JOÃO EDUARDO GENTIL LÉ

Improvements and W Band expansion of the antenna characterization system of the “EPUSP mmW Center”

São Paulo
2023

JOÃO EDUARDO GENTIL LÉ

Improvements and W Band expansion of the antenna characterization system of the “EPUSP mmW Center”

Corrected Version

Dissertation presented to the Polytechnic School of the University of São Paulo for the title of Master of Science.

Area of Concentration: Microelectronics

Advisor: Prof. Dr. Gustavo Pamplona Rehder
Co-advisor: Prof. Dra. Ariana Maria da Conceição Lacorte Caniato Serrano

São Paulo
2023

Este exemplar foi revisado e corrigido em relação à versão original, sob responsabilidade única do autor e com a anuência de seu orientador.

São Paulo, de de

Assinatura do autor:

Assinatura do orientador:

Catalogação-na-publicação

Gentil Lé, João Eduardo
Improvements and W Band expansion of the antenna characterization system of the “EPUSP mmW Center” / J. E. Gentil Lé -- versão corr. -- São Paulo, 2023.
100 p.

Dissertação (Mestrado) - Escola Politécnica da Universidade de São Paulo. Departamento de Engenharia de Sistemas Eletrônicos.

1.ANTENAS 2.INSTRUMENTAÇÃO ELÉTRICA 3.ONDAS MILIMÉTRICAS 4.TELECOMUNICAÇÕES I.Universidade de São Paulo. Escola Politécnica. Departamento de Engenharia de Sistemas Eletrônicos II.t.

ACKNOWLEDGMENTS

This work is dedicated to my parents, Regina Marcia Violin Gentil and Júlio César Lé, for their sponsorship and unconditional support.

I thank my wife, Gabriela Boccardo Lé, for being part of my daily life; a sometimes confused presence, but loyal and intense. I wish you had come with an operating manual as detailed as this text.

I thank my advisors, Gustavo and Ariana, for having proposed to me the challenge of carrying out this work, for their patience and for pioneering the path I am following.

I thank my colleagues and employees of the Microelectronics Laboratory (LME-USP) for their interaction and help during during the period of my undergraduate and master's degree: Gustavo Palomino, Igor Abe, Alexandre, Pedrinho, Raimundo, Jair, Maurício.

Finally, I thank prof. Rafael Penchel and his student Elígia Simionato, both from São Paulo State University, for the design and simulation data of the Sections 4.3.1 and 4.3.2 antennas, and Dongwei Wang from Technical University Darmstadt, for the design of Section 4.3.3 antenna.

This work was carried out with the support of CNPq, The National Council for Scientific and Technological Development - Brazil.

RESUMO

GENTIL LÉ, J. E. **Melhorias e ampliação da Banda W do sistema de caracterização de antenas do “EPUSP Centro mmW”**. 2023. 100p. Dissertação (Mestrado) - Escola Politécnica, Universidade de São Paulo, São Paulo, 2023.

Devido à disponibilidade de espectro, o estabelecimento de canais de comunicação nas Ondas Milimétricas tem se mostrado uma alternativa concreta para atender à crescente demanda por taxa de transmissão de dados. Antenas desempenham um papel crucial em sistemas sem fio; testes precisos desses dispositivos são necessários para se obter um bom desempenho geral do sistema. No entanto, a caracterização de antenas em ondas milimétricas apresenta desafios em termos de tecnologia e custo. O objetivo deste projeto é aprimorar e expandir um sistema de caracterização de antenas que está sendo desenvolvido no Laboratório de Microeletrônica, que faz parte da Escola Politécnica da Universidade de São Paulo (EPUSP). Rotinas de teste foram desenvolvidas para calcular os erros e garantir o correto funcionamento do sistema. Tais testes mostraram valores de erro abaixo de 0.2 dB para medições de diagrama de radiação. Também se concluiu que o sistema desenvolvido possui um desalinhamento mecânico da ordem de 1 mm e erros de posicionamento de motores de passo inferiores a 0.2°. Antenas nas bandas V e W foram medidas para validar seu desempenho. Os resultados mostram que o sistema desenvolvido é capaz de capturar nuances sutis em uma ampla faixa de potências, especialmente na banda V, onde a suavidade nas medições indica ausência de sinal refletido. Vários formatos de apresentação de dados são empregados para tornar a apresentação dos resultados mais compreensíveis, destacando ainda mais a robustez e confiabilidade do sistema de caracterização de antenas desenvolvido.

Palavras-chave: Antenas, Instrumentação Elétrica, Ondas Milimétricas, Telecomunicações.

ABSTRACT

GENTIL LÉ, J. E. **Improvements and W Band expansion of the antenna characterization system of the "EPUSP mmW Center"**. 2023. 100p. Dissertation (Masters) - Polytechnic School, University of São Paulo, São Paulo, 2023.

Due to the availability of bandwidth, the establishment of communication channels in Millimeter Waves has emerged as a viable alternative to meet the growing demand for data exchange rates. Antennas play a crucial role in wireless systems, and precise testing of these devices is necessary to achieve overall system performance. However, characterizing antennas at Millimeter Wave frequencies presents challenges in terms of technology and cost. The objective of this project is to improve and expand an antenna characterization system that is being developed at the Microelectronics Laboratory, part of the Polytechnic School of the University of São Paulo (EPUSP). Test routines were developed to calculate errors and ensure the correct functioning of the system. These tests showed error values below 0.2 dB for radiation pattern measurements. The tests also concluded that the developed system has a mechanical misalignment on the order of 1 mm and stepper motor positioning errors lower than 0.2°. Antennas in the V and W bands were measured to validate its performance. The results demonstrate that the developed antenna characterization system is capable of capturing subtle nuances of fabricated antennas across a wide range of power levels, particularly in the V band, where smoothness in measurements indicates the absence of signal reflections. Various data presentation formats are employed to make the results more comprehensible, further highlighting the robustness and reliability of the developed antenna characterization system.

Keywords: Antennas, Electrical Instrumentation, Millimeter Waves, Telecommunications.

SUMMARY

1 Introduction

1.1 Interest of the Millimeter Waves

Engineers are technical people. Once they get a problem, they will search for one solution. What caused the problem is rarely important if it does not help to overcome it. The society agreed at some point between the cognitive revolution [1] and the Marconi experiment [2] that telecommunication is important to the human being. At that exact point, engineering acquired new problems: how to telecommunicate more reliably, more efficiently, less expensively and in a more comfortable way. While all these features are positive, they are not fully compatible. The application will weight each one over the others and every telecom application will dictate their own needs for the system designer:

- In Wireless Local Area Networks (WLAN) systems, like WiFi ones, the router designer must ponderate between efficiency and cost when choosing components available on the market;
- In satellite television broadcasting systems, reliability is not so important as cost and usefulness. That is the reason for the signal loss on rainy days.

It follows, then, that it is not possible to say that one form of data communication is always better than others. Any impression about technology research direction will reduce the number of applications that it could benefit. In other words, the technological frontier advances in a discrete and uncoordinated way. As will be clear in the following lines, the present work falls within the scope of telecommunications, in applications that emphasize the efficiency of data exchange in wireless systems.

One clear telecommunication system characteristic concerns the transmission media it uses: guided or unguided medium. Metallic (twisted pair or coaxial), waveguides and optical fiber are used in the first category; antennas are used in the second one. Unguided systems use the atmosphere to communicate. To ensure that one system does not disturb the other, the spectrum is divided into bands, through national and international legislation. Communication channels are established on one or a set of bands. In general, establishing the channel in higher frequency bands reduces the size of the device (so then circuits and systems), increases the

project/fabrication/measurement complexity, increases the propagation loss if there are obstructions along the path and increases the channel capacity. This last point is of paramount importance: channel capacity is an upper limit bound at which Shannon Information [3] can be transferred between nodes of a communication system, and it's given in bits per unit of time. Although it depends on the statistical properties of the channel, which is again application-dependent, an intuitive way to understand how to maximize the capacity is to study a typical case of a continuous-time analog channel subjected to Gaussian noise. According to the Shannon-Hartley theorem [4], the channel capacity [Bits/s] in this situation is given by Eq. 1, where *B* [Hertz] is the channel bandwidth, *S* [Watts] and *N* [Watts] are the average received signal power and the average received noise power over the bandwidth, respectively.

$$C = B \cdot log_2(1 + \frac{S}{N}) \quad \text{(Eq. 1)}$$

A channel with great capacity is an efficient channel. For example, in systems that does not require high rates, it is possible to use code redundancy to trade capacity for reliability. Two reasons limit the use of *S* to increase *C*: (i) it is a logarithmic relation and (ii) the maximum amount of power that a transmitter can emit is not arbitrary but regulated by international agencies. On the other hand, *B* and *C* are linearly related when the signal noise ratio (*S/N*) is greater than the unit; doubling the bandwidth doubles the upper limit of information exchange. It is possible to conclude that using more bandwidth is the main manner to increase the capacity of a channel.

However, it is not always possible to increase the bandwidth, as it is generally a fraction of the channel center frequency. As a real world example, let's see the case of two different band standards for WLAN developed by the same IEEE 802.11 Working Group [5]: the *802.11ac* protocol was released in December 2013, is centered at 5 GHz and has a maximum channel bandwidth of 0.16 GHz; *802.11ad* is another protocol released in December 2012, centered around 60 GHz, where channels are 2.16 GHz wide. Another way to look at this is through the spectrum allocations chart available on the National Telecommunications and Information Administration (NTIA) website [6], which is the agency that manages the Unites States of America federal use of the spectrum. A slice of this graph concerning the 2.4 GHz vicinity is shown in figure 1: channels are at most a few tens of megahertz wide. This is the reason why, a few paragraphs earlier, it was mentioned that

increasing the channel's center frequency leads to greater channel capacity. Mobile operators are dealing with this limitation using Carrier Aggregation schemes, which allows the combination of various slices of this spectrum chart to create a unique channel [7]. However, spectrum is a scarce resource, and future congestion at low frequencies is inevitable. To give us an idea about this crowding, NTIA claims [8] that 93% of government spectrum use is below 3 GHz.

Figure 1: USA spectrum allocation chart.

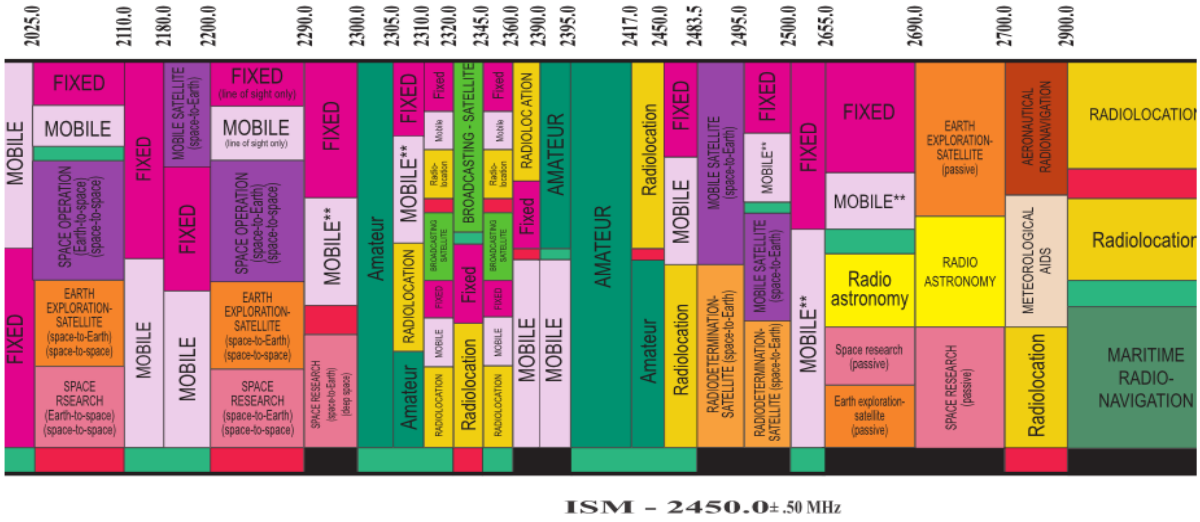

Source: [6].

Summarizing, a great alternative for wireless telecommunications applications that require high data rates and are not completely blocked by obstacles (channel with Line-Of-Sight [LOS]) is to establish the communication channel at higher frequencies, particularly within the Millimeter Wave bands (30-300 GHz), due to the abundance of spectrum not yet fully explored. In a research targeting cellular networks working at 28 and 73 GHz in the New York City environment, in reference [9], authors concluded that systems working at Millimeter Waves can offer, without an increase in cell density, at least one order of magnitude more capacity than existing microwave cellular links such as 4G LTE. In [10], the same authors give examples of Millimeter Wave applications, working around and above 100 GHz, that demand high data exchange rates and low latency, such as autonomous vehicles communication, robotic control and wireless fiber for backhaul.

However, the hardware used in transceivers becomes increasingly complex as the operating frequency increases. Passive devices must have physical lengths less than 1/20 of the guided wavelength to be considered concentrated. Consider a capacitor placed between 50 Ohm transmission lines for DC decoupling. Assume

these lines are microstrip, with an effective dielectric constant equal to 6. If the circuit were designed to work around 5 GHz, the capacitor should not be longer than 1.23 mm, since the guided wavelength is equal to 24.49 mm. If the capacitor was designed for 60 GHz, its dimension should not exceed 102 µm. This means that circuits must be fabricated in a monolithic approach, using microelectronics techniques such as lithography and thin film deposition.

Nonetheless, it is for active devices that the relation between technological nodes and frequency becomes more pronounced. Active devices are based on transistors; an important parameter for them is the frequency at which the small-signal current gain drops to unity, which is called cutoff frequency (f_t). It's an operational upper limit of the technology. For a circuit to work close to the f_t, it has to be very well designed. For silicon, it's possible to increase the cutoff frequency reducing the gate length [11], ie. using the most recent nodes. Another alternative is to work with III-V materials [12], like GaAs or InP, which have greater electron mobility than silicon. However, both alternatives could be very expensive and not fully suitable for the customer market.

If the design of a simple prototype is a complex task, it is not hard to imagine that it is even more challenging to develop devices that are used for testing and characterization such as: spectrum analyzers, signal analyzers, signal generators, power sensors, vector network analyzers (VNAs). These instruments are mainly developed by few historical companies, such as Keysight (formerly Hewlett-Packard), Anritsu and Rohde & Schwarz, and are band-specific with the costs increasing with frequency.

Instruments are definitely necessary, despite being expensive. As will be shown in the next sections, Millimeter Wave research labs around the world have begun to build an infrastructure that will enable the characterization of the next generation of telecommunications research and products. And when the budget is not enough, instrumentation becomes the object of research and development. This is the case of the present study, whose objective is to discuss the problem of characterizing antennas in Millimeter Waves. As a final result, a functional setup operating at the V (50-75 GHz) and W band (75-110 GHz) is presented.

1.2 State of the art of Millimeter Wave antenna measurement setups

1.2.1 Overview

The constituent devices of a measurement setup can be divided into the following categories: instruments, test fixtures and device under test (DUT). Cables, waveguides, adaptors, connectors and probes are examples of test fixtures devices, and their purpose is to provide an interface between instrumentation and DUT, without disturbing the measurements. That said, let's imagine what are the penalties when using a coaxial connector to interface between some Millimeter Wave planar antenna and a VNA. This connector, which will not exist in a final version of the front-end device, will likely be soldered to the access port; soldering will change the characteristic impedance of the line, as well as introducing parasites, such as parallel-to-ground capacitances and series inductances. Furthermore, the dimensions of the connector will be much larger than those of the Millimeter Wave antenna, since its size is of the order of the wavelength. During the measurements, this huge metallic mass will definitely change the radiation behavior.

In this way, due to the small antenna dimensions and the high working frequencies, connectors should not be used to test these Millimeter Wave antennas. The connection to the antenna must be done with fragile coplanar waveguide (CPW) micro-probes. This creates an additional difficulty in positioning when compared with measurements of connectorized antennas in classic anechoic chambers: two micro-positioners must be used, one for the antenna under test (AUT) and one for the probe. Such a set cannot be moved after the contact between probe and AUT is established.

Another difference in relation to measurements at lower frequencies, but which is already a trend in device measurements in Millimeter Waves, is the use of frequency converter instruments in the signal path. The movement of such devices must be taken into account when designing a measurement system.

Finally, perhaps the reader will be surprised by the difference between the Millimeter Wave antenna measurement systems presented below and the conventional anechoic chambers. There is a big difference between the amount of absorbing materials. This is basically due to two reasons. The first is that the external electromagnetic interference is very small compared to measurement systems below

6 GHz. The second is that the wave that hits a surface and is reflected has some difficulty reaching the AUT, since it has a very small effective area. Thus, absorbers should undoubtedly be placed on metal surfaces close to the antennas, but their use around the system is arbitrary.

This section presents some Millimeter Wave antenna measurement facilities worldwide. They are presented in an increased level of in-house development. All of them are capable of probe based measurements, ie. non-connectorized antennas. The information was taken from scientific articles or laboratory websites.

1.2.2 University of Sheffield - England

NSI-MI is a North-American Company [13] with a complex and complete portfolio for high-frequency measurements. Its solutions include: antennas, mechanical positioners and controllers, reflectors, benchtop instruments (signals sources and receivers), control and processing softwares, as well as already pre-configured systems as compact range, radome, near and far-field, target simulation systems. In May 2021, it was acquired by AMETEK for $230 million [14].

University of Sheffield's Communications Research Group uses the spherical positioner SNF-FIX-1.0 from this company [15]; together with a Keysight PNA and Virginia Diodes extensors, they can measure antennas from 10 to 110 GHz (Fig. 2). They claim to be the first in the United Kingdom to have a setup working on these frequencies. Three motors move the Reference Antenna (RA) over a complete sphere (up to 1m of diameter), with 0.01° of resolution at a maximum 5°/sec velocity. The spherical movement is limited only by the support structure of the AUT. The solution comes with a computer preloaded with the NSI2000 Antenna Measurement Software, which provides RA movement, instrument acquisition, data processing and visualization.

In Fig. 3, it is possible to see the apparatus used to contact the probe with the AUT. Only one micropositioner could be seen, which assumes that the AUT is manually adjusted to its ideal position. Attention should also be paid to the absence of absorbers on the reflective surfaces close to the AUT. Although moving the RA allows measurement of an almost complete sphere, the use of an AUT base that is not transparent to Millimeter Waves limits this measurement to the upper hemisphere.

Figure 2: Millimeter Wave antenna measurement facility at the University of Sheffield, England.

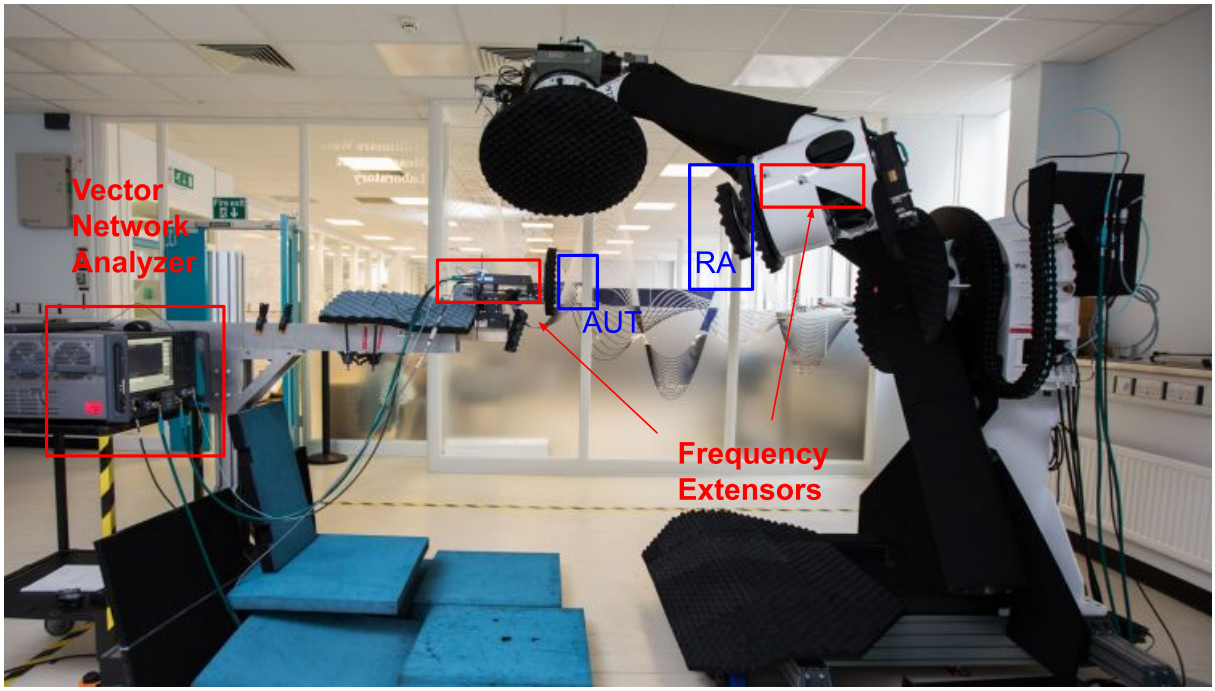

Source: extract from the University of Sheffield website [15] video; annotations were made by the author.

Figure 3: AUT placement and contact of the Millimeter Wave antenna measurement facility at the University of Sheffield, England.

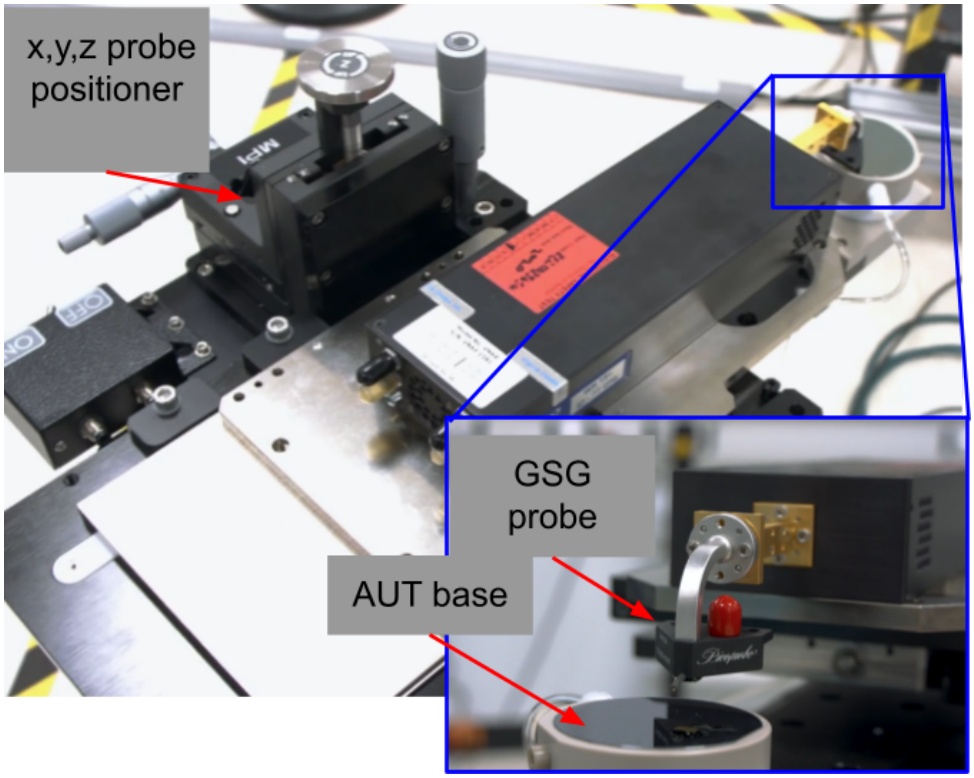

Source: extract from the University of Sheffield website [15] video; annotations were made by the author.

1.2.3 Ulm University - Germany

At the Institute of Microwave Engineering of the Ulm University, there is a robot-supported test range for integrated antennas measurements between 100 GHz and 330 GHz, supporting near and far field characterization. The commercial-industrial robot arm moves the reference antenna at an almost complete half hemisphere trajectory, as could be seen at the insert of Fig. 4, with a maximum resolution of 0.5° and 4°, for elevation and azimuth, respectively [16]. It probably uses a mixer to create the emitted signal ("Rx Module") and a frequency extender to receive the signal ("TxRx Module"). They claim to have created the software for control and data processing.

Figure 4: Millimeter Wave antenna measurement facility at the Ulm University, Germany.

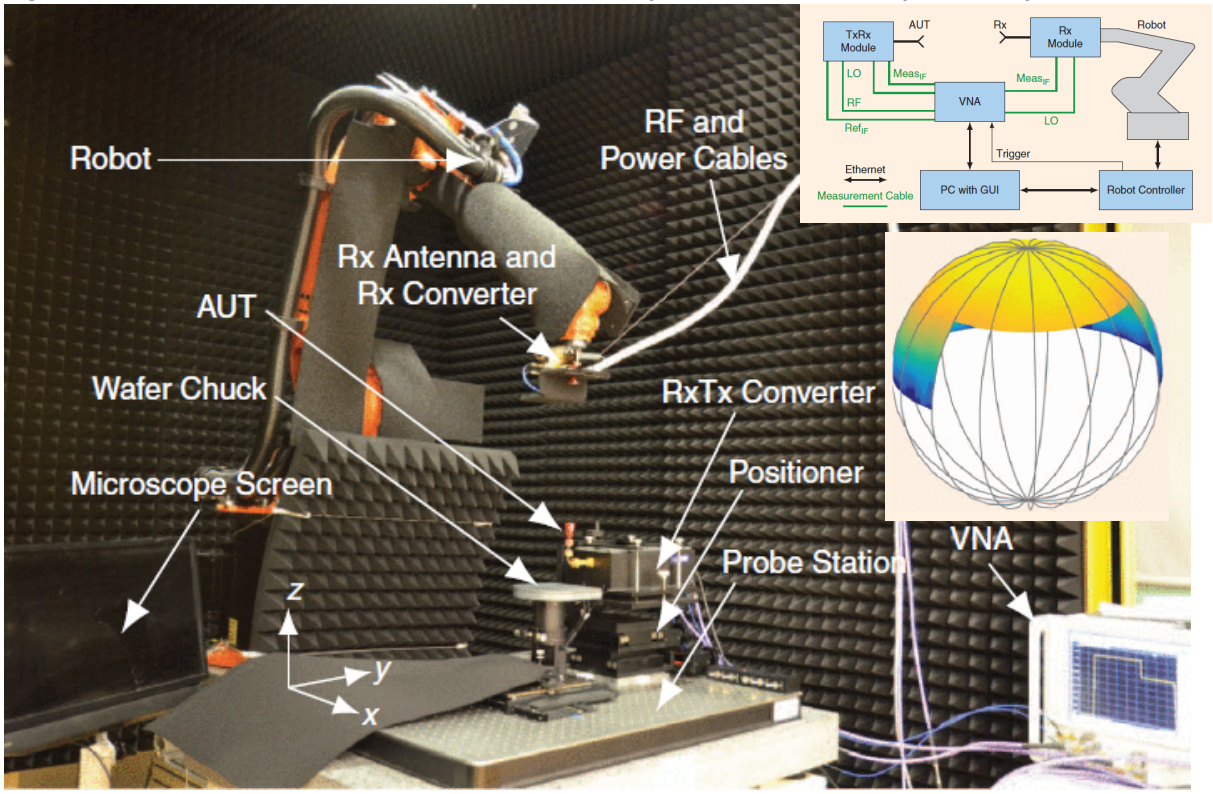

Source: extract from Ref. 16; inserts were added by the author. The figure also shows a block diagram, in addition to a spherical graph showing the measurement limits of the setup.

An improvement over the previously presented configuration is that the GSG probes are customized to keep the AUT away from the metallic waveguides, in addition to the use of absorbers on the closest surfaces. Due to the small uncertainty of positioning the AUT presented in [16], probably there must be a manual micro-positioner for both the AUT and for the probe.

Figure 5: AUT placement and contact of the Millimeter Wave antenna measurement facility of the Ulm University, Germany.

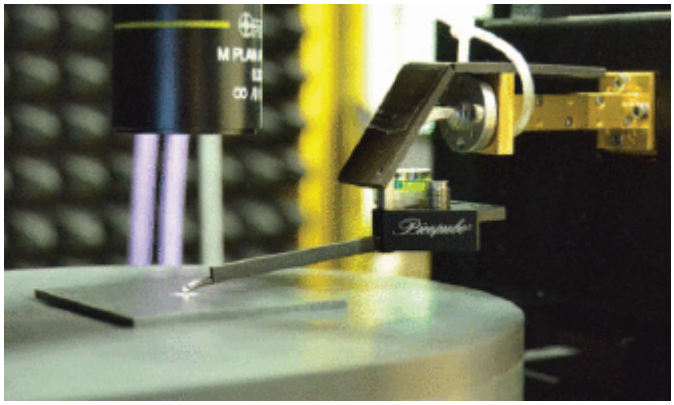

Source: extract from Ref. 16.

1.2.4 Eindhoven University of Technology - Netherlands

The Center for Wireless Technology (CWTe) created an in-house, near-field scanner system operating from 24 to 110 GHz [17]. As the above setups, the AUT stays stationary while the RA moves in a spherical manner around it. Antennas are in a real anechoic environment, very well designed against electromagnetic perturbations. From the article's figures where it was presented [17,18], it is not possible to see frequency extenders or mixers; this does not allow us to conclude how friendly this setup is to changing the operating band.

Figure 6: Millimeter Wave antenna measurement facility of the Eindhoven University of Technology, Netherlands.

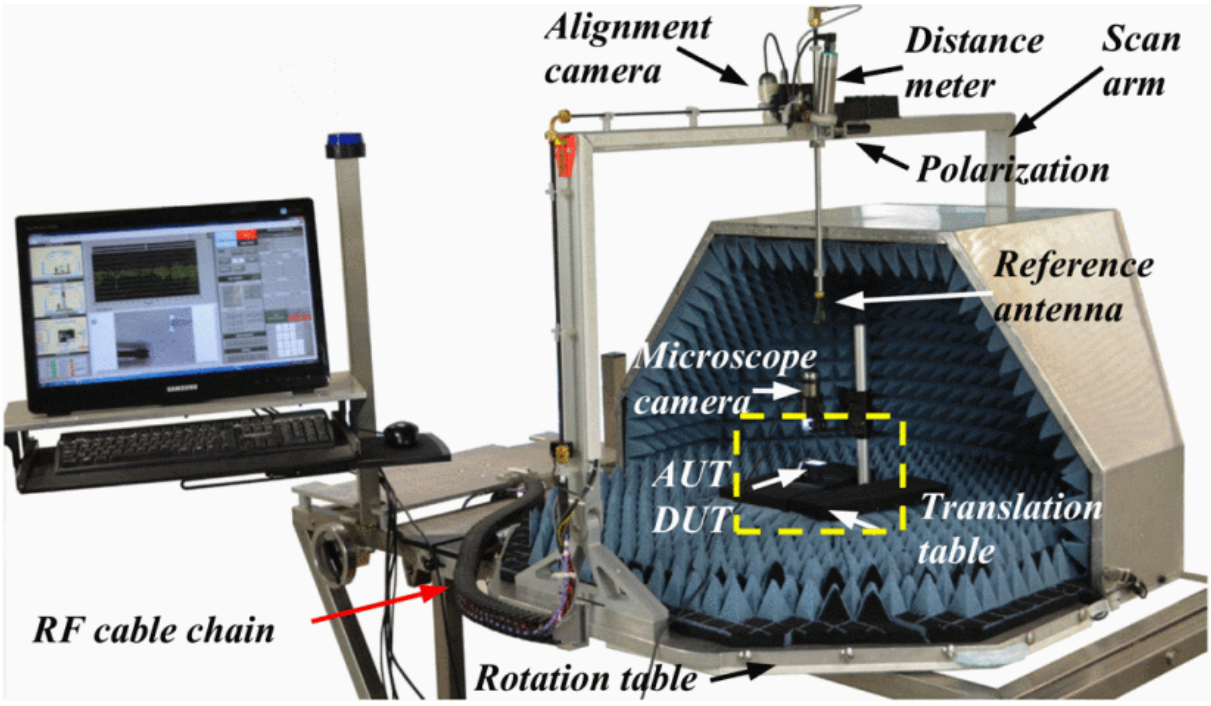

Source: extract from Ref. 17.

An interesting feature in this setup is the format of the probe: it has a long body and the coaxial connector comes from the bottom (Fig. 7), which reduces this test fixture influence during measurements. It is not possible to see, however, how the AUT is positioned in the center of the measurement sphere.

Figure 7: AUT placement and contact of the Millimeter Wave antenna measurement facility of the Eindhoven University of Technology, Netherlands.

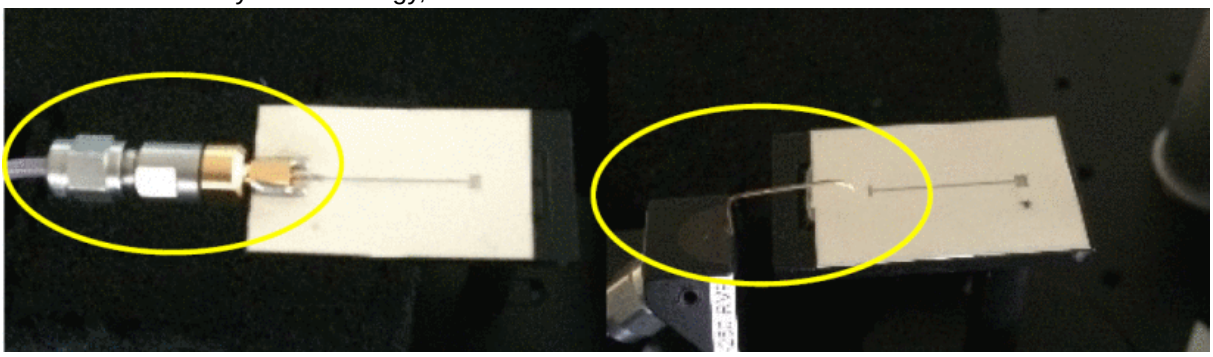

Source: extract from [18].

1.3 Objectives and organization of the text

The “mmW Center” [19] is a research center that combines state-of-the-art equipment and qualified personnel with the objective to spread knowledge and help Brazilian companies and research groups in the development and testing of Millimeter Wave devices, circuits and systems. It is part of the Microelectronics Laboratory, within the Polytechnic School of the University of São Paulo (USP). In 2016, after acquiring a Keysight VNA (PNA N5247B) and frequency extenders from OML, it became the first laboratory of Latin America with the ability to measure two port devices up to 110 GHz and four port devices up to 67 GHz.

Efforts to create a Millimeter Wave antenna characterization system began around 2018. When this author joined the team (2019), the laboratory already had a mechanical apparatus that moves the reference antenna in elevation and azimuth, and the necessary instrumentation (VNA, cables and multiplier) to measure V band antennas, as can be seen in Fig. 8. The control software was capable of controlling the movement of the motors through an Application Programming Interface (API), with a G-code scheme, provided by the microcontroller connected to the motor drivers, previously implemented by another student. But as the communication part with the VNA was missing, the system was not functional.

Figure 8: Millimeter wave antenna measurement facility in early stage of development at the University of São Paulo, Brazil.

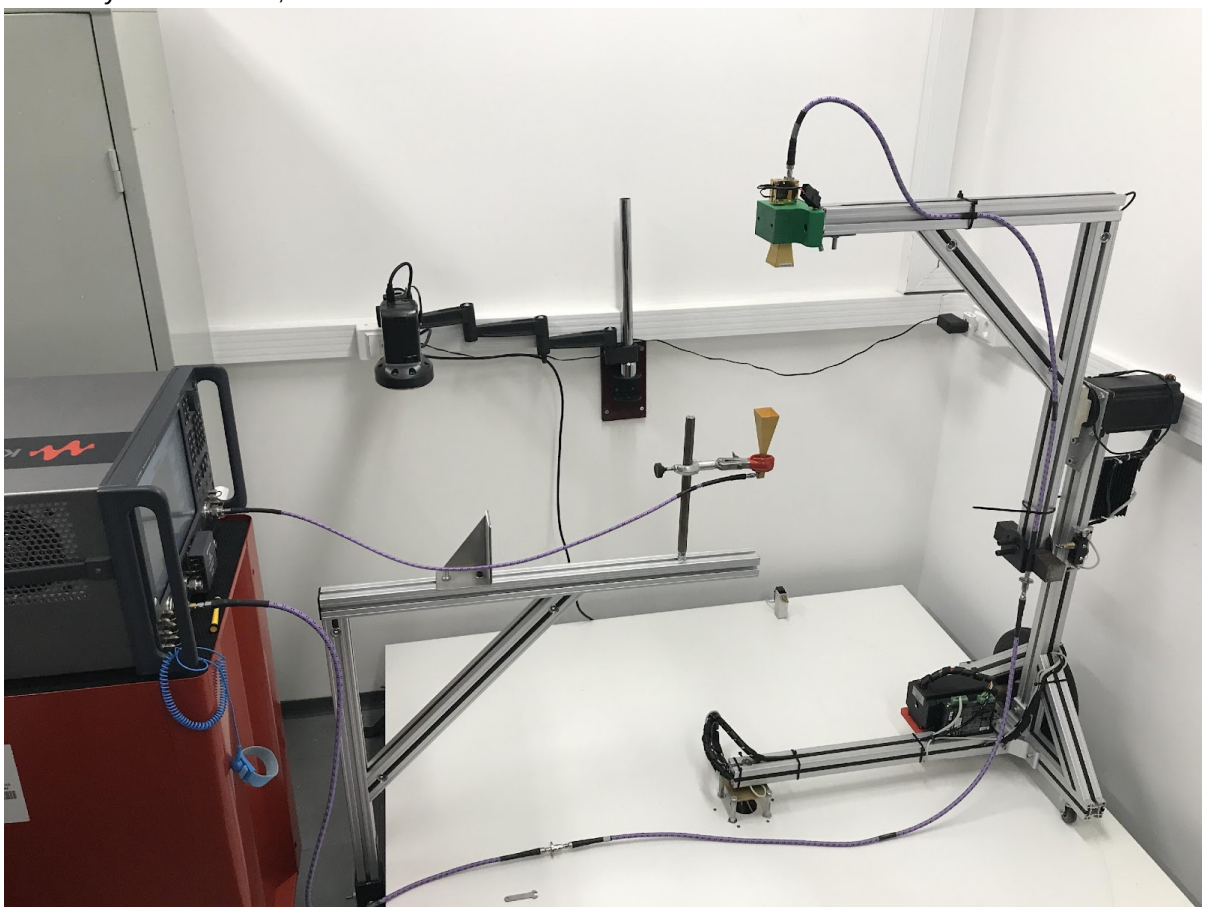

Source: author.

But even if the acquisition part was ready, what is the value of a measurement without its accuracy information? Could one say that a measurement is good if the data looks like the simulation? If so, there is no reason to measure a device. It's easier to just rely on modeling and simulation.

Another shortcoming of the present setup implementation is the lack of repeatability caused by manually positioning the AUT. There will be different results for each placement of the same AUT. With that in mind, the summarized objectives of this work are:

1. Improve the mechanical part of the system to create repeatable results, reducing inaccuracies that can be reduced and accounting for those that cannot be avoided;
2. Expand the system capabilities in terms of parameters extraction and frequencies;

3. Develop algorithms for extracting results and implement a software capable of acquiring, visualizing and retrieving data.

To be able to understand the system's sources of errors, we need to take one step back and study the theory behind antennas tests, and establish some assumptions. This is done in Chapter 2, which is divided into theory and practice. Then, in Chapter 3, we present the final configuration of the antenna characterization system in terms of its electromagnetic and electromechanical parts. This division helps seeking for points that disagree with the cited assumptions. In this same chapter the software capabilities and user interface are introduced. In the fourth and final section, we study the statistical accuracy of the system and show some real-world antenna measurements results.

2 Antennas, parameters and measurements methods

2.1 Overview

It is possible to define antennas as electromagnetic energy transducers that are inserted between free space and guided media in electrical circuits. As mentioned, in telecommunications networks, electromagnetic waves carry information; when free space is used as the channel, two (or more) antennas are used to couple the source to the receiver(s); the purpose of the antennas, in this case, is to provide the greatest possible coupling between the systems. This coupling, in turn, depends on several factors, such as: relative position between transmitting and receiving antennas, antenna radiation characteristics (the way the energy is spatially distributed), the amount of power injected into the transmitting antenna and losses - in free space, in the impedance mismatch between the antenna and in the materials of the guided circuit.

The parameters presented in the following topics are well known and give the designer of Millimeter Wave systems an idea of the radiation characteristics of a fabricated antenna. Based on this empirical information, the coupling of two or more circuits can be predicted; thus, through these figures of merit, the designer should be able to tell if a given antenna meets the requirements of the communication system.

Before introducing the main parameters sought in antenna tests, some definitions need to be established. Two antennas are used in the measurements: the antenna-under-test (AUT), and the reference antenna (RA). The RA makes a spherical path around the AUT, with a constant radius, always pointing to the antenna under test, which is at the center of this sphere. As a consequence of the theorem of reciprocity of electromagnetism (section 3.8 of [20]), the properties of antennas are the same whether the antenna is receiving or transmitting, ie. they are reciprocal devices. It means that in a reciprocal two port network formed by two antennas, air, a source and a load termination, no matter which antenna is excited or measured, as the transmission of the signal does not depend on the direction of propagation. This will allow us to theorize scenarios in which the AUT is the power transmitter, even though it is configured in our setup on the power receiver side. The setup’s goal is to create, at the AUT aperture, a planar (far-field condition [21]), linear polarized wave, coming from an arbitrary controlled direction. The constant radius movement guarantees a fixed received power density at this aperture independent of the wave

direction. Those assumptions are the basis for virtually all measurement results, and allows one to understand the relationship between received (transmit) and transmitted (received) power. It is natural to use a spherical coordinate system to define the radiation properties of the AUT. This way, two angles are used to distinguish the direction of radiation: the **azimuth** is represented by the Greek letter “phi" (φ); the **elevation**, by the Greek letter “theta” (θ). The spherical coordinate system is shown in Fig. 9.

Figure 9: Spherical coordinate system.

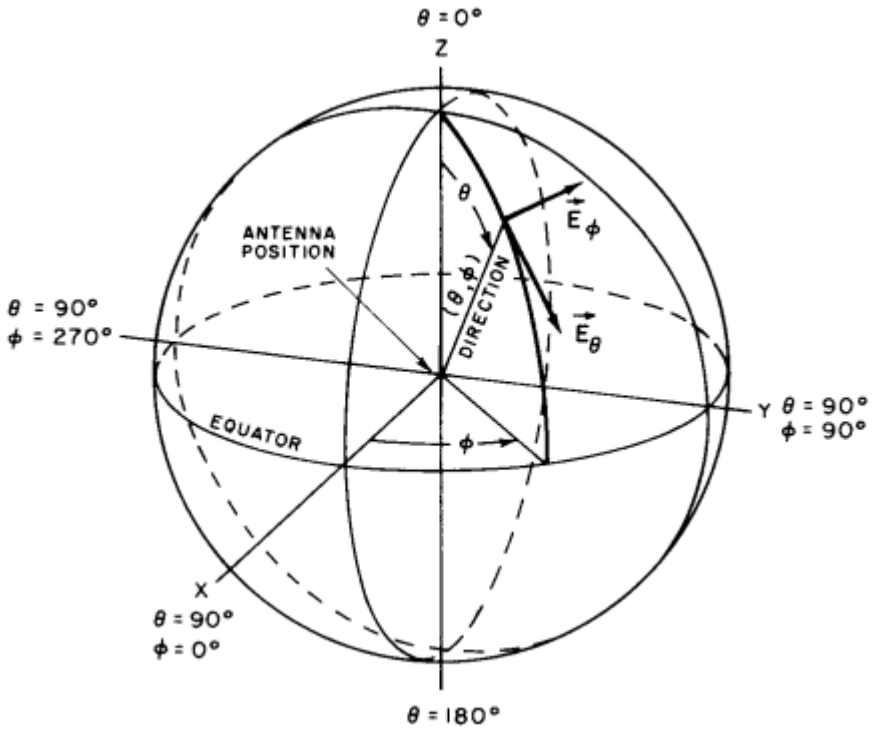

Source: [22]

However, only the spherical coordinate position of this RA or, in this case, of the incoming wave, is not enough to unequivocally distinguish the radiation direction of the AUT. For example, fix the RA at any point in the system of Fig. 9. For each AUT rotation displacement, even though its center is held at the zero-radius position, there would be a different coupled value[1]. In this way, the radiation direction must take into account the relative coordinates, that is, the angular position of the RA subtracting the rotation of the AUT. This is the meaning of the ‘r’ subscript of the position (φ_r,θ_r), present in section 2.2, and the reason why the measurements are

[1] The only case that it doesn’t change is for an isotropic AUT.

presented differently, without the index, in Section 2.3. In Subsection 3.3.3 it will be discussed when this difference is important and how to overcome it.

2.2 Antenna Measurement Theory

2.2.1 Radiation Pattern

There are a lot of definitions for this figure of merit in the literature. In this section, some of them will be discussed and it will be concluded that only one of them is feasible to be measured, is invariable to the measurement conditions and carries all the necessary and sufficient information about the spatial radiation characteristics of the antennas.

In page 74 of [23], this parameter is defined as *"The spatial distribution of a quantity that characterizes the electromagnetic field generated by an antenna"*. In NOTE 4 and 5 that follows: *"When the square of the amplitude or relative amplitude is plotted, it is called a power pattern. (…) When the quantity is not specified, an amplitude or power pattern is implied"*. For measurements purposes, this definition is ambiguous, as it may mean that the radiation pattern relates the coupled power ("power") and the relative position between this AUT and some RA; this is how most researchers deal with this measure. However, this definition does not exclusively define the behavior of the AUT, as this "power pattern" is a function of (i) the relative elevation and azimuth coordinates between RA and AUT, (ii) the RA radiation characteristics, (iii) the distance between the antennas and (iv) the power inserted into the system, which would not allow an easy extrapolation of the results for other scenarios.

A more practical definition should take into account the power density; this is what Balanis does, in [20, page 36]: "*The power pattern of the antenna (...) is just a measure, as a function of direction, of the average power density radiated by the antenna*". As an example of this distinction, in Fig. 10 is shown a scenario where the AUT is radiating and the receiving RA is positioned at three different radius positions. The power coupled in the scenario using the reference antenna RA3 is smaller than that using the RA1, as the former extends over a smaller area of the spherical shell than the latter. However, the power density ρ_3 is equal to ρ_1. Thus, using power density instead of power, the radiation pattern measurement is indifferent to the RA characteristics and distance to the AUT. However, imagine how hard it would be to

measure power density; one must know the total power value that is received by the receiving antenna and divide this value by its effective area. For this, it is necessary to know all the signal losses between this antenna and the power receiver. Another point is that this measure is still a function of the system feed power.

Figure 10: Relationship between distance between antennas, effective area of the reference antenna, power received by the reference antenna and power density.

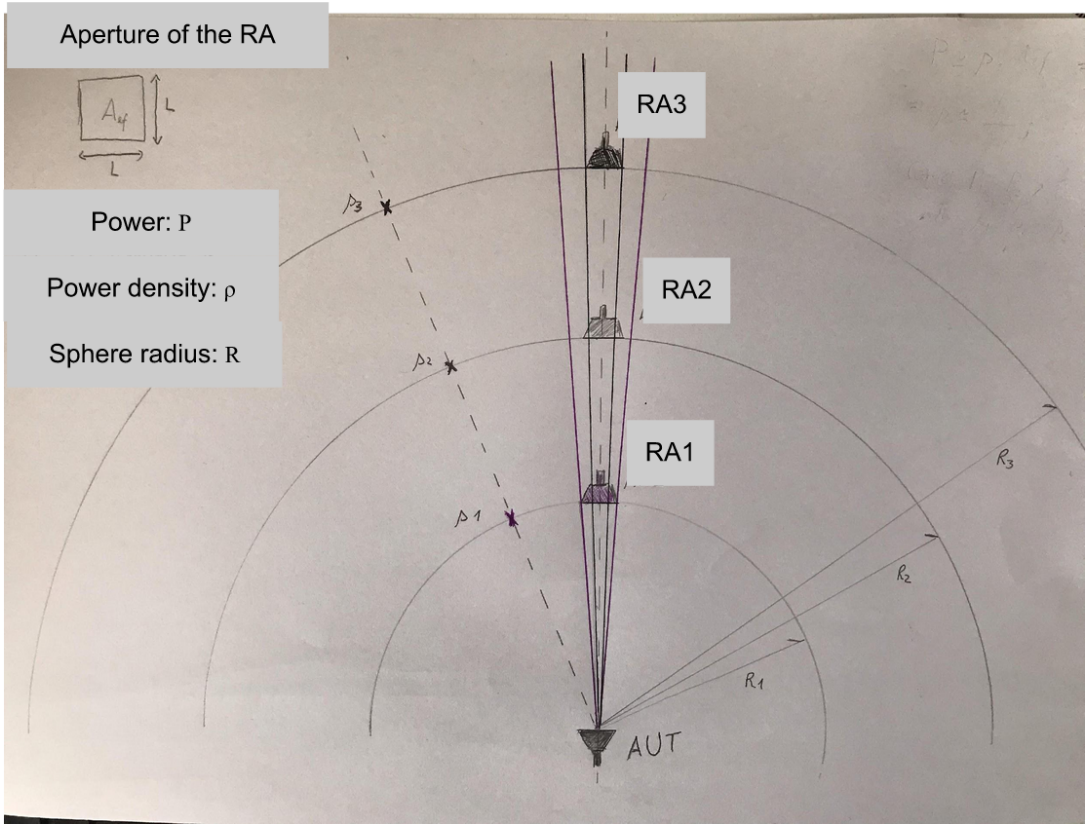

Source: author. In this scenario, $\rho_1=\rho_2=\rho_3$ and P1>P2>P3. This way, working with power densities, instead of powers, makes the distance between the antennas not decisive during the tests.

For the measurement of the radiation pattern to become viable, normalized power density is used instead. Actually, Balanis suggests, but does not define, that this normalized measurement is preferred [20, page 36]: "*In practice, absolute power patterns are usually not desired".* As will be shown in section 2.3.1, this is obtained by normalizing the received power by the maximum received power, and this diagram is independent of the characteristic of the RA, the distance between RA and AUT, the source's power level and all the circuits that surround it.

Summarizing, the radiation pattern is a graphical description of the spatial distribution of the energy, when the AUT is used as a transmitter, or the spatial affinity of incoming energy, when it is used as a receiver. In this work, it is given in normalized power density (ρ_{Norm}) and is a function of the relative angular position

(elevation and azimuth) of the receiver, if the AUT is the transmitter, or the transmitter, if the AUT is the receiver. Based on this definition, one can define the normalized radiated power ($P_{radNorm}$) of the antenna as:

$$P_{radNorm} = \oiint \rho_{Norm}(\varphi_r, \theta_r) \cdot dA = \oiint \frac{\rho(\varphi_r, \theta_r)}{C} \cdot dA = \frac{P_{rad}}{C} \qquad \text{(Eq. 2)}$$

For a configuration where the AUT is the source, P_{rad} is the total power radiated (a function of the power input at the antenna terminals), and C is the normalization constant, which depends on the power generated at the source, the distance between antennas, RA characteristics and circuit characteristics between RA and signal receiver. $P_{radNorm}$ only depends on the radiation/reception characteristics of the antenna. The integration surface is the spherical shell formed by the trajectory of the reference antenna.

Figure 11: 3D and 2D Radiation Patterns examples.

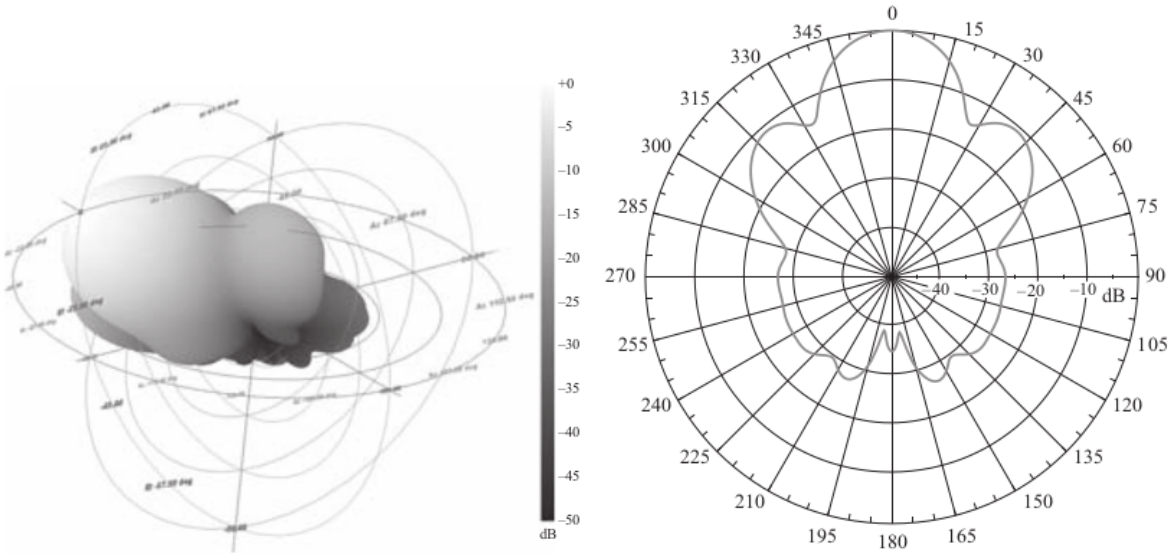

Source: [21]. In the image on the left, it is shown the three-dimensional (3D) representation of the radiation pattern; each point on the spherical shell is represented by an amplitude value (normalized power density). In the image on the right, one of the planes of the 3D plot is extracted, generating a 2D radiation pattern, which is most commonly used to present this type of data.

In Fig. 11, there is a view of how the radiation pattern is normally presented. The image on the right (2D representation) is a slice of the image on the left (3D representation). In most cases, only two perpendicular slices are used to represent the radiation pattern of an antenna. It should be noted that there are an infinite number of 2D radiation patterns. The datasheet or scientific article must make it clear to which spatial section the diagram refers. It is usual to align the measurement coordinate system to the AUT so that the place of greatest radiation is the position

(φ=0, θ=0). In this way, the image on the right of Fig. 11 would represent a normalized power density (note that the maximum value is at 0 dB) as a function of the elevation angle, for a fixed azimuth angle. This type of graph can be displayed in cartesian or in polar coordinates. Directivity is a performance factor derived from the radiation pattern; it will be presented in the following section.

2.2.2 Directivity, Efficiency and Gain

It is possible to see, in Fig. 11, that the antenna concentrates energy in one direction to the detriment of the other directions. It is common to say that an antenna is more directional when this ratio is more pronounced, and this antenna can radiate or receive a large amount of power density in a given direction, compared to other directions. An antenna that radiates in all directions with the same intensity is called isotropic, and is the complete opposite of a directional antenna. This quality of focusing the beam of electromagnetic energy is the property of directivity. For its definition, the relationship between the concept of radiation power intensity (*U* [Watts/unit of solid angle]) and the aforementioned power density (*ρ* [Watts/square meters]) is needed. The following formula is used in the transformation (expression 2-12 in [20]):

$$U\left(\varphi_r, \theta_r\right) = r^2 \cdot \rho\left(\varphi_r, \theta_r\right) \quad \text{(Eq. 3)}$$

Where "*r*" is the distance, in meters, between the AUT and the spherical shell considered in the calculations. Manipulating this equality to insert the normalized value gives:

$$U\left(\varphi_r, \theta_r\right) = \frac{r^2 \cdot \rho\left(\varphi_r, \theta_r\right) \cdot C}{C} = r^2 \cdot \rho_{Norm}\left(\varphi_r, \theta_r\right) \cdot C \quad \text{(Eq. 4)}$$

Finally, [23, page 74] defines directivity as: *"the ratio of the radiation intensity in a given direction from the antenna to the radiation intensity averaged over all directions"*. And, in the following NOTE 1: *"The average radiation intensity is equal to the total power radiated by the antenna divided by 4π"*. Putting the definition into a mathematical expression, this means (expression 2-16 in [20]):

$$D\left(\varphi_r, \theta_r\right) = \frac{4 \cdot \pi \cdot U\left(\varphi_r, \theta_r\right)}{P_{rad}} \quad \text{(Eq. 5)}$$

Using (2) and (4), it is possible to accommodate the normalized values in (5):

$$D\left(\varphi_r, \theta_r\right) = \frac{4\cdot\pi\cdot r^2\cdot\rho_{Norm}\left(\varphi_r,\theta_r\right)\cdot C}{P_{radNorm}\cdot C} = \frac{4\cdot\pi\cdot r^2\cdot\rho_{Norm}\left(\varphi_r,\theta_r\right)}{P_{radNorm}} \quad \text{(Eq. 6)}$$

It is common to refer to the directivity as the maximum directivity; in this case, (6) turns into (7), since $\rho_{NormMax}$ =1.

$$D_{max} = \frac{4\cdot\pi\cdot r^2}{P_{radNorm}} = \frac{1}{\frac{P_{radNorm}}{4\cdot\pi\cdot r^2}} = \frac{1}{P_{MeanRadNorm}} \quad \text{(Eq. 7)}$$

The mean power radiated normalized ($P_{MeanRadNorm}$) could be derived from a 3D radiation pattern measurement. Note that directivity is dimensionless and has a minimum value of 1, which happens when the antenna has the same normalized power density in all directions, that is, an isotropic antenna.

The efficiency (η) of an antenna is a measure that relates the power inserted into its terminals and the power radiated by it, if it is being used as a transmitter; similarly, if it is being used as a receiver, this parameter relates the power coming from the free space and the power delivered to a matched guided circuit. The maximum value of η is 1; when this occurs, no energy is lost, and the antenna acts as a perfect transducer. The minimum value is 0, which means no power transfer. The reduction of the antenna efficiency is a result of its metal and dielectric losses (impedance mismatch is not considered).

Another parameter widely used in antennas is the gain (G). It has the same interpretation as directivity, but takes into account antenna losses. The general expression is given below; as with directivity, it's common to use the term "gain" as the maximum gain of an antenna.

$$G\left(\varphi_r, \theta_r\right) = \eta \cdot D\left(\varphi_r, \theta_r\right) \quad \text{(Eq. 8)}$$

An equivalent way to represent the gain when the antenna is in the receiving position is through the antenna effective area (A_e). It's an intuitive method to describe the capturing characteristics of the antenna and is particularly useful to us, since this property relates the power density presented at the antenna aperture with the power available at the antenna terminals (P_{avs}). The relations between P_{avs} , gain and effective area are given in Eqs. 9, 10 (expression 2-115 of [20]) and 11.

$$A_{e_{RCV}}\left(\varphi_r, \theta_r\right) = \frac{P_{avs}\left(\varphi_r,\theta_r\right)}{\rho} \quad \text{(Eq. 9)}$$

$$G_{RCV} = \frac{4 \cdot \pi \cdot A_{e_{RCV}}}{\lambda^2} \quad \text{(Eq. 10)}$$

$$G_{RCV} = \frac{4 \cdot \pi \cdot P_{avs}\left(\varphi_r, \theta_r\right)}{\lambda^2 \cdot \rho} \quad \text{(Eq. 11)}$$

2.2.3 Polarization Pattern

An electromagnetic wave consists of an electric (E) vector field coupled to a magnetic (H) vector field. For this wave in a isotropic medium (eg. air), far from any metallic or scattering region, both vectors remain perpendicular to each other during the trajectory, oscillating and rotating around the propagation direction, in an unchanging pattern; the cross product between them always points to the propagation direction. This means that knowing the pattern of one of the vectors (a function of space and time), the other is determined. The polarization of an electromagnetic wave is defined according to the direction of the E vector field, and specifies [23, page 16] "*the shape, orientation, and sense of the ellipse that the extremity of the field vector describes as a function of time*". An example of this vector curve trace is shown on the left of Fig. 12; the observer's view in the propagation direction is shown in the right image of the same figure. In general, the polarization forms an elliptical pattern; linear and circular are special cases of that.

Figure 12: polarization pattern of a propagating wave.

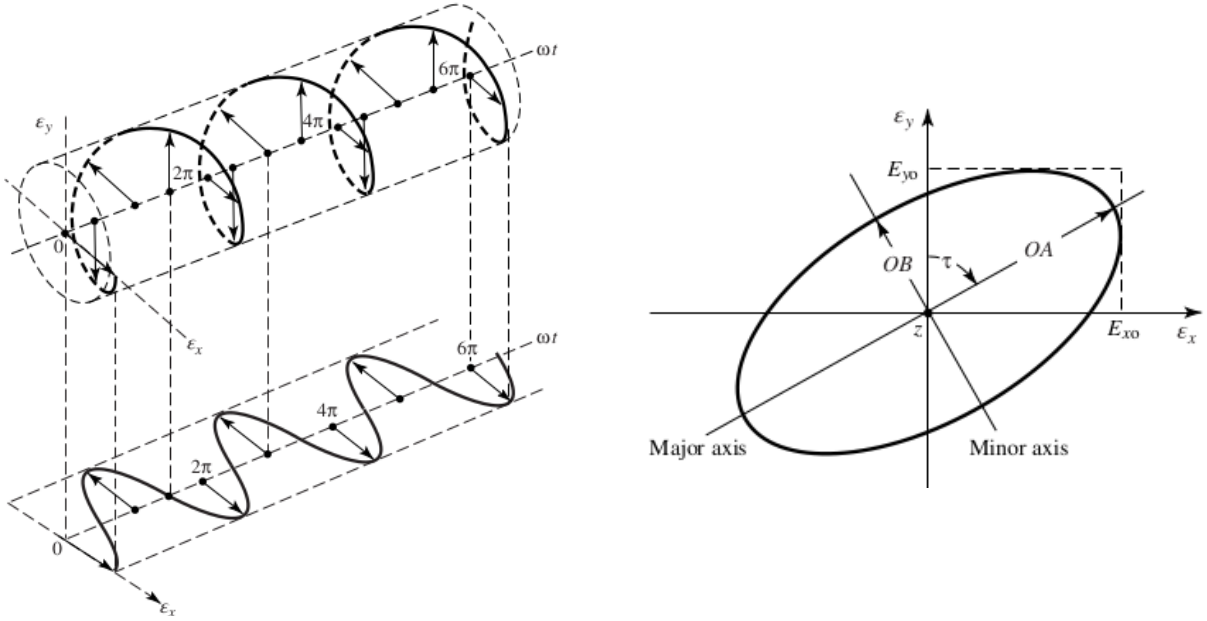

Source: [20]. In the image on the left, the curve traced by the electric vector field vector is shown. In the image on the right, it is shown the pattern of this vector field when the observer is in the propagation direction; normally, this pattern forms an ellipse.

The polarization of an antenna is defined as [23, pages 66 and 67]: "*the polarization of the wave transmitted by the antenna"*. However, as the polarization of electromagnetic waves emitted by a real antenna varies depending on the relative position (function of θ_r and φ_r) between observer (receiving antenna) and radiating antenna [20], the polarization of the antenna is usually defined as the polarization of the radiated electromagnetic wave at the direction of maximum directivity.

All these definitions are extremely important because antennas only receive signals that align with their polarization. This means that a linear polarized antenna with vertical polarization will only receive signals that contain the electric field vector in the vertical direction; in turn, a circularly polarized antenna will admit signals whatever the wave polarization pattern.

As commented, the polarization of real antennas varies with the relative position between antenna and observer. A figure of merit that deals with this quality is the antenna polarization pattern. This measurement is similar to the 2D radiation pattern, but at each spherical coordinate position, the direction of the electric field of the incoming wave is modified in a controlled way. This is done using a linearly polarized RA, such as a horn antenna; rotating it around its own axis will allow the direction of the radiated wave's electric field to change. In this kind of measurement, if the measured points for a given relative spherical position completely overlap, the AUT is circular polarized in that relative position; the farther one measured point is from the other, the more linear the polarization will be. *Axial ratio* is defined as the ratio between the highest and lowest power received at each relative position of the setup. In a circular polarization, the *axial ratio* would be ideally 0 dB; in a linear polarization, it would be ideally infinite.

2.2.4 Scattering Parameter (S-parameters)

The reader can find an extensive explanation about what are and how to measure scattering parameters at [25]. It is intended, in this way, to simplify the text showing only in which situations these parameters are used in the design and analysis of antennas. Among all the S-parameters, the most important for antennas is the *S11* which could be easily converted into input impedance and reflection coefficient. The designer could use this information for matching purposes. It is also an indicator of an antenna's operating frequencies.

To measure this parameter, it's first necessary to perform a one port calibration. This process involves a contact and measurement sequence between the probe and devices on a well-characterized calibration substrate. For the sake of saving time and ease of handling, this measurement is easier to carry out in a microprobe station, and should be done in the antenna characterization system only when the metallic chuck of the former interferes with the measurements. An example of such a case is in antennas that radiate downwards, that is, in the opposite plane to the pads.

2.3 Antenna Measurement Practice

2.3.1 Radiation and Polarization Patterns

As stated in Section 2.2.1, the radiation pattern measurements are interested in the normalized power density as a function of the relative position between RA and AUT. Let's assume the scenario where the AUT is radiating and the RA is receiving the signal. The mismatch and path loss between RA and the load representing the receiver is called L_{path}, which is a positive number lower than 1 and is the same for any relative position. This way, it is possible to measure the normalized power density using Eq. 9, as shown below:

$$\rho_{Norm}(\varphi,\theta)=\frac{\rho(\varphi,\theta)}{\rho_{max}}=\frac{\frac{P_{avs}(\varphi,\theta)}{A_{e_{RA}}}}{\frac{P_{avsMAX}}{A_{e_{RA}}}}=\frac{P_{avs}(\varphi,\theta)}{P_{avsMAX}}\cdot\frac{L_{path}}{L_{path}}=\frac{P_{L}(\varphi,\theta)}{P_{L\_MAX}} \quad \text{(Eq. 12)}$$

Where P_L and P_{L_MAX} are the instrument receiver reading values for a given relative spherical position (φ,θ) and at the maximum power received position, respectively. In decibels, Eq. 12 becomes:

$$\rho_{Norm}(\varphi,\theta)[dB]=P_{L}(\varphi,\theta)[dBm]-P_{L\_MAX}[dBm] \quad \text{(Eq. 13)}$$

This is a simple but powerful result. It tells us that to measure the AUT generated normalized power density at the receiving antenna aperture, it is enough to normalize the power readed by the instrument connected to it, no matter what or how many linear devices are between them. The algorithm for the 3D radiation pattern is shown in the flowchart of Fig. 13. The 2D radiation pattern, and the polarization pattern procedures are subsets of this most complete one. The user decides what is the start, step and stop points for the elevation and azimuth

coordinates. This will define the sub-area of the complete spherical shell that will be measured, as well as the distance between the samples. For each spherical position, the polarization motor rotates the RA to find the maximum coupled power between antennas, ie. the maximum received value. After all the interesting points were measured, the received values are normalized by the maximum one. This will transform the power matrix (dBm), into a normalized power density matrix (dB).

Figure 13: Flowchart explaining the radiations and polarization patterns measurement.

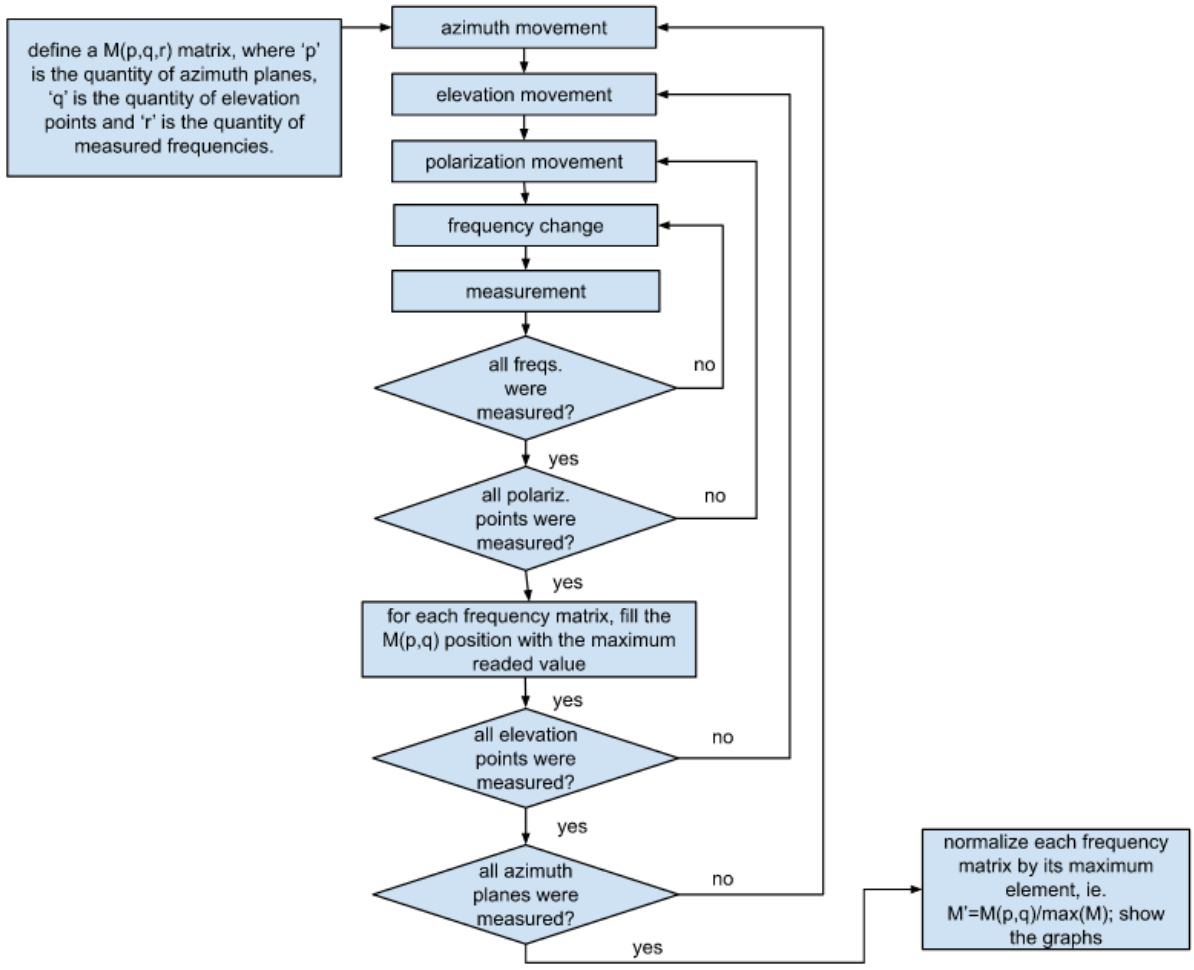

Source: author.

2.3.2 Directivity, efficiency and gain

To determine the gain, the system will use the comparison method ([20], page 1006). In this method, the maximum values of received power are obtained using two different setups: one of them using the usual test setup and the other by replacing the AUT with a standard horn antenna ("standard"), well characterized by its datasheet. These setups are compared in Fig. 14. The S_{STD} and S_{AUT} blocks are the passives devices used to adapt and connect the output guided wave of the antennas to the

receiver. These connections are usually different from each other, as the standard antenna is a waveguide horn and the AUT will most likely have CPW pads.

Figure 14: Comparison method for gain measurement.

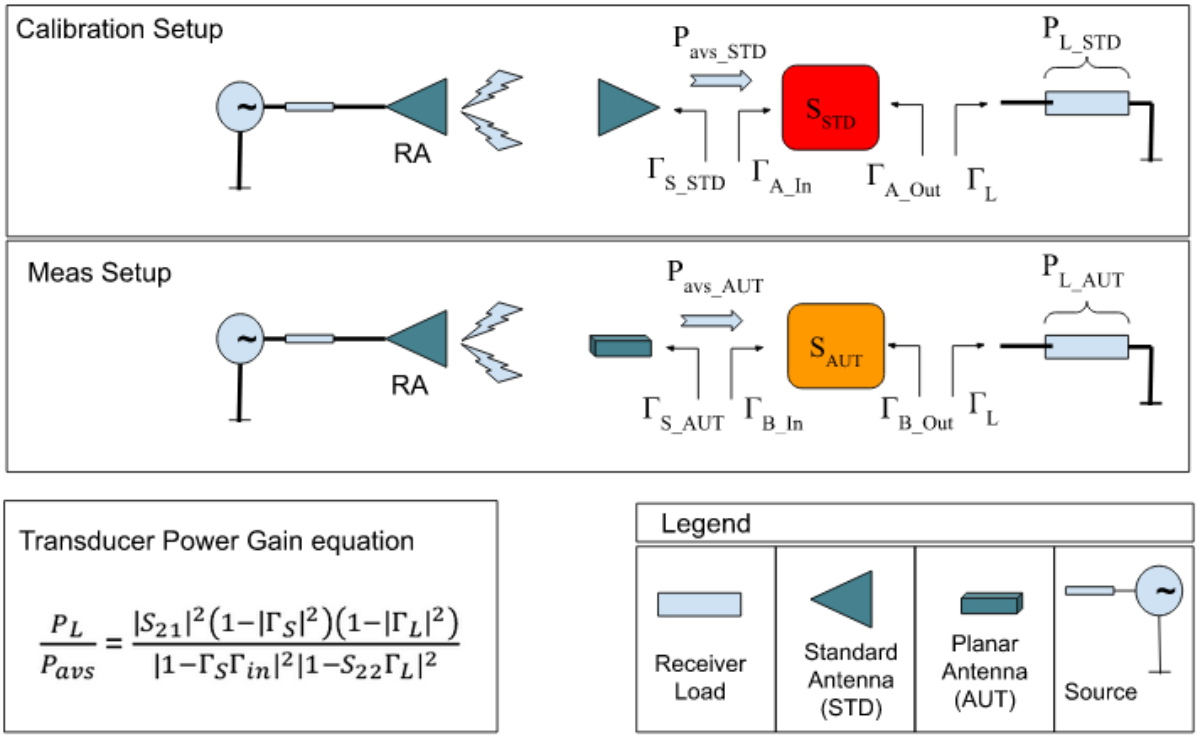

P_L: power delivered to the load (read at the receiver)

P_{avs}: power available at the source (receiver antenna)

Source: author.

Manipulating S-parameters, it is possible to derive an expression (transducer power gain in [24]) that relates the power delivered to the instrument's receiver and the power available at the output of the test antennas for both setups. Combining both equations and using Eq. 11, one can deduce an expression in which the only unknown is the gain of the AUT. However, the laboratory does not have the necessary tools to calibrate and measure the reflection coefficients of the majority of the devices presented in the figure, and these devices datasheets mostly do not show all the necessary features in the datasheets. For example, the datasheet of the cables and probes only shows measured graphs of S11 and S21. These are indeed reciprocal components, but there is not enough information to find the output reflection coefficient.

That said and considering that all the equipment used between AUT (and STD) and power receiver in this work are metrology grade, this work will disconsider the errors caused by the mismatch losses during the gain measurement, and will only

consider the insertion loss data of them. In this work, this is the meaning of “path losses for gain measurements”, as opposed to “path losses defined for the radiation pattern” (section 2.3.1), which take mismatch losses into account. Using Eq. 11, it is possible to find the relationship between received power and antenna gain:

$$P_{L\_MAX\_STD} = P_{avs\_MAX\_STD} \cdot L_{STD} = \frac{\rho \cdot \lambda^2}{4 \cdot \pi} \cdot G_{STD} \cdot L_{STD} \quad \text{(Eq. 14)}$$

Where G_{STD} is the gain of the standard antenna, referenced by the manufacturer in the datasheet. The absence of coordinates in this expression means that the measurement is made at the relative position of maximum coupling between the antennas. In decibels, this expression becomes:

$$P_{L\_MAX\_STD}[dBm] = 10 \cdot log_{10}\left(\frac{\rho \cdot \lambda^2}{4 \cdot \pi}\right) + G_{STD}[dBi] + L_{STD}[dB] \quad \text{(Eq. 15)}$$

For the AUT, a similar equation is given by:

$$P_{L\_MAX\_AUT}[dBm] = 10 \cdot log_{10}\left(\frac{\rho \cdot \lambda^2}{4 \cdot \pi}\right) + G_{AUT}[dBi] + L_{AUT}[dB] \quad \text{(Eq. 16)}$$

Subtracting equation 15 from equation 16 results in:

$$P_{L\_MAX\_AUT}[dBm] - P_{L\_MAX\_STD}[dBm] = G_{AUT}[dBi] - G_{STD}[dBi] + L_{AUT}[dB] - L_{STD}[dB]$$

and, rearranging the terms, the AUT gain can be obtained by:

$$G_{AUT}[dBi] = P_{L\_MAX\_AUT}[dBm] - P_{L\_MAX\_STD}[dBm] + G_{STD}[dBi] + DGPL[dB] \quad \text{(Eq. 17)}$$

Where the Difference in Guided Path Loss (*DGPL*) between the standard antenna setup measurement and the AUT (planar) setup is given by:

$$DGPL[dB] = L_{STD}[dB] - L_{AUT}[dB]$$

For this calculation, the insertion loss values of each path component is obtained from its datasheet. It is important to remember that losses are positive values. Typically, these datasheet information are for generic batch components, and are presented in a graphical format, with frequency in the ‘x’ axis. For the *DGPL* calculation, these graph data were fitted into linear functions.

One last thing needs to be said about the gain definition and measurement. Zeroing all the reflection coefficients presented in Fig. 14 for the purpose of measurements brings this work definition of gain much closer from the realized gain than for the classic gain [23]. But, as we will see in the accuracy calculations (section 4.2), the errors associated with either of these two definitions in this setup are roughly the same, so we will not make that distinction.

One challenge for this measurement is to align the RA for a maximum coupling position. This can only be obtained automatically via a brute force method, in which the maximum coupling is sought through several measurements, with the simulated boresight as an initial estimate point. In fact, the measurement of the 3D radiation pattern already gives us this maximum coupling position. That is why it is a good practice to perform this measurement before a gain measurement.

To obtain the antenna gain for any position, Eq. 16 is modified to:

$$P_{L\_AUT}(\varphi,\theta)[dBm] = 10 \cdot log_{10}(\frac{\rho\cdot\lambda^2}{4\cdot\pi}) + G_{AUT}(\varphi,\theta)[dBi] + L_{AUT}[dB] \quad \text{(Eq. 18)}$$

Subtracting Eq. 16 from Eq. 18:

$$P_{L\_AUT}(\varphi,\theta)[dBm] - P_{L\_MAX\_AUT}[dBm] = G_{AUT}(\varphi,\theta)[dBi] - G_{AUT}[dBi]$$

rearranging the terms and using the normalization of Eq. 13:

$$G_{AUT}(\varphi,\theta)[dBi] = G_{AUT}[dBi] + \rho_{Norm}(\varphi,\theta)[dB] \quad \text{(Eq. 19)}$$

which gives the gain in any direction, as a function of the radiation pattern and the maximum gain of the antenna.

Until the conclusion of this dissertation, the algorithm for calculating the directivity, and later the efficiency, was not ready.

3 Antenna Characterization System

3.1 Overview

A good understanding of equipment and setup is essential to extract their maximum potential, extend their useful life and track the sources of measurement errors. In this work, this explanation is divided into two parts: electromagnetic and electromechanical. The first one will explain the instruments, their connection and configuration, and discuss the strengths and limitations of the presented solution. The second will explain the physical movement of the antennas and the actuators behind it, besides talking about the possible causes of misalignments.

3.2 Electromagnetic

3.2.1 Vector Network Analyzer (VNA)

The VNA is a device that combines the attributes of a source and a tracking (tuned to the source) spectrum analyzer to produce a stimulus/response pair of a device under test. In addition to the scattering parameters, a VNA is capable of generating numerous other useful results, such as noise figures, intermodulation products, compression points, TDR (time domain reflectometer) and much more. It is arguably the most complex electronic instrument.

The mmW Center's vector network analyzer is from the PNA-X series, identified in this family by the part number N5247B. This basically defines the parameter “minimum and maximum operating frequency” of the equipment, and, consequently, the base hardware, such as the type of connector of the test ports.

A number of options are offered by the manufacturer to complement the base hardware of the N5247B. In the case of Center’s equipment, hardware options 401 and 20 give access to an extra source (“Source 2”, in Fig. 15) and to connectors (“jumpers”) on the rear panel, respectively. In Fig. 15, there is a simplified block diagram of the hardware. It is extremely important to understand what each of the receivers in this scheme means. There are two types of them: *reference receivers* and *test receivers*. For *reference receivers*, the number after the letter “R” tells which port it is referring to: “R1” measures the signal that comes out of port 1. For *test receivers*, “A” measures power entering on port 1, “B” measures power entering on port 2, and so on. Table 1 summarizes the function of the VNA receptors.

Figure 15: Simplified block diagram of the vector network analyzer available at the Center.

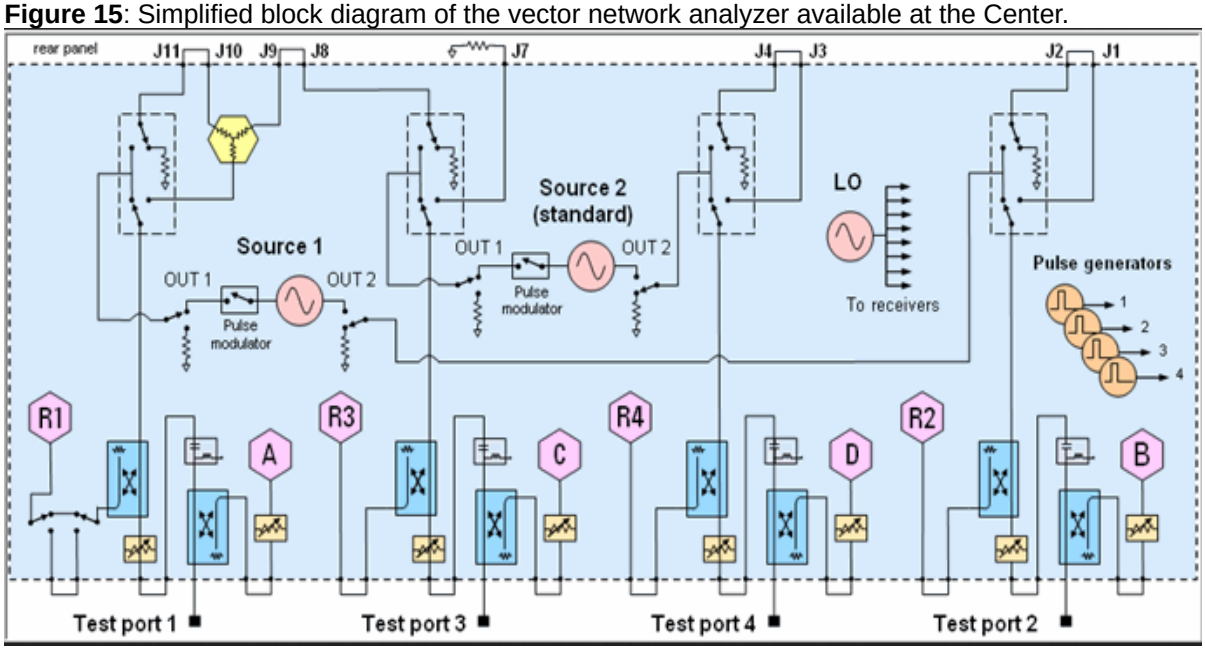

Source: Equipment technical specifications [26].

Table 1 - Types of receivers present in the VNA.

RECEIVERS	TYPE	EXPLANATION
R1, R2, R3, R4	Reference Receivers	Measures the signal that leaves the VNA and enters the DUT
A, B, C, D	Test Receivers	Measures the signal that leaves the DUT

Source: author.

All measurements made by the VNA are based on relations of values read from the receivers; measurements are either ratios between two receiver values (“ratioed”) or the receiver value itself (“unratioed”, or “absolute power”). S-parameters are examples of “ratioed” measure: S11 is A/R1 [dB]. As an example of “unratioed”, there is the power arriving at port 3: D [dBm]. In fact, network analyzers are designed for scattering parameters measurements, which means that the hardware is optimized for "ratioed" measurements. There is no need for precise output signal levels at the source, nor an accurate reading of the signal at the receivers, as calibration procedures [25] are capable of removing errors associated with measurements. However, both the generated signal and the signal reading must be stable. Otherwise, "ratioed" measurements would not be possible; for example, if the source power changes and the receiver remains stable, there would be a variation in the measurement not caused by the DUT. This explains why the datasheet [26] does

not provide stability or reproducibility performances for sources or receivers, but only for ratio measurements, as is shown in Fig. 16. The more stable the source and receiver are, the longer the calibration will keep confidence.

As shown in previous sections, antenna measurements in this setup are “unratioed”. For this kind of measurements, it is most common to use power sensors (and meters) when precision is needed, and spectrum analyzers when one needs to know the spectral content of the signal. However, if normalized measurements are used, this would be equivalent to rationalizing the measurements, since source and receiver absolute level imprecision will be canceled. Consider, for example, measuring two points on a radiation pattern. The absolute measurement is a function of the source power, the power reading at the receiver and the absolute imprecision of both. If the source and receiver are stable, the difference between these two measurements would nullify the power of the source, the absolute imprecision of the source and the absolute imprecision of the receiver; the result would just be the relative difference in power between two points, that is what is needed.

Figure 16: Stability of VNA “ratioed” measurements.

Table 22a. Stability[1] – Typical

Description	Magnitude (dB/°C)	Phase (degree/°C)
10 MHz to 50 MHz[2]	0.05	0.4
50 MHz to 16 GHz[2]	0.01	0.2
16 GHz to 20 GHz	0.01	0.3
20 GHz to 50 GHz	0.02	0.7
50 GHz to 67 GHz	0.03	1.0
67 GHz to 70 GHz	0.05	1.1

[1] Stability is defined as a ratio measurement made at the test port.

[2] With Option 425 installed and LFE disabled, applied to frequencies ≤ 100 MHz. Above 100 MHz, performance is the same for both LFE enabled or disabled. For LFE enabled performance ≤ 100 MHz, see Table 22b.

Source: Equipment technical specifications [26].

The VNA runs an embedded Windows 10 operating system. Everything that is achievable on a regular desktop is also achievable on the VNA; Internet browsing through a browser is an example. The specific application for measurements is made through a software that runs on top of this operating system. Such software communicates with the hardware through calls to the operating system (system calls). The user can interact with the software through the mouse, keyboard or front panel (hardkeys and touch screen); or from another process, through the COM

(Component Object Model) mechanism provided by the operating system. In this last mechanism, the application offers an interface (set of methods) that should be used in the inter-process communication. For cases where the commands come from another computer, through SCPI commands (Standard Commands for Programmable Instruments [27]), there will be a server process that mediates between the network and the VNA application, translating the SCPI commands into COM, and vice versa in the path back. A simplified logic diagram illustrating user interaction with the hardware is shown in Fig. 17.

Figure 17: Logic diagram illustrating how the user has access to the hardware.

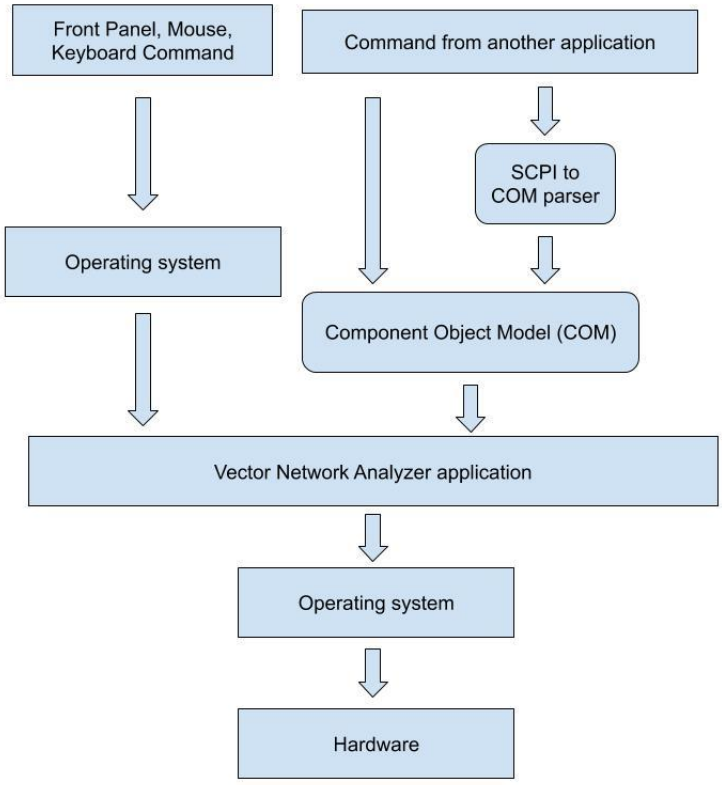

Source: author.

For the same hardware, a series of software options are sold by the manufacturer. These options are facilities released, through licenses, in the VNA application. As an example, the VNA has a signal reception circuitry similar to that of certain types of spectrum analyzers, but signal processing is required to eliminate spurious products between the local oscillator and the input signal. In Fig. 18, a continuous wave (CW) 5 GHz signal is inserted into port 1 of the VNA. There is, in the upper window, a spectrum analyzer measurement released by license; in the lower window, the input signal is measured with a conventional power meter (receiver

“A”, in Fig. 15). It’s not hard to see the difference between measurements made with the same hardware.

Figure 18: Two measurements of the same signal: the upper one makes use of the Spectrum Analyzer license, while the second one is a measurement of the input power.

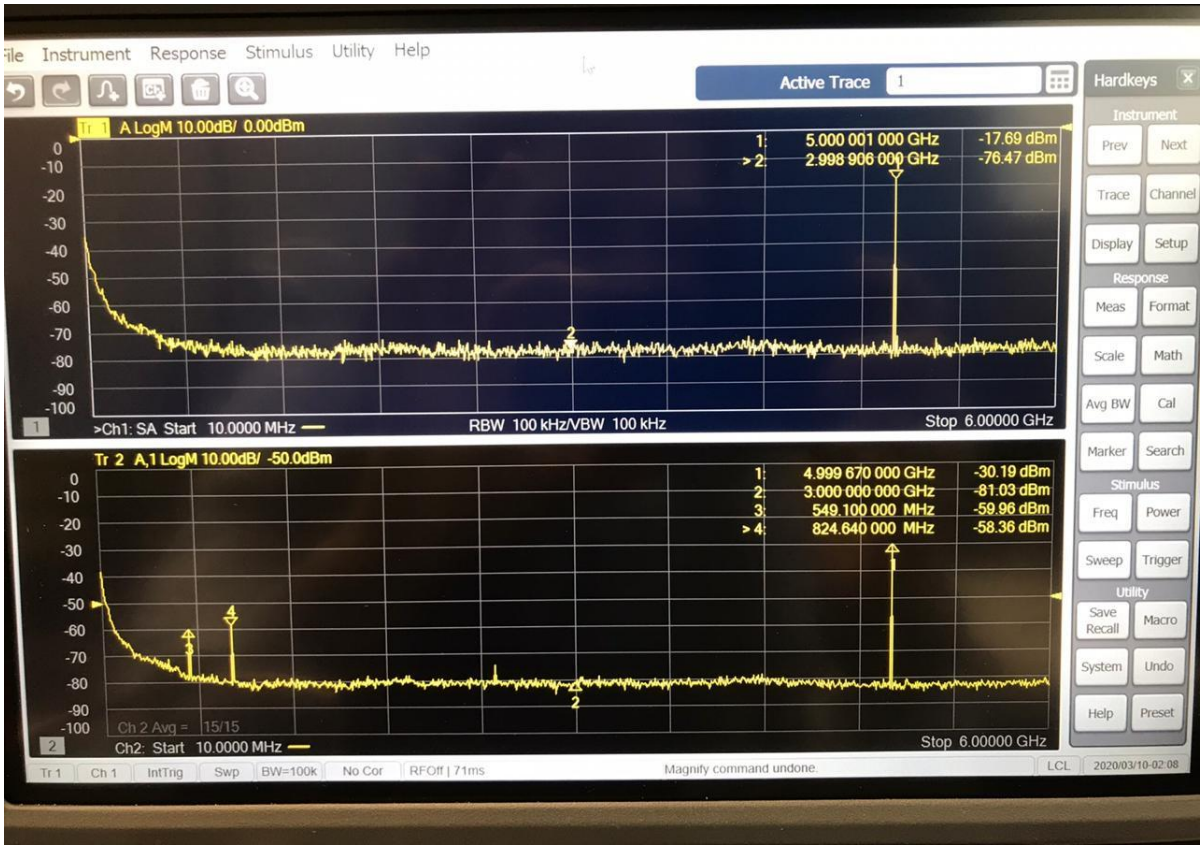

Source: author.

Finally, the license that the Center’s PNA has installed is the Frequency-Offset Measurement (identified by S93080B), which allows the source frequency to be different from that tuned by the receiver during “tracking”. This is important for this work, since this setup will be using mixers or frequency multipliers.

3.2.2 Frequency Multiplier

As normally happens to Millimeter Wave frequencies test equipment, the setup does not fully work on the frequencies at which the measurement is to be performed. The VNA generates a CW signal below 20 GHz, which is shifted up to the test frequency. After interaction with the DUT, if this frequency can be read by the VNA, such signal is directly connected to the receiver; otherwise, the signal is shifted down before entering the receiver. This configuration was chosen because the signal must travel over a long path of cables and coaxial connectors. These devices become

increasingly expensive and less efficient with increasing frequency. As an example, a 10 mm long, 1 mm inner conductor (rated to 110 GHz) coaxial cable costs thousands of dollars and has an insertion loss close to 2 dB at 100 GHz [28].

For the frequency up shift, it is possible to use a mixer or a multiplier. The mixer would need a local oscillator (LO) signal and a RF input, while the multiplier just needs the RF signal. For the sake of simplicity, the mmW Center's setup uses multipliers instead of mixers to up-shift the signal. The data available in the multiplier manufacturer's datasheet [29,30] is shown in Fig. 19.

Figure 19: Center's Multipliers datasheets.

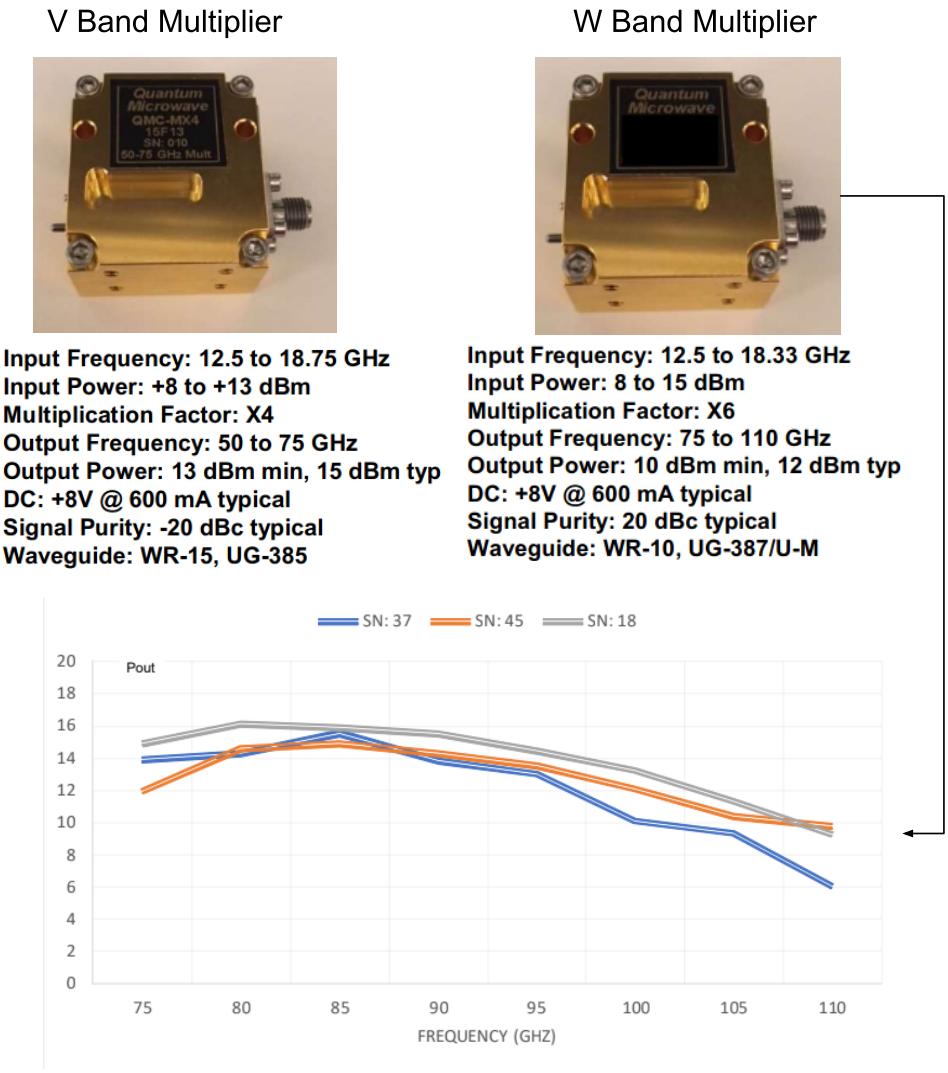

Source: manufacturer datasheet [29,30]. In the chart provided, the ordinate axis ("y-axis") refers to power, in decibel-milliwatts (dBm).

A positive point of these active multipliers is that, as long as the input power limits are respected, the output power is independent of this input value. This means that even if there is a power imbalance of the input signal caused by moving and

twisting the cables, this will not affect the test signal, which is generated in the multiplier. Again, it is not important to know the absolute value of this signal, but its stability is necessary.

3.2.3 Frequency Extender

It is not possible to directly read the W band signal through the VNA receiver. For measurements in this band, the signal must be downshifted before reaching the VNA. As for up-converting, two solutions exist: use a down-converting mixer or a frequency divider. As the laboratory already has frequency extenders, which are basically mixers, the first option was chosen. As will be shown in the next section, this step takes place very close to the VNA, in a region that remains stationary. Therefore, there is no increased assembly complexity compared to using frequency dividers.

Figure 20: Basic architecture of a frequency extender showing all the input and output signals.

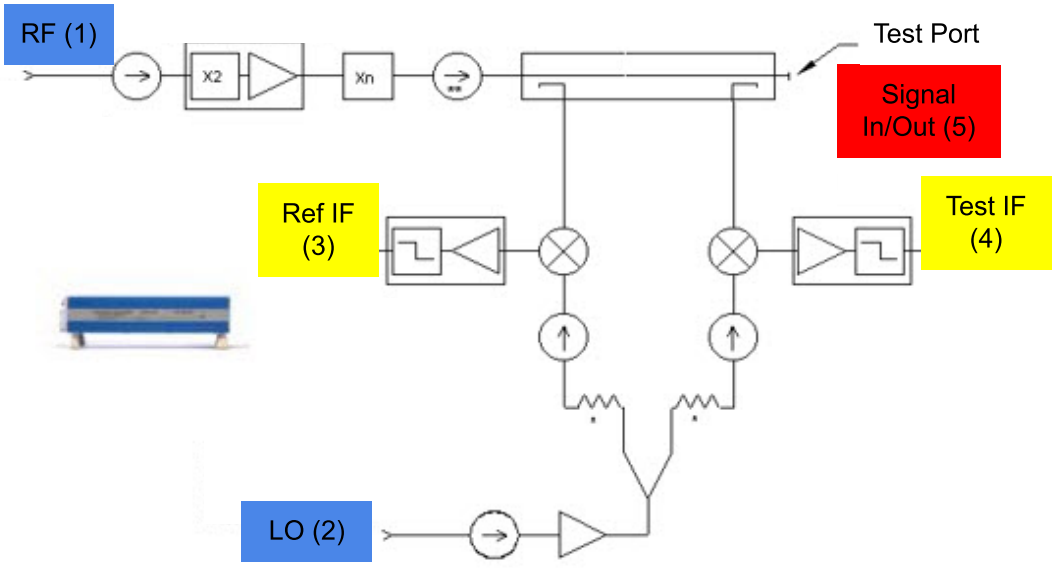

Source: Keysight PNA help file [31]. Annotations made by the author.

Frequency extenders use two mixers, amplification and frequency multiplier to be able to generate and acquire the forward and reflected waves on the frequencies of interest. For each DUT port, one frequency extender is required. The general block diagram is shown in Fig. 20. An external circuitry, often a VNA, feeds the extender with two different signals: RF and LO. Inside the extender, after individual multiplication, these two signals will have a very close frequency, so that the mixer downconverting combines them in a low frequency signal, represented by the IF

signal. The IF signal is correlated in amplitude and phase with the RF signal. Measuring the low frequency signal (IF) will allow us to know the characteristics of the high frequency signal (RF). Directional couplers are used to sample the RF forward and reflected signals; the later downconverting will create the *Ref IF* and *Test IF* signals, respectively.

Figure 21: Basic architecture of a frequency extender showing only the input and output signals used in the Center antenna measurement setup.

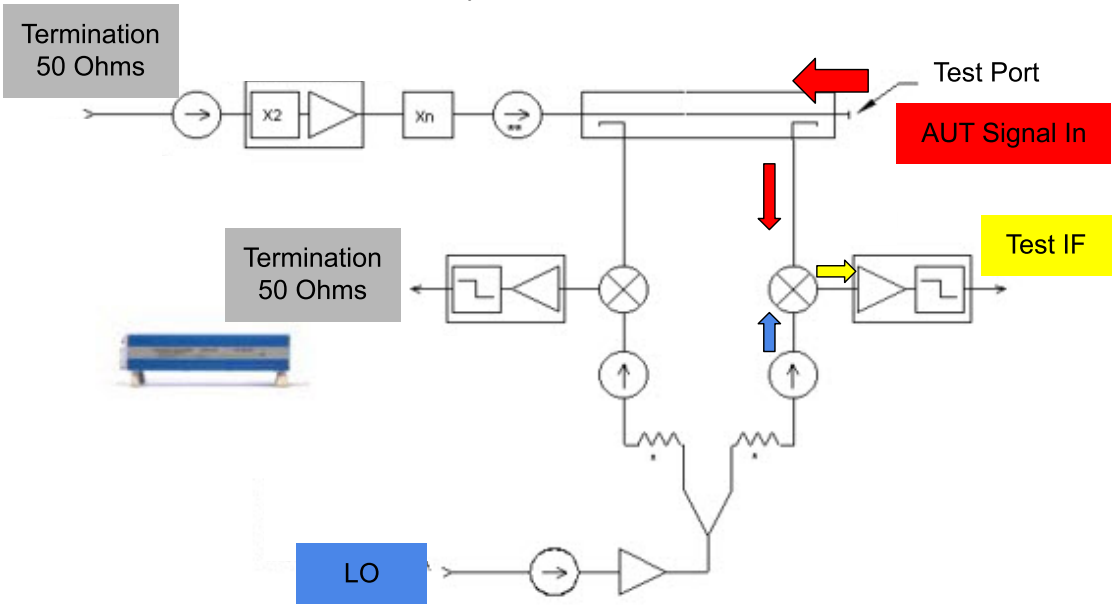

Source: Keysight PNA help file [31]. Annotations made by the author.

In the mmW Center's configuration, the frequency extender is used in a reception unidirectional scheme, where only the DUT reflected signal is important. This configuration is shown in Fig. 21. The W band signals coming from the AUT enters the Test Port (Signal In/out), then it is mixed with the resulting LO signal and gets out of the extender through the Test IF port.

To improve the explanation, let's use numbers. Suppose that an antenna operating at 100 GHz is being measured. This is the signal frequency at Test Port. The OML frequency extender [32] multiplies the LO signal by 8; let's fix the Test IF frequency as 100 MHz (as said, low frequency). Eq. 11 relates signal frequencies, and all values, except LO multiplier, are given in Hertz. This way, the VNA should be configured to output a LO signal of 12.512 GHz and read a signal at 100 MHz.

$$LO_{IN} = \frac{(TestPort + TestIF)}{LO_{mult}} \qquad \text{(Eq. 20)}$$

The physical connection between VNA and frequency extender is shown in Fig. 22. VNA's port 4 generates the LO signal, and the Test IF signal is connected

directly to the receiver B (table 1). As there is no need for the RF and Ref IF (Fig. 22) signals, those ports are terminated with 50 Ohms loads.

Figure 22: Center's connection between VNA and frequency extender.

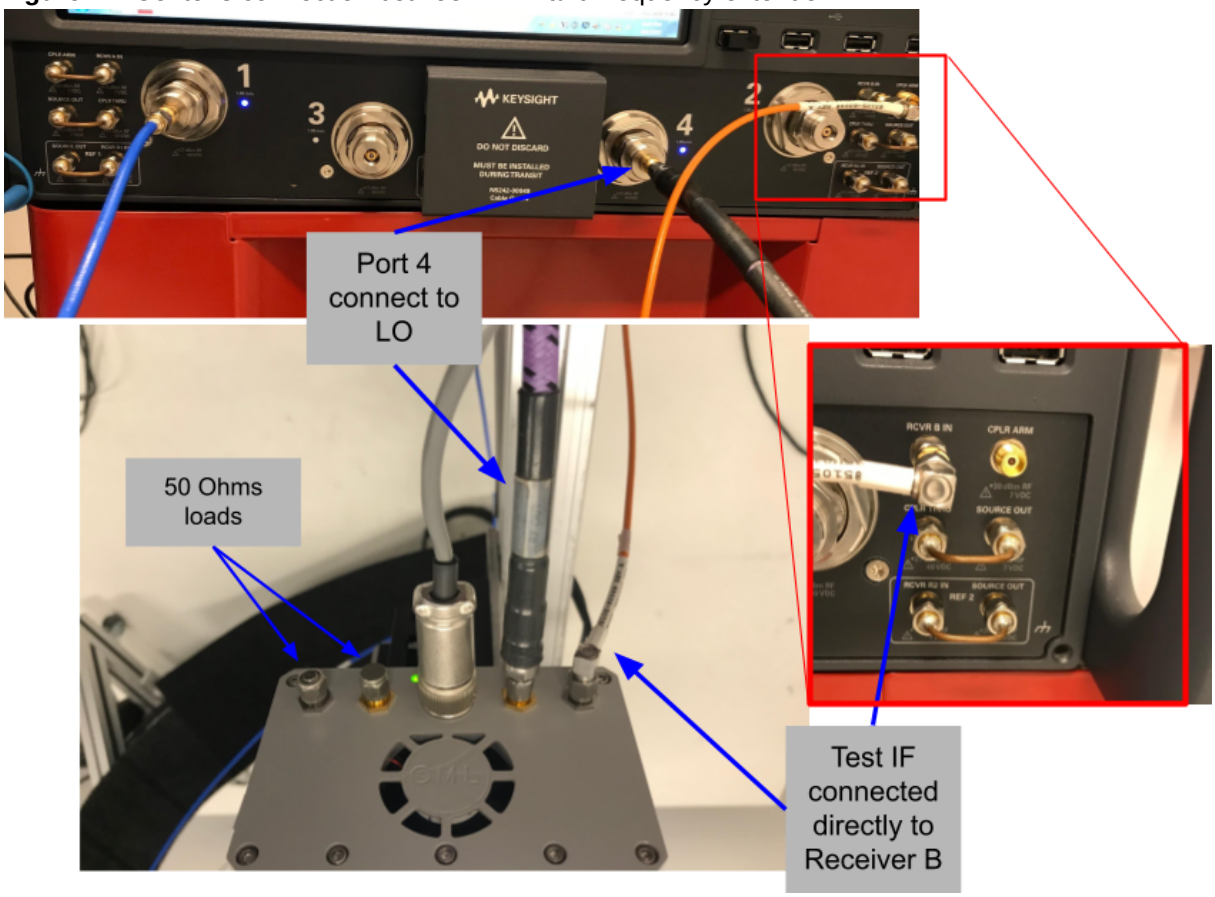

Source: author.

The concern about stability that was discussed earlier (VNA and multipliers) is also needed for this device. A linear correlation between the Test Port and the Test IF port signals amplitude is required, so that normalized measurements are not impaired. The instrument datasheet [32] claims for a stability of +-0.2 dB.

3.2.4 Signal flow

A block diagram of the electromagnetic devices configuration of the setup is summarized in Figs. 23 and 24. The first one is called V band setup for the reason that, based on the manufacturer specification of the components used, this must work from 50 GHz (lower limit of the multiplier and lower available data of the standard antenna) to 70 GHz (VNA settable upper limit), which are part of the V band frequencies. As normalized values are used, it is probably possible to extend the lower limit of this setup to the lower cutoff frequency of the WR-15 waveguide, which

is close to 40 GHz. Some tests must be done to find out if the multiplier does not have some type of filter for frequencies outside the specification, in addition to ensuring that the antennas are far enough apart for the far-field condition to be respected. For the same reason, the second one is called W band setup (Fig. 24). Although the lower frequency specification of the multiplier and the frequency extender is 75 GHz, our measurements confirmed that it is possible to use them up to 70 GHz.

It is important to notice that the antennas, probes and coaxial-waveguide converters are different between setups, as they are intended for different frequency bands and, therefore, their connections have different physical dimensions. In Fig 25, there is a photograph of the assembled V band setup; in Fig. 26, the W band setup is assembled. In both photographs the AUT is a standard horn antenna.

The improvements of this part of the system are shown below:

- ☑ Design and prototype of the parts that attach the rotating joints to the mechanical apparatus. In this way, the cables are not twisted during movement;
- ☑ Heat sink connected to the multipliers to prolong their useful life and avoid sudden changes in temperature;
- ☑ VNA configuration for frequency offset measurements.

Figure 23: Signal flow for the V band setup.

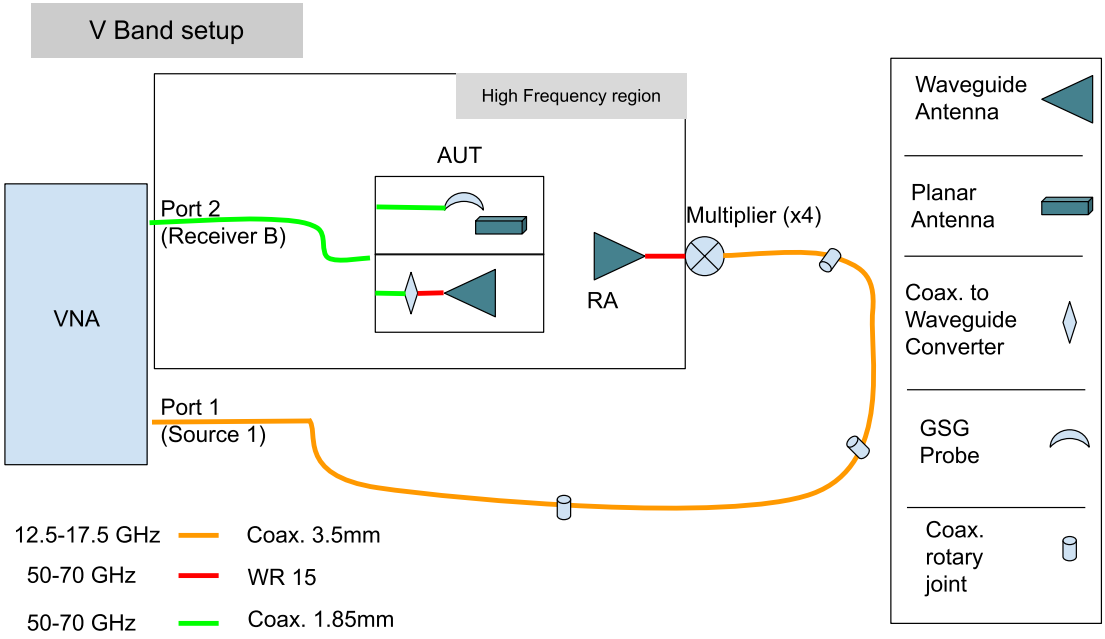

Source: author.

Figure 24: Signal flow for the W band setup.

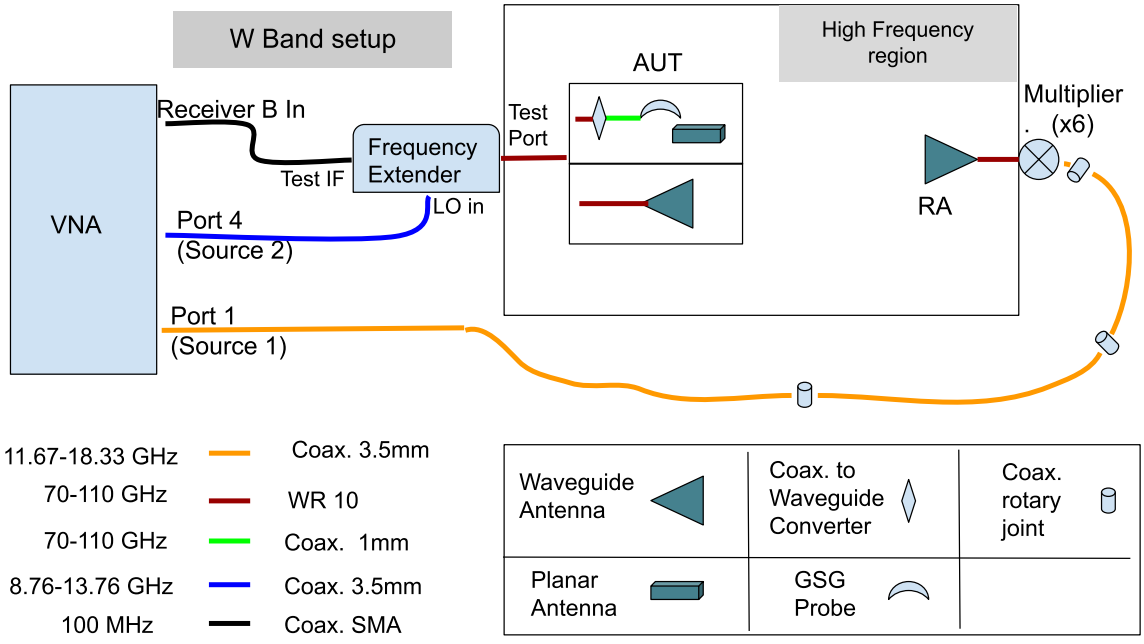

Source: author.

Figure 25: Center's antenna measurement system assembled in V band configuration.

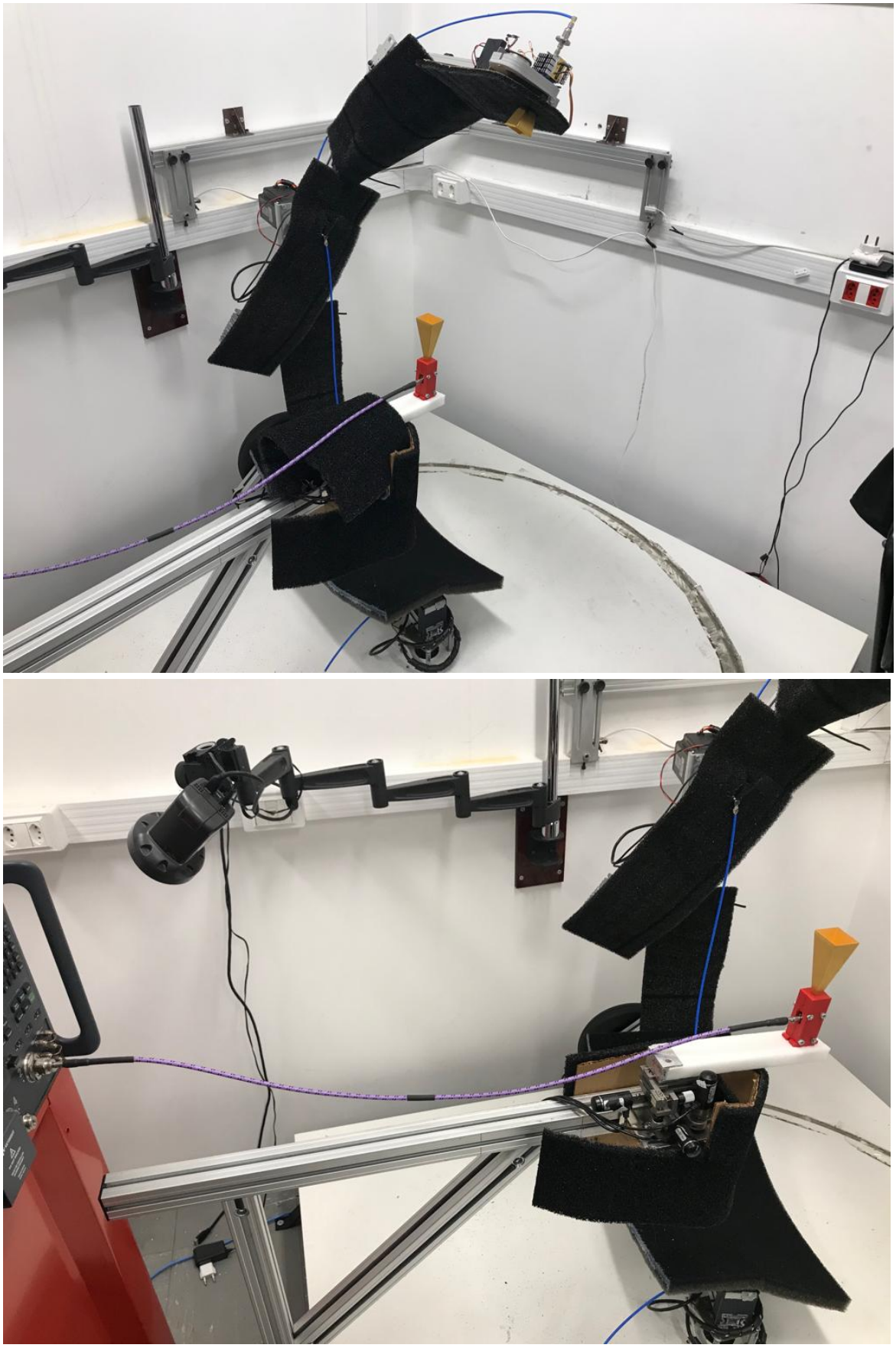

Source: author.

Figure 26: Center's antenna measurement system assembled in W band configuration.

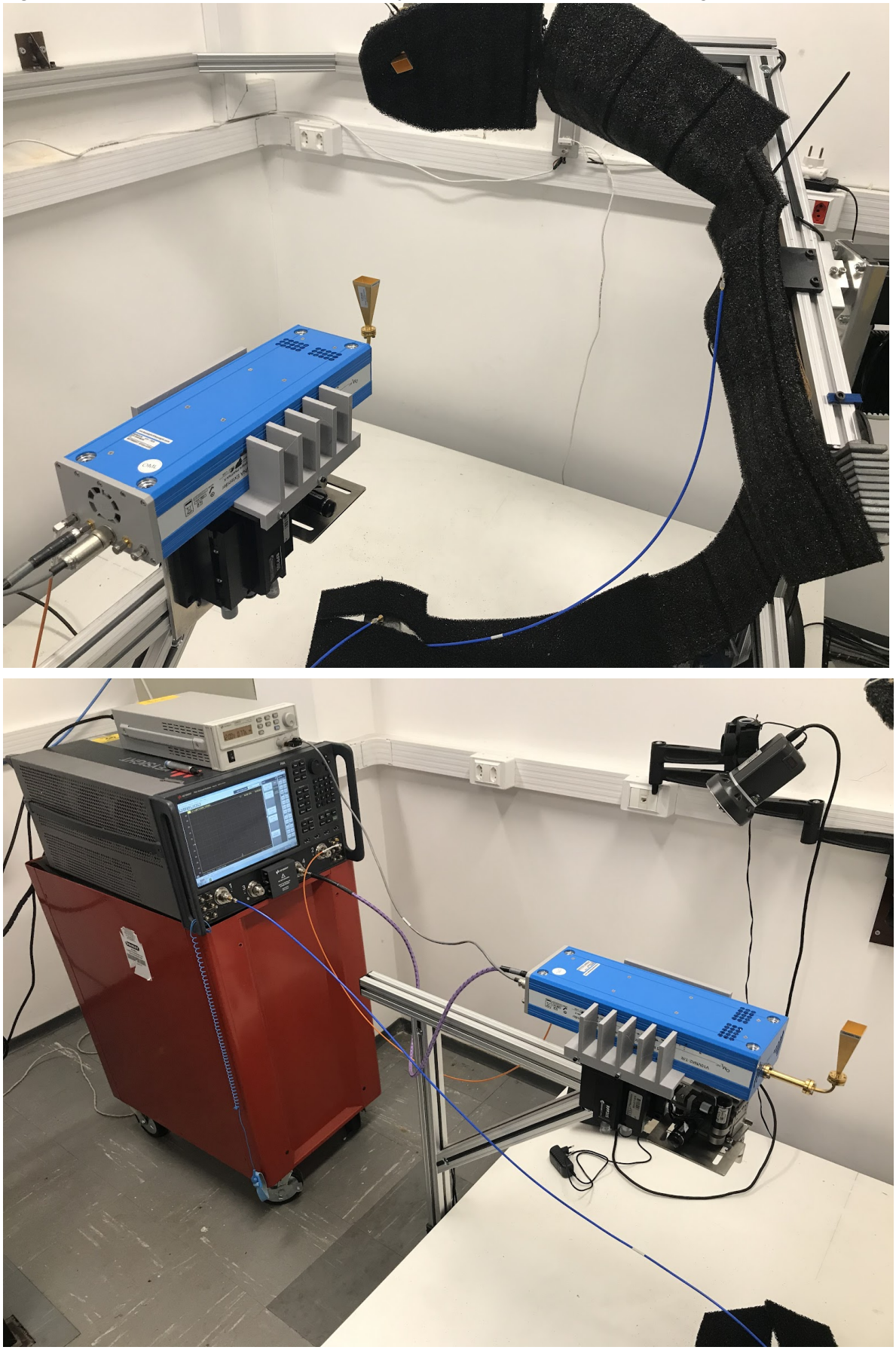

Source: author.

3.3 Electromechanical

3.3.1 Reference Antenna

As stated in Section 2, the configuration must supply a plane wave with constant power density at the center of the spherical coordinate system. The direction of arrival and the polarization of this wave must be controllable. This is done by moving the RA through a spherical shell of constant radius; in the setup of the Center, this movement is done through the mechanical apparatus shown in Fig. 27. There are two rotation axis, whose movements are automatically provided by two stepper motors, called here azimuth motor and elevation motor, for obvious reasons. Imagine moving the elevation motor while not acting the azimuth motor: the RA will follow a path according to the elevation angle in Fig. 9. In the same way, keeping the elevation motor static and varying the step of the azimuth motor, the RA will follow a path in which only the azimuth angle will be modified.

Figure 27: Mechanical apparatus for the RA spherical movement.

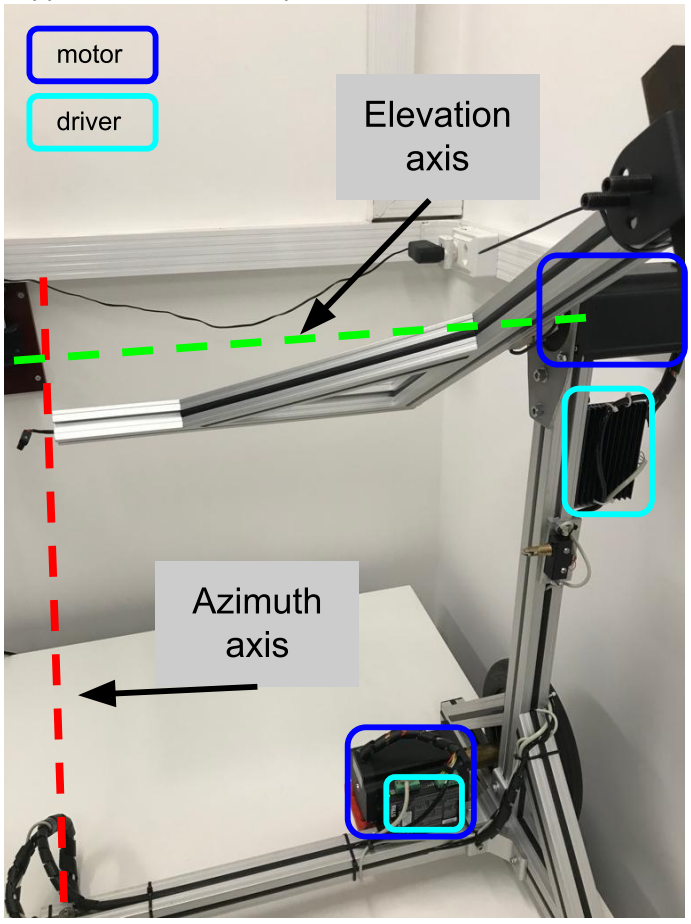

Source: author. The axis represents the elevation and azimuth variables. Each axis movement is controlled by a stepper motor.

One motor driver is used to control each motor; one microcontroller is used to control both drivers. It is an open loop control, that is, the microcontroller generates each of the step commands, but has no feedback on whether the step was performed. So, it is necessary to guarantee the integrity of the step signal: control cables must be shielded, and attention should be paid to the occurrence of possible electromagnetic interference. The only feedback is performed through end-of-travel switch, one for each motor, which are used to give an RA absolute position notion, such as (0,0). Although the sensors are not that precise, making the mechanical arms search for the sensor with a fixed direction of rotation, always using the same speed, allows the setup to have an excellent position repeatability. As the elevation arm is directly connected to the motor shaft, the elevation movement will have the same step resolution as the stepper motor, which in this case is 0.018°. The more balanced the elevation arm, i.e. the less axial torque on the motor shaft, the more accurate and smooth this step will be. The azimuthal motion, however, is transmitted to the metal apparatus through a wheel. This makes it very difficult to define a resolution for the azimuth movement. In this case, tests were made to estimate the step/degree ratio.

To enable the control of the polarization of the incoming wave, the RA must rotate around its own axis, that is, around the normal of its aperture. A complex structure (Fig. 28) was developed to connect the RA to a bearing; this assembly is coupled to a gear, which in turn is connected to the shaft of a third stepper motor via a belt. This motor is called polarization motor. This modular solution allows to quickly modify the measurement band, in addition to enabling future expansion of the setup to higher frequency bands. An illustrated tutorial is given in Appendix A showing the steps needed to replace the RA structure when changing frequency band measurement.

The intersection between azimuth axis and elevation axis defines the center of what will be called the RA coordinate system (*RACS*), as shown in Fig. 29. The setup has two sources of misalignment: they are defined as *RA_d1* and *RA_d2*. They are basically the misalignment between the normal axis of the RA horn aperture when the RA is set to the position (0,0) and the azimuth axis. The *RA_d1* error is a translational error; it is easy to see that when this misalignment occurs, the RA will not travel the whole spherical shell; for example, the (0,0) point will never be reached. The *RA_d2* error is a rotational error, but it is not easy to see what it causes

to the measurements. It is important to make it clear that both errors are visually imperceptible, but causes disturbance on the measurements, since the system works in a wide power range, around 0 to -60 dBm. Section 4 will discuss a procedure to reduce to a satisfactory level the errors associated with these misalignments.

Figure 28: RA mechanical apparatus.

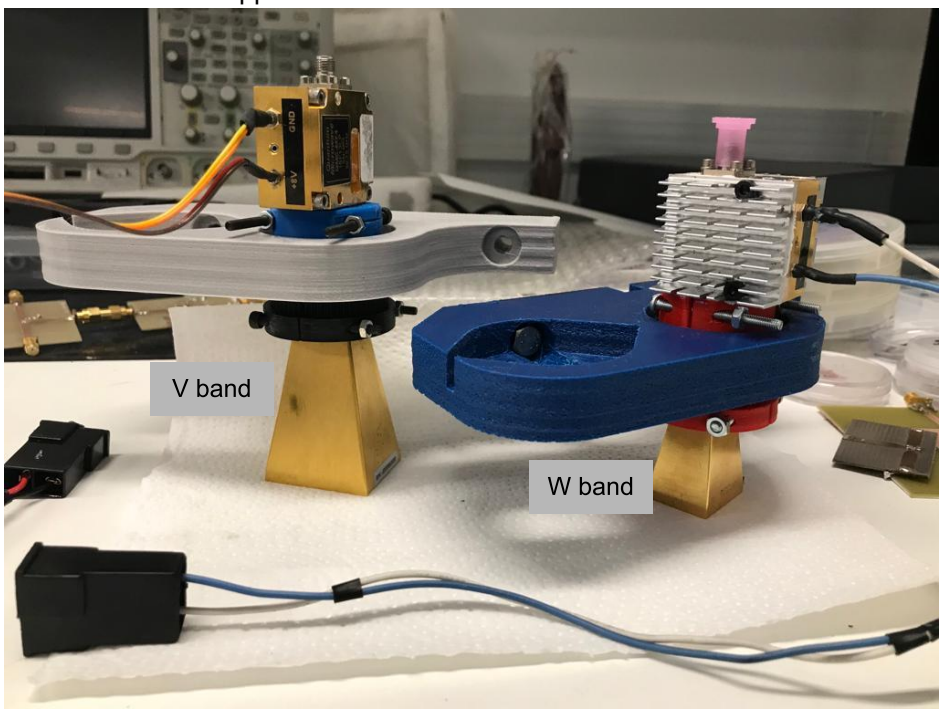

Source: author. The shown support enables the rotation (around its own axis) of the RA. This allows the control of the polarization of the incoming wave, as the RA is a linear polarized antenna. For each measurement band, one of them must be built.

Figure 29: Drawing showing the misalignment sources of the RA apparatus.

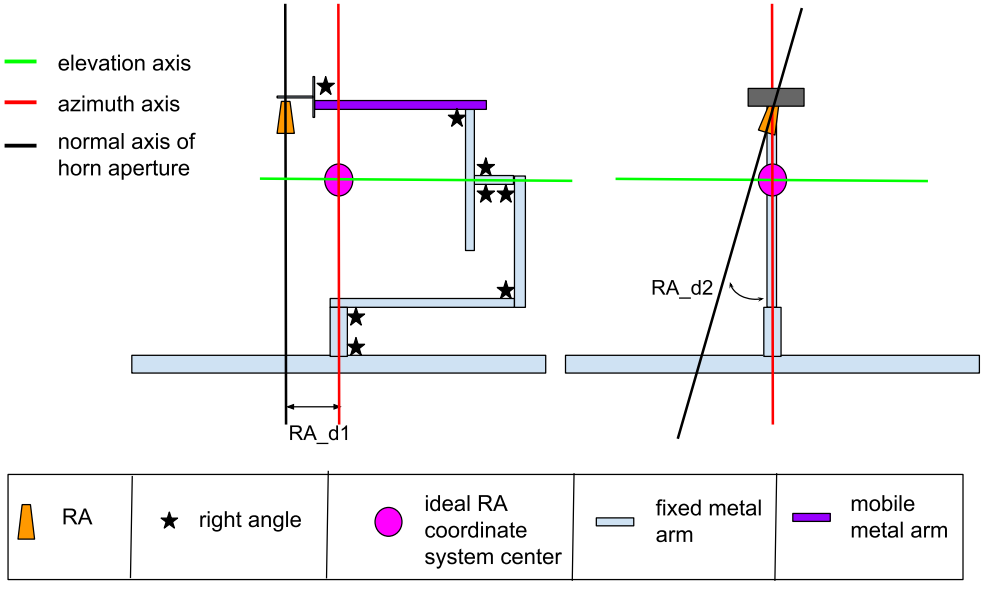

Source: author. These error sources undermine the assumption made about the wave arriving at the center of the RACS.

The improvements of this part of the system are shown below:

- ☑ New less invasive end-of-travel switch, for both the elevation and azimuth motors;
- ☑ New step motor to control the polarization of the incoming wave. It is called the “polarization motor”. This permits the system to perform 3D radiation patterns and 2D polarization patterns;
- ☑ Shield and ferrite at the control cables susceptible to EMI, such as the control signals of the polarization motor driver, or frequency multiplier power cord. Both are subject to noise from signals from other motors;
- ☑ RA support was totally modified to accommodate the rotational movement. All the parts were designed in FreeCAD and prototyped in a 3D printer;
- ☑ Study and placement of broadband Millimeter Wave absorbers on metal surfaces that have proven to interfere with measurements;
- ☑ Several replacements of supporting metal parts to make the movement more stable;
- ☑ Much of the microcontroller code has been rewritten to create a crash recovery mechanism, to communicate with the driver of the polarization motor and to create a more robust and accurate RA spherical movement;
- ☑ Delimitation of misalignment error sources.

3.3.2 Antenna Under Test

As stated, the measurements assume that the distance between the antennas remains constant during the measurement. Therefore, misalignment is also a concern in AUT placement. In Figs. 23 and 24, it is possible to note that the system will measure planar and connectorized antennas. For connectorized, only the AUT needs to be moved; for planar, both the AUT and the probe need to be moved. The use of two independent positioners is mandatory. It is important to notice that the contact between planar antennas and the probe is very delicate: the pads are generally designed with a pitch of 100um, and the probe is fragile and expensive.

In the Center’s setup (Fig. 30), it was chosen that the antenna should contact the probe, and not the contrary, as would be expected. The reason is simple: the AUT [support] base is lighter than the probe apparatus. This generates more stability

in this delicate movement. To avoid measurement interference, the AUT base is made of a material that imitates air. In this base, an air duct was opened to allow vacuum suction, in order to keep the antenna stable during contact and measurement. It is fixed in a motorized micropositioner, which is driven by three piezoelectric motors, one for each axis (x,y,z). These devices have a resolution of about 30 nm. For the slightly coarse movement of the probe, a manual micropositioner is used, also with 3 degrees of freedom. For connectorized antennas measurement, only one micropositioner is used: the motorized when in V band setup (Fig. 25), and the manual when in W band (Fig. 26). The two existing positioners are connected to a metallic apparatus which, in turn, is mechanically isolated from the rest of the building, in order to prevent vibrations and damage to the probe.

Figure 30: AUT base and probe positioners.

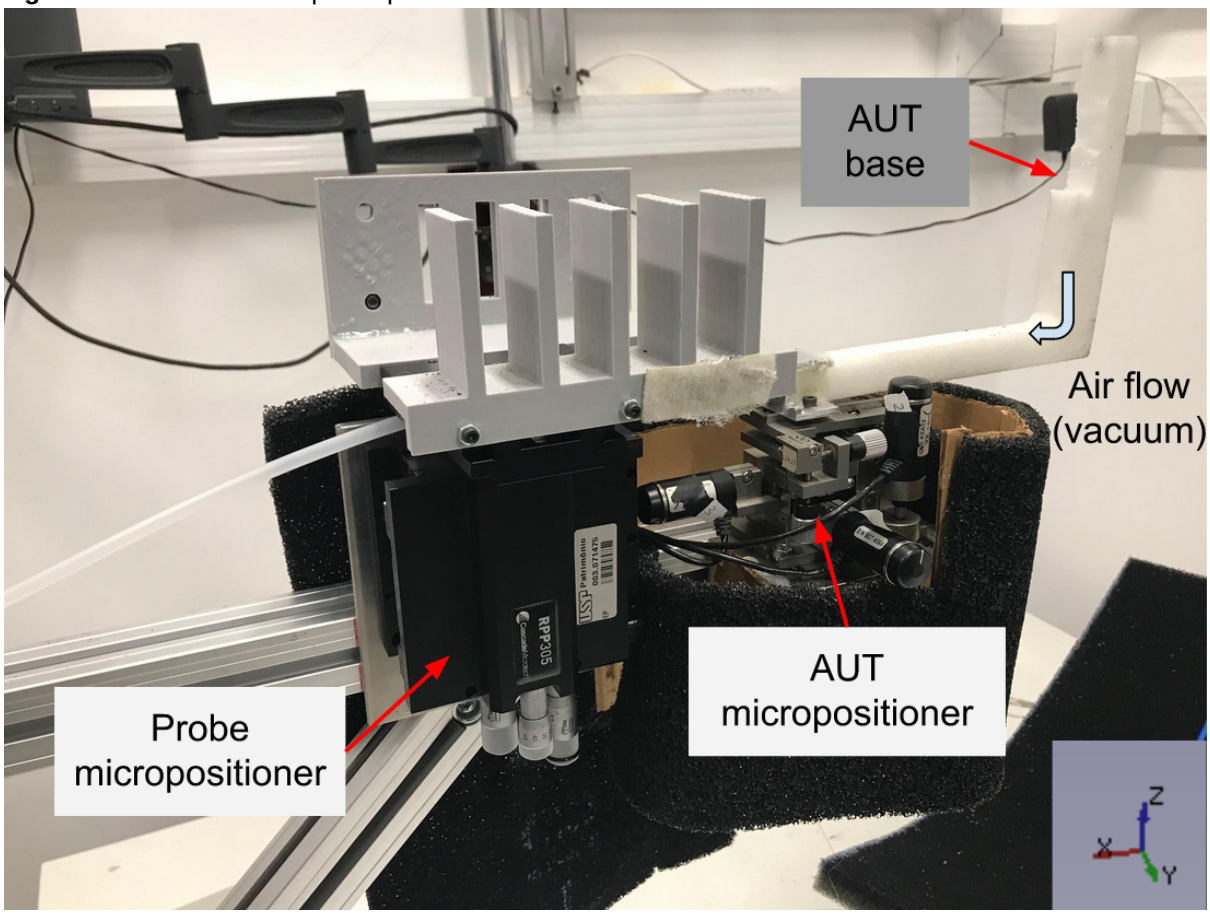

Source: author.

For the V band setup, the probe is directly connected to the VNA through one 1.85mm coaxial cable; for the W band, the probe is connected to a 1mm coaxial cable, which is connected to a coax-waveguide adapter, and then to a WR-10 waveguide which is connected to the Test Port of the frequency extender (Fig. 31).

All this structure is placed above the probe micropositioner. Each band setup has its own custom made probe, with an RVP-style body, made by Picoprobe, quite similar to the setup in section 1.2.3; it is designed to keep metal parts as far away from the AUT as possible. Note that the coaxial contact comes from bottom to top, which is not very common for micro-probes.

Figure 31: Final assembly of the part concerning the AUT.

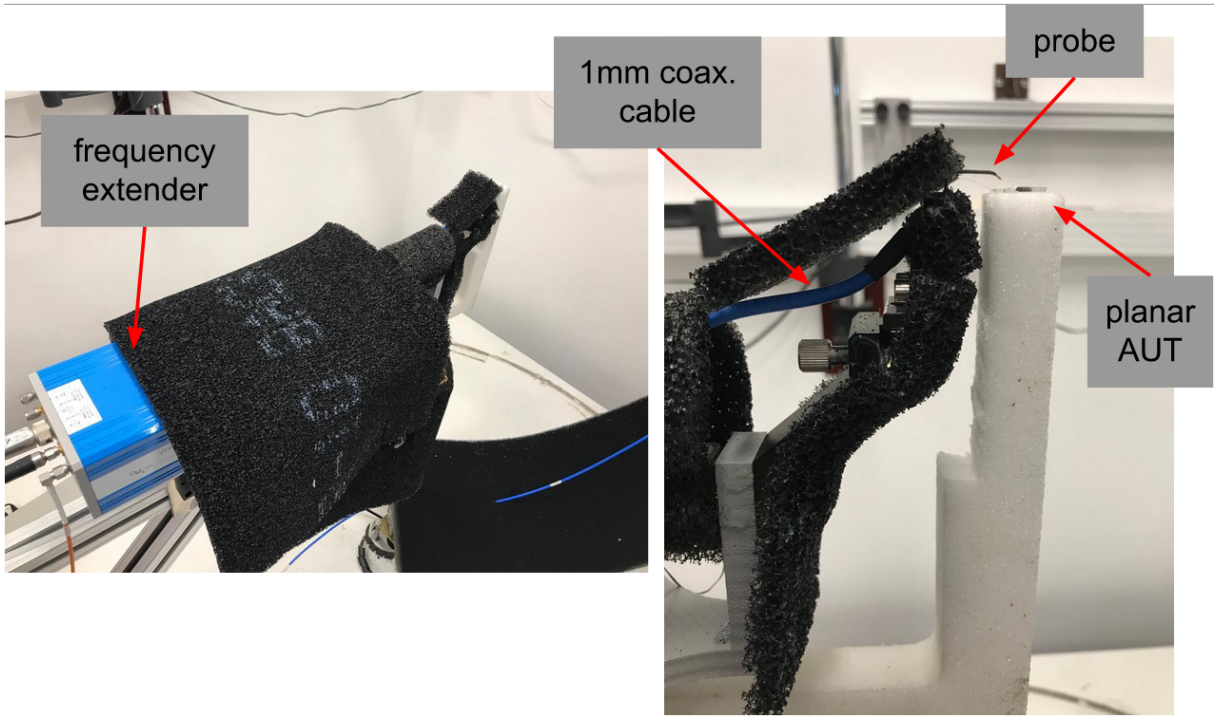

Source: author. The probe is already connected to the frequency extender, and this is resting on the probe positioner. One AUT is above the AUT base. The next step is to move this base to make contact between the tip and the antenna.

At this point, it is well known that it is possible to move the probe and the AUT separately, and for the correctness of the measurement, the AUT must be set at the center of the RACS. Let's suppose, for a while, that there is a visual feedback of where this RACS center is (see Fig 29). Let's call this point (x0,y0,z0). Below, a procedure for aligning the AUT is described; in Fig. 32, this procedure is presented in a flowchart manner.

1) Configure the instrument to show at the front panel the receiver power for the whole band loading the "VNA state file" "X_band_probe_contact.sta". It will be the feedback of the probe contact, ie. the way to distinguish between no contact and contact. At this point, it is possible to see the noise floor, which is down -90 dBm. Turn on the DC power of the multiplier and, for the W band,

the frequency extender power source. Move the RA to the simulated boresight of the AUT. At this point, the receiver shows near -60 dBm: it is the probe acting as a bad antenna;

2) To prevent accidental damage to the probe, move it as far as possible from the AUT base while making manual modifications to it. The AUT base must start this procedure from the lowest height (Z) possible.
3) Put the AUT in the AUT base with the help of a clamp. The user must estimate, in this positioning, if the probe will be able to reach the pads. The antenna pads must be aligned to the probe body;
4) With the manual micropositioner, move the probe until its tips come close to the center of the RACS. Its height must coincide with z0; the Y of the probe must be the same as the y0; the X must take into account the length of the antenna access, ie. the distance between the pads and the center of the AUT. Let's call this distance L'. Then, the X position of the probe tips must be at x0+L'.
5) Align the X and Y coordinates of the base of the AUT to the probe. If the end-of-travel of this positioner is reached, go back to step 2. When X and Y of both are almost aligned, see if the AUT center is at (x0,y0); if not, the user did not estimate very well the access length; go back to step 2.
6) With the help of a microscope, make the contact between the probe and the AUT, moving the AUT base mainly in the Z direction. Again, the feedback will be the front panel view of the equipment. The received power level will increase significantly when contact is made.

Figure 32: Flowchart of the procedure to align the AUT to the center of the RACS.

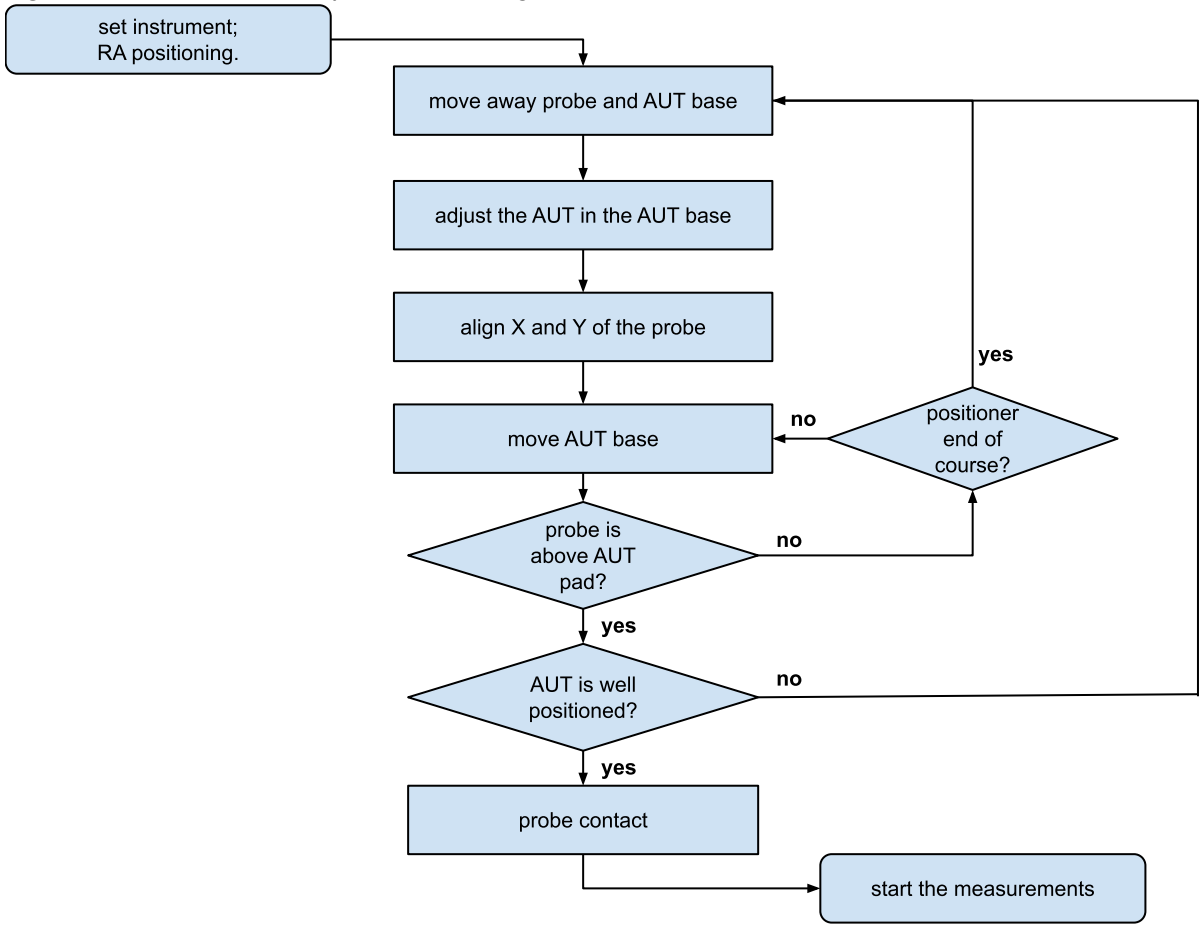

Source: author.

The improvements of this part of the system are shown below:

- ☑ Project and implementation of both the AUT and probe supports, including the metal parts that attach the micropositioners to the aluminum profile (isolated from the building), and the Polylactic Acid (PLA) parts that support the frequency extender and the probe, in addition to the AUT base material cut. The laboratory already had the micropositioners;
- ☑ Probe contact algorithm.

3.3.3 Considerations about coordinate systems

In the previous section, it was shown that the RA movement defines the RACS. It was supposed that somehow the user was able to visualize the center of the RACS. Then, the AUT alignment becomes possible. How to create this visual feedback? The best imagined alternative for non-invasive and accurate marking is

using lasers. Here, two line lasers will be used for the X=0 and Y=0 planes, and a cross-line laser plummet for the Z plane.

A metal structure was designed to allow the *X laser* to move in X and Z directions, and the *Y laser* to move in Y and Z. Such a structure guarantees a 90° angle shift between the two planes. Before aligning those lasers to the RACS, it will be great to align the RACS to an absolute reference: the earth. The procedure is: match the vertical plummet line with the part of the azimuth axis that is in touch with the table (Fig. 27), and modify the height of each one of the table feet individually, in an iterative way. Alignment feedback is given by moving the system in azimuth: the shaft of the elevation motor must remain in the horizontal laser plane. At this point, the Z position of the table is parallel to the earth surface; the Z=0 plane and the normal that contains the center of the RACS is defined.

Figure 33: Laser system giving the visual feedback of the RACS.

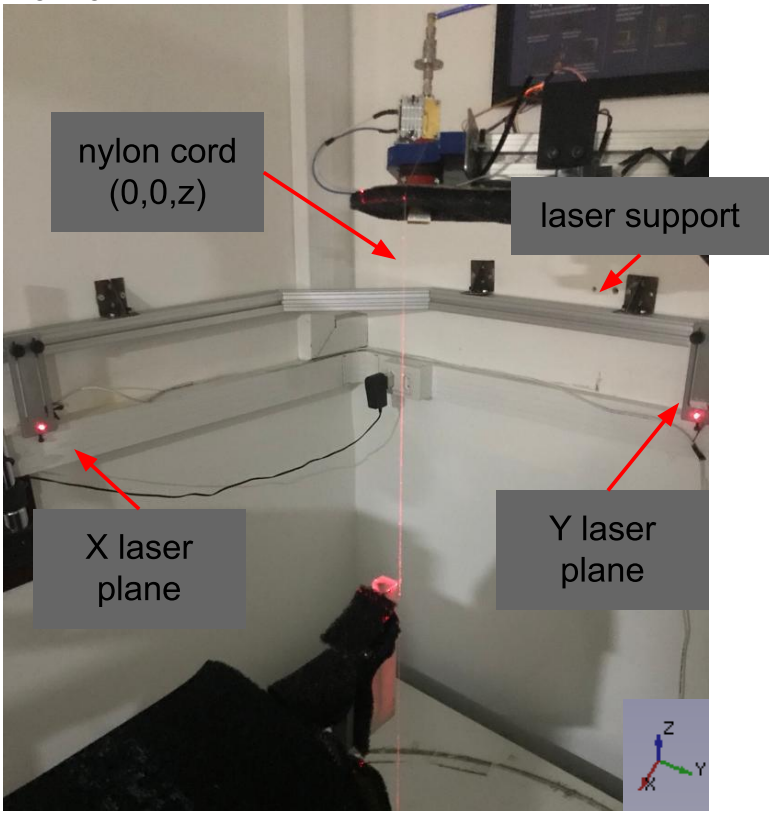

Source: author. Three lasers create this orientation: two line lasers define the x=0 and y=0 planes, and a cross-line laser plummet defines the z=0 plane.

Next step is to align the *X* and *Y lasers*, individually, to the vertical line of the plummet laser. First, a nylon cord (see Fig. 33) is connected to the RA support and to a weight, and is aligned to this vertical plummet laser. This will give visual feedback, as it is not possible to see the laser without a material to reflect the light. Turn off the

plummet laser and align both *X* and *Y lasers* to the nylon cord. Finally, the intersection between those two lasers with the horizontal plummet beam is the center of the RACS.

Notice that, during the alignment process, the relative rotation between AUT and the RACS was modified. The AUT base is probably not parallel to the RA table. Is this disorientation of the system dangerous for the measurements? A basis to discuss these misalignment aspects must be created. Above, it was concluded that the RA movement defines the RACS. The laser system defines another coordinate system; but it could be positioned as close as possible to the RACS, and its sole purpose is to visually show the RACS to the user. It's possible to model the AUT positioning as a relative coordinate system, the *AUTCS*, as shown in Fig. 34. The *xy plane*, for planar antennas, will be the copper or dielectric plane; *xz plane*, or *E-plane*, will be the symmetrical plane containing the access. The *yz plane*, or *H-plane*, will be the intersection between both previous planes and the AUT centroid. The reason for the E and H-planes convention is that, for most linear antennas, these will be respectively their maximum vector field position, ie, the polarization of the AUT (see section 2.2.3).

Figure 34: Defining the AUT coordinate system (AUTCS).

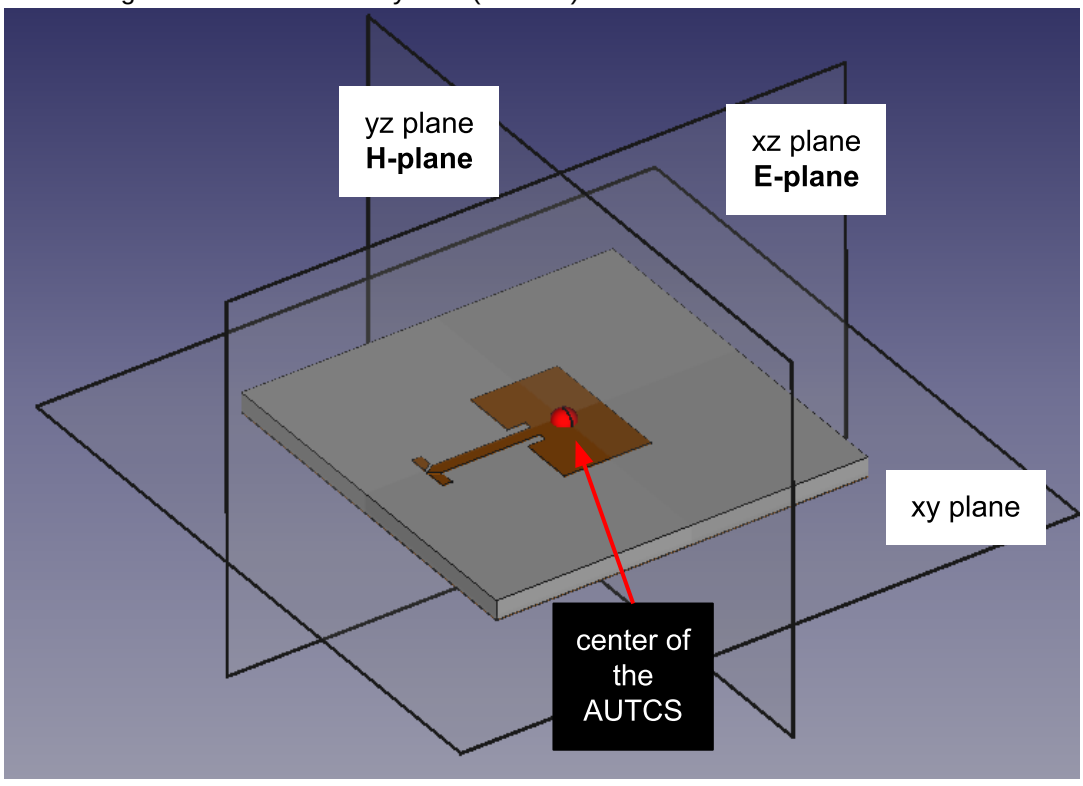

Source: author. The AUTCS is a relative coordinate system of the RACS, which will be our global or absolute coordinate system.

When both coordinate systems coincide with each other, there will be no AUT positioning error. The misalignment between them could be separated between translational and rotational offsets. The first one could be arbitrarily reduced with the help of the micropositioners and laser system, and, therefore, will be assumed null in this work. The reader could find more information about the influence of the translational offset into the measurements at [18]. Then, for us, the misalignment between AUTCS and the RACS is only caused by the rotational offset. This is what distinguishes the AUT figures of merit indexes (φ_r,θ_r) (section 2.2) from the measured ones (φ,θ) (section 2.3). Their relation is given in Eq. 21.

$$\left(\varphi_r, \theta_r\right) = (\varphi + \Delta\varphi, \theta + \Delta\theta) \quad \text{(Eq. 21)}$$

It is easy to imagine that for a 3D radiation pattern, this correction could be made in a pos-measurement stage. For a maximum gain, this rotational offset doesn't disturb the data, as the AUT boresight must be searched independently of its coordinates. In a 2D radiation and polarization pattern, however, it is a good practice to align the azimuth in a way to measure the H and E-planes (Fig. 34). For linear polarized antennas, an algorithm was developed to search for these planes while moving the azimuth motor. Therefore, in this antenna measurement system, once the RACS is well defined, the AUT positioning misalignment can be reduced to an arbitrarily low value.

The improvements of this part of the system are shown below:

- ☑ Project and implementation of the laser system;
- ☑ Theoretical study of misalignments: delimitation of error sources, modeling of the setup as a set of coordinate systems, explanation of important misalignments for each of the measurements of the antenna's figures of merit.

3.4 Control Software

The control software is responsible for the orchestration between the instrument and the microcontroller. Through its intuitive interface that has been evolving in these three years of work, the user is able to easily express his measurement needs. One example of its simplicity is shown in Fig. 35, where the user can see the exact sampling points that he settled for a 3D radiation pattern.

In its main window, the user can start and stop the sweeps, save, open and manipulate the data of the various measurements discussed in this work. For radiation and polarization patterns, the system can measure up to 10 frequencies in one single RA movement. It has the capability to automatically find the maximum polarization coupling position, as well as the E and H-planes for linear polarized antennas. Measurement settings are done in a pop-up window to create a less dense interface; all the system positioning and calibrations are performed through this user interface, and many indicators are implemented for a complete understanding of system status. The data is exported in a text file and shows all pertinent measurement information such as RA position, maximum received power, VNA settings, calibration antenna and last calibration date (in gain measurements).

Figure 35: Pop-up configuration window of the control software; behind it, it's possible to see the main window, responsible for the data acquisition and manipulation.

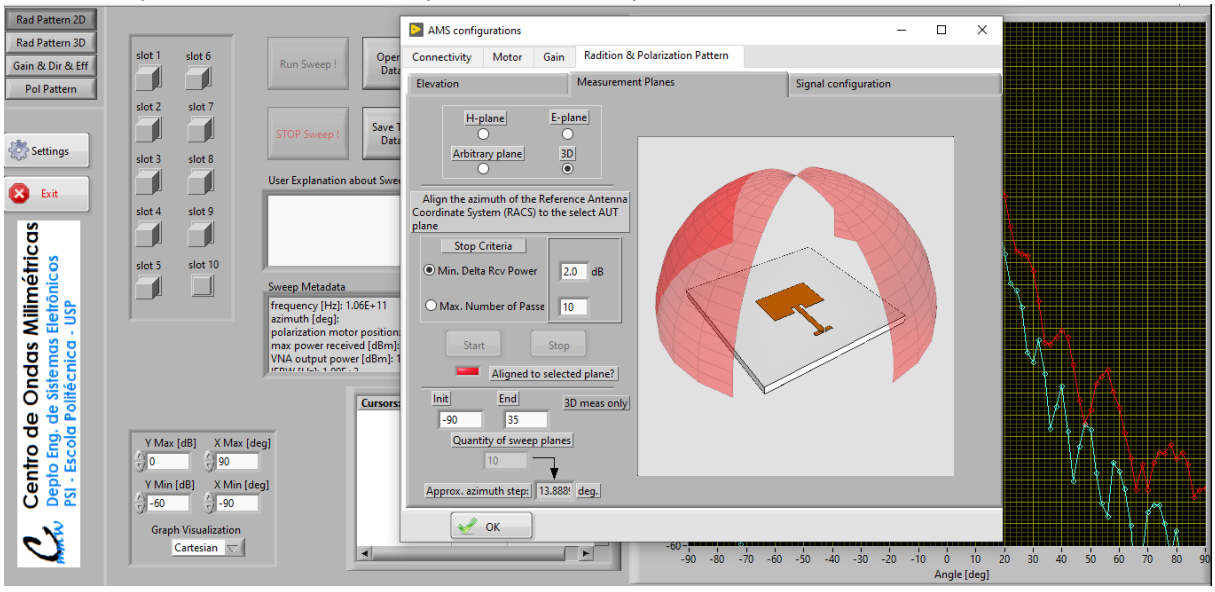

Source: author.

Appendix B shows a sequence of images of the user interface of this software. Some control buttons are automatically disabled if the communication with the instrument and/or microcontroller are not established. The measured data were retrieved from previous made measurements. This section will not have the "improvements" checkbox, as all the software and algorithm implementation were all made during this work period.

4 Results

4.1 Overview

After establishing some assumptions in Chapter 2, the antenna measurement system presented in Chapter 3 was developed. While presenting it, some possible sources of errors that could affect the accuracy of the measurements were pointed out. The first part of this section is dedicated to studying these system assumptions and estimating their errors:

1) The response variation is only made by the device under test (DUT). For example, the difference in the measurements of two different points in the radiation pattern must be caused by the AUT response to the incoming wave, instead of an increased output power of the multiplier, or increased noise levels on the VNA receptor. This will be discussed at the instrumentation accuracy section (4.2.1), where all the active devices into the chain are taken into consideration.
2) The system is measuring exactly the point that it is supposed to be. What is the error associated with the motion of the RA? For that, section 4.2.2 will test the repeatability of the motor movement.
3) The RA must make a spherical trajectory around the AUT. The errors caused by the misalignment of the RA apparatus (Fig. 29) undermine the assumption of the existence of the RACS. This misalignment error will be studied in section 4.2.3.

The first two errors are non-deterministic in nature and therefore must be presented through a statistical approach. Both will be modeled as Gaussian processes, and the final accuracy will be presented as the three-sigma rule of thumb [33], in which 99.7% of the events lie within this interval. Each section will describe its own test setup, conditions and sequences. All the tests were done using a horn antenna as the AUT, after a 40-minute instrumentation warm-up, with the VNA configured to emit a 14.5 dBm signal and receive it with a 1 kHz IFBW. The V band configuration was used for the study. But the same methodology could be used with the W band setup.

After the accuracy of the system is presented in section 4.2, some real world antenna measurements will be shown and discussed in section 4.3. The conclusion and directions for future work will be in chapter 5.

4.2 Accuracy

4.2.1 Instrumentation

It is well known that electronic instruments drift with time. The main reason is its temperature variation. This is particularly a problem in active devices, which dissipates a lot of power to process the signal. In this setup, during the test period, the frequency multiplier consumes 8 V x 0.5 A = 4 W of power, and the frequency extender consumes 12 V x 0.8 A = 9.6 W. All the energy that is not spread to the next stage of the chain, in an electromagnetic format, is dissipated into heat. This phenomena elevates the temperature of the devices, even putting the characterization system into a small room with air conditioning.

Figure 36: Example of instrumentation error caused by the rise of the temperature.

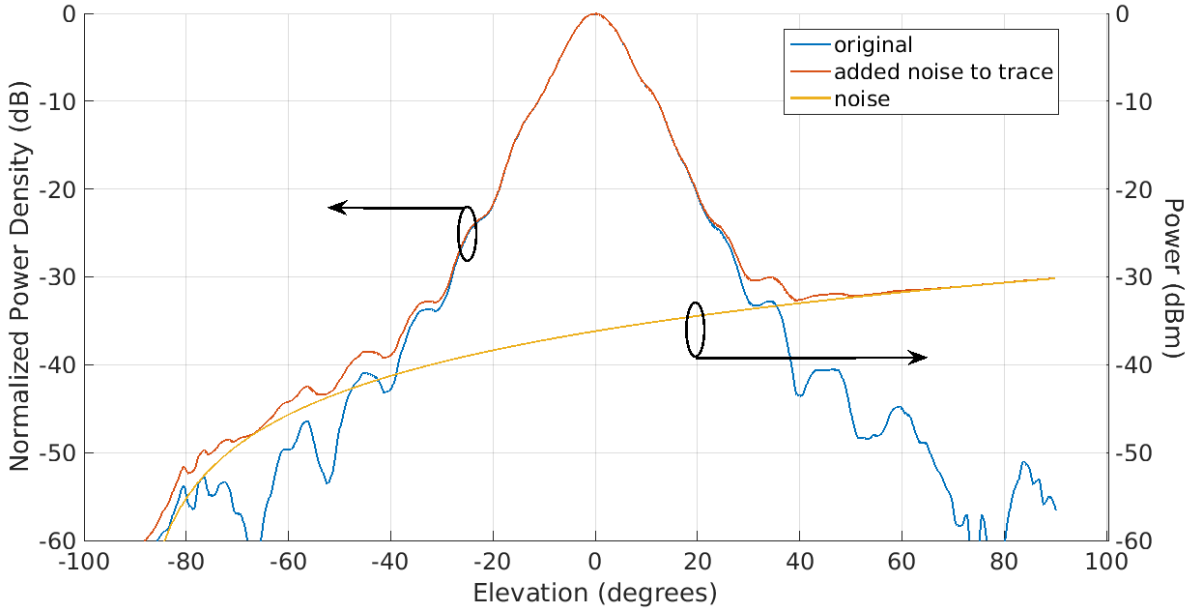

Source: author. The yellow trace represents the power of a hypothetical noise. Adding this noise signal to the original radiation pattern results in the red trace. Notice that the noise masks the real radiation pattern data.

In Fig. 36 there is an example of what this kind of error could cause to the measurements. Let's suppose that the temperature rising in the VNA receiver increases the power density of the noise as a cubic function, as the time goes on. The yellow trace shows this noise power; the red one is the result of the sum of the

measured radiation pattern with this VNA receiver drift. Notice that this error masks the real AUT data, as the result is always above the noise floor.

The instrumentation accuracy test consists of analyzing the stability of the measurements for various frequencies and received power levels. Here, three frequencies (50 GHz, 60 GHz and 70 GHz) and three different RA positions (here called A, B and C), which is equivalent to varying the received power, were tested. The tests A and C lasted 6 hours, while the B lasted 5 hours, which are reasonable times for a 3D radiation pattern measurement. At every one-minute interval, 20 samples are acquired, and the average value is stored in memory. The results are presented at Fig. 37.

Figure 37: Instrumentation test curves.

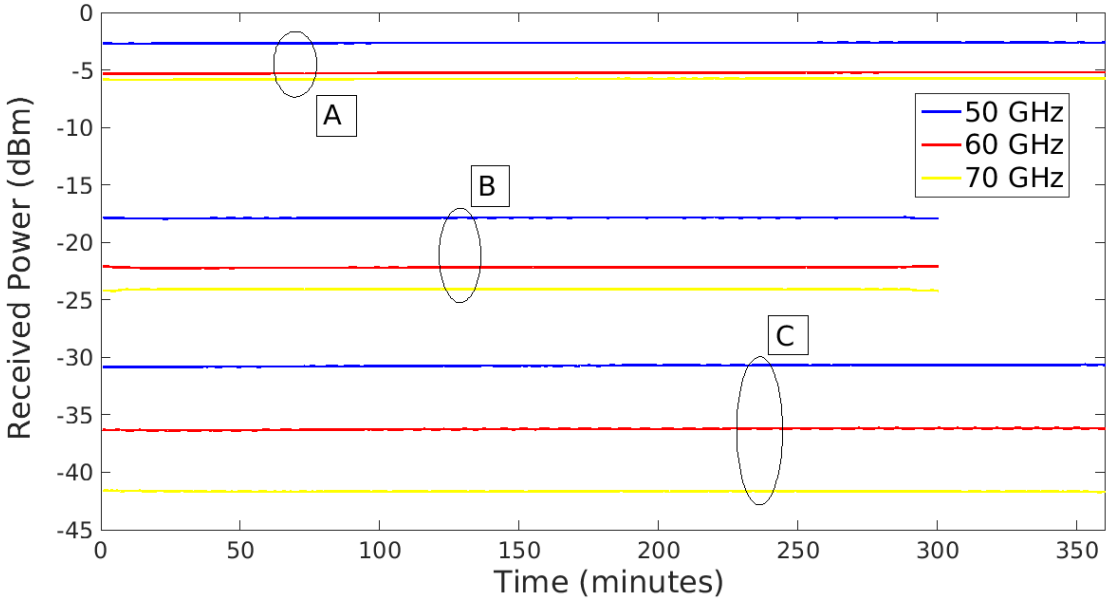

Source: author. Chart showing the evolution of the values at the VNA receiver during the tests for three frequencies (50 GHz, 60 GHz and 70 GHz), in three different RA positions (A, B and C).

To understand the behavior of the signal, at Fig. 38 the traces of the 50 GHz signals are enlarged. It is possible to see that it is not a true stationary process, as the mean level increases as the time elapses.

Figure 38: Zoom at the three 50 GHz test traces of Instrumentation Test (Fig. 37).

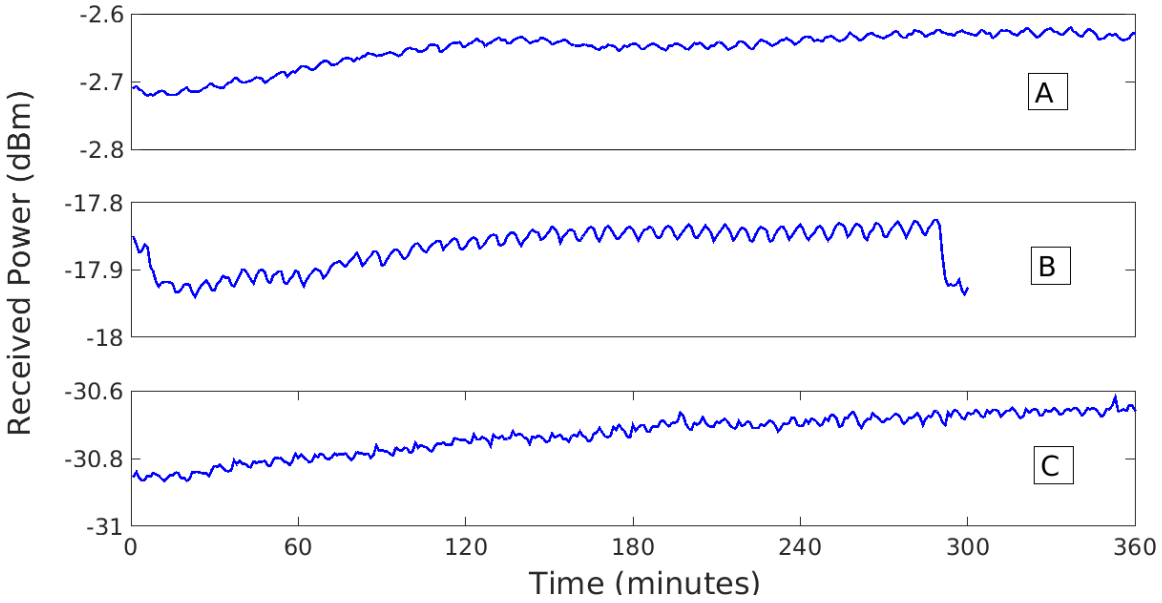

Source: author. It's possible to see that the mean level increases as time goes by. It is not possible to know what happened to the signal at position B to make it change so quickly at the beginning and end of the test.

Table 2 - Variance of the decibels-milliwatts values of the tests of Fig. 37.

	50 GHz	**60 GHz**	**70 GHz**
Point A	$7.1 \cdot 10^{-4}$	$1.6 \cdot 10^{-3}$	$1.1 \cdot 10^{-3}$
Point B	$9.8 \cdot 10^{-4}$	$1.2 \cdot 10^{-3}$	$8.6 \cdot 10^{-4}$
Point C	$3.7 \cdot 10^{-3}$	$3.8 \cdot 10^{-3}$	$4.5 \cdot 10^{-4}$

Source: author.

Table 3 - Variance of the milliwatts values of the tests of Fig. 37.

	50 GHz	**60 GHz**	**70 GHz**
Point A	$1.1 \cdot 10^{-5}$	$7.4 \cdot 10^{-6}$	$3.9 \cdot 10^{-6}$
Point B	$1.4 \cdot 10^{-8}$	$2.4 \cdot 10^{-9}$	$6.9 \cdot 10^{-10}$
Point C	$1.4 \cdot 10^{-10}$	$1.1 \cdot 10^{-11}$	$1.1 \cdot 10^{-13}$

Source: author.

Using the extracted data, the variance of the values in decibels-milliwatts were calculated. However, as this noise is added to the original signal that is coming from the RA, all these statistics must be done in milliwatts instead of decibels. Table 3 shows this variance in milliwatts. Looking only at the magnitude order of the values,

it is possible to notice that the instrument deviation over time of the setup increases as the received power level increases (value of point A is greater than point C) and as the frequency decreases (value for 50 GHz is greater than value for 70 GHz).

To better visualize what this error causes to the measurements, the statistical excursion of the received signal (3 sigma) is presented in Table 4. For every test point, the difference is not greater than 0.2 dB.

Table 4 - Three-sigma excursion, in decibels-milliwatts for each point of Fig. 37.

	50 GHz	**60 GHz**	**70 GHz**
Point A	0.080	0.119	0.097
Point B	0.094	0.105	0.087
Point C	0.182	0.185	0.064

Source: author.

At this point, it is possible to conclude that the instrumentation accuracy is a function of the measurement time, the test frequency and the receiver power level. Table 3 and 4 gives these values for a 5-6 hours measurement, for three frequencies at three received power levels. Using the same methodology adopted in these tests, it's possible to characterize the instrumentation accuracy in any desired frequency and received power level, for a given test period.

Figure 39: Example of radiation pattern measurement error caused by a stochastic error in the elevation stepper motor.

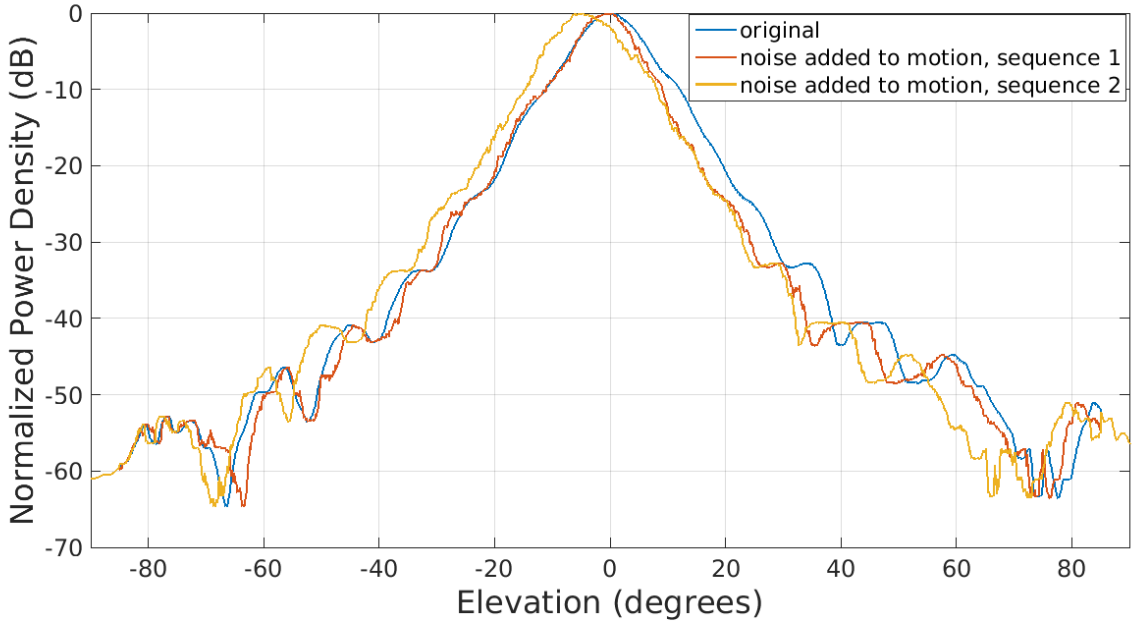

Source: author. This chart shows the effect of a noisy elevation movement in the measurement of a radiation pattern of a high directive antenna, very well aligned to the RACS.

4.2.2 Mechanical Movement

This essay aims to discover what is the movement accuracy of the elevation movement, in degrees. First, let's see what this kind of error could cause to the measurements. Fig. 39 shows a radiation pattern measurement trace, which is for a Horn antenna measurement, well rotationally aligned (boresight is near 0° elevation), and two traces that simulate two outcomes of the addition of noise to the motion. This movement error is cumulative, the step has a Gaussian distribution with mean equal to +0.1° and standard deviation of 1.55°. It could be seen that in this exaggerated scenario, the trace becomes asymmetrical, and the boresight leaves its original position.

For this test, 10 radiation patterns were measured, from -90° to +90° in elevation, using the same AUT, in the same AUT position and orientation, at the same three frequencies of the previous section tests. The tests were made in sequence. The results for the 60 GHz essay are given in Fig. 40. The AUT is purposely not rotational aligned, and that is the reason for the actual asymmetry and boresight dislocation.

As this test pretends to extract the movement accuracy from instrumentation measurements, and as these sources of error are uncorrelated, it is necessary to subtract the previously found variance (instrumentation error) from this section measurements. This way, let's focus on the points 'A', 'B' and 'C' from the Fig. 40, as the instrumentation variance for these points are already known (Table 3). For each of these points, in each of the tested frequencies, it is possible to calculate a variance for the 10 values (essays) of received power. Table 5 and 6 shows these values in decibels-milliwatts and milliwatts, respectively.

Figure 40: Mechanical movement test.

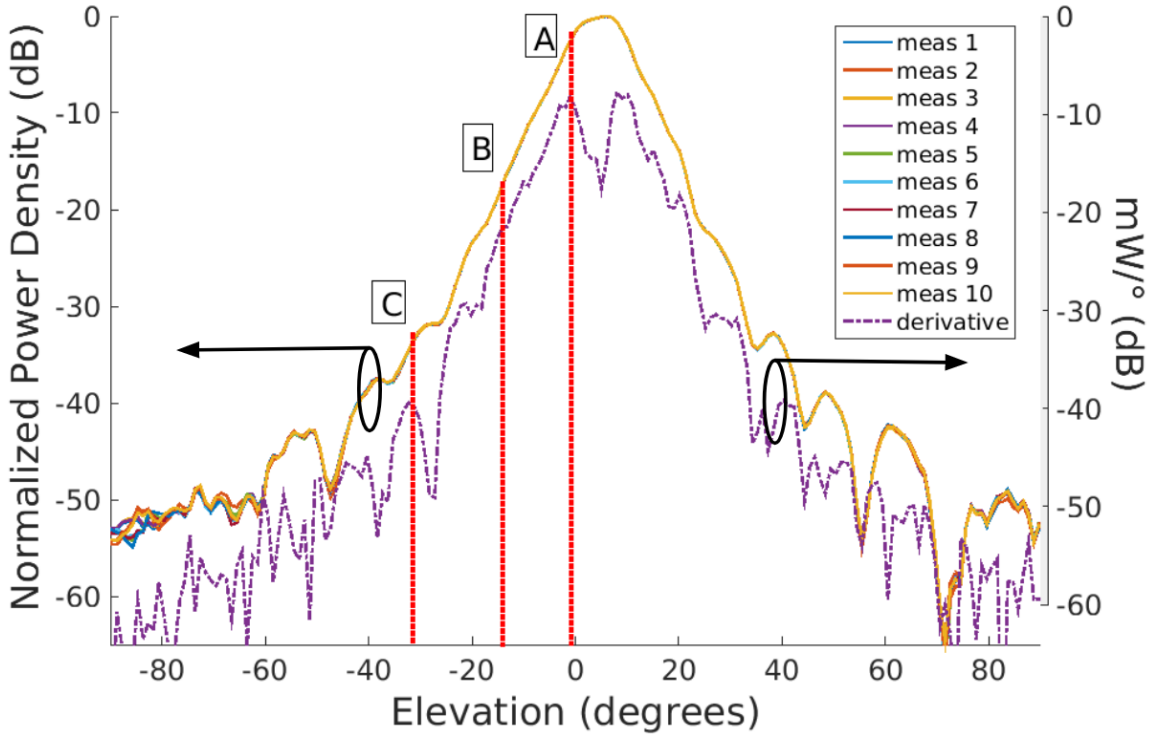

Source: author. Essay showing 10 measurements of a radiation pattern for the 60 GHz signal. The differences between the traces could only be caused by the instrumentation and movement errors. The points ‘A’, ’B’ and ‘C’ are those in which the information of instrumentation accuracy is already known.

Table 5 - Variance of the decibels-milliwatts values of the mechanical movement accuracy tests.

	50 GHz	**60 GHz**	**70 GHz**
Point A	$5.1 \cdot 10^{-5}$	$5.5 \cdot 10^{-4}$	$8.4 \cdot 10^{-5}$
Point B	$3.3 \cdot 10^{-4}$	$7.7 \cdot 10^{-4}$	$9.3 \cdot 10^{-5}$
Point C	$3.4 \cdot 10^{-3}$	$2.0 \cdot 10^{-3}$	$1.4 \cdot 10^{-2}$

Source: author.

Table 6 - Variance of the milliwatts values of the mechanical movement accuracy tests.

	50 GHz	**60 GHz**	**70 GHz**
Point A	$1.9 \cdot 10^{-6}$	$2.3 \cdot 10^{-5}$	$3.4 \cdot 10^{-6}$
Point B	$1.1 \cdot 10^{-8}$	$1.3 \cdot 10^{-8}$	$6.2 \cdot 10^{-10}$
Point C	$1.2 \cdot 10^{-11}$	$1.3 \cdot 10^{-11}$	$2.3 \cdot 10^{-11}$

Source: author.

Subtracting Table 3 values from Table 6 corresponds to disregarding the instrumentation error of the mechanical accuracy tests. The results are shown in table 7.

Table 7 - Calculated variance for the mechanical movement of the antenna measurement system.

	50 GHz	**60 GHz**	**70 GHz**
Point A	$-9.1 \cdot 10^{-6}$	$1.5 \cdot 10^{-5}$	$-4.9 \cdot 10^{-7}$
Point B	$-3.0 \cdot 10^{-9}$	$1.1 \cdot 10^{-8}$	$-6.5 \cdot 10^{-11}$
Point C	$-1.3 \cdot 10^{-10}$	$1.8 \cdot 10^{-12}$	$2.3 \cdot 10^{-11}$

Source: author.

The existence of positive (white and orange cells) and negative (gray cells) values in a balanced way suggests a similarity between the mechanical movement test variance and the instrumentation test variance. This means that the instrumentation variance is dominant over the movement variance. Analyzing the highest positive value (orange cell), i.e. the worst case of stepping error, and applying the three-sigma rule, shows that the measurement error caused by the motor movementation is +-0.0118 mW, and occurs at the ‘A’ position of Fig. 40. To turn this power measurement error into step error, it is mandatory to use the derivative of the radiation pattern (in milliwatts) as a function of the elevation angle, calculated at this ‘A’. In Fig. 40, using one of the measurements for the 60 GHz test, this numerical derivative is calculated and plotted in decibels. The value of the derivative in this ‘A’ elevation position is 0.0717 mW/degree. This means that in this setup using this AUT, 1 degree of error corresponds to 0.0717 mW, and 0.0118 mW of error would correspond to a **0.1646 degree** step error. This is the three-sigma, worst case, maximum angular movement error of this setup.

Finally, it was shown that the instrumentation error is predominant over the movement error. As such AUT is probably the most directional antenna that this system will measure, it is totally safe to disregard the system movement errors when considering the instrumentation error.

4.2.3 Reference Antenna Alignment

It is important to notice that the 0° elevation position is not initially known. Our visual estimation error is not small. The end-of-travel switch is installed, but it will

never be exactly at this position. Tests need to be performed to understand the quantity of steps necessary to go from this sensor to the origin.

Figure 41: RACS elevation zeroing system procedure.

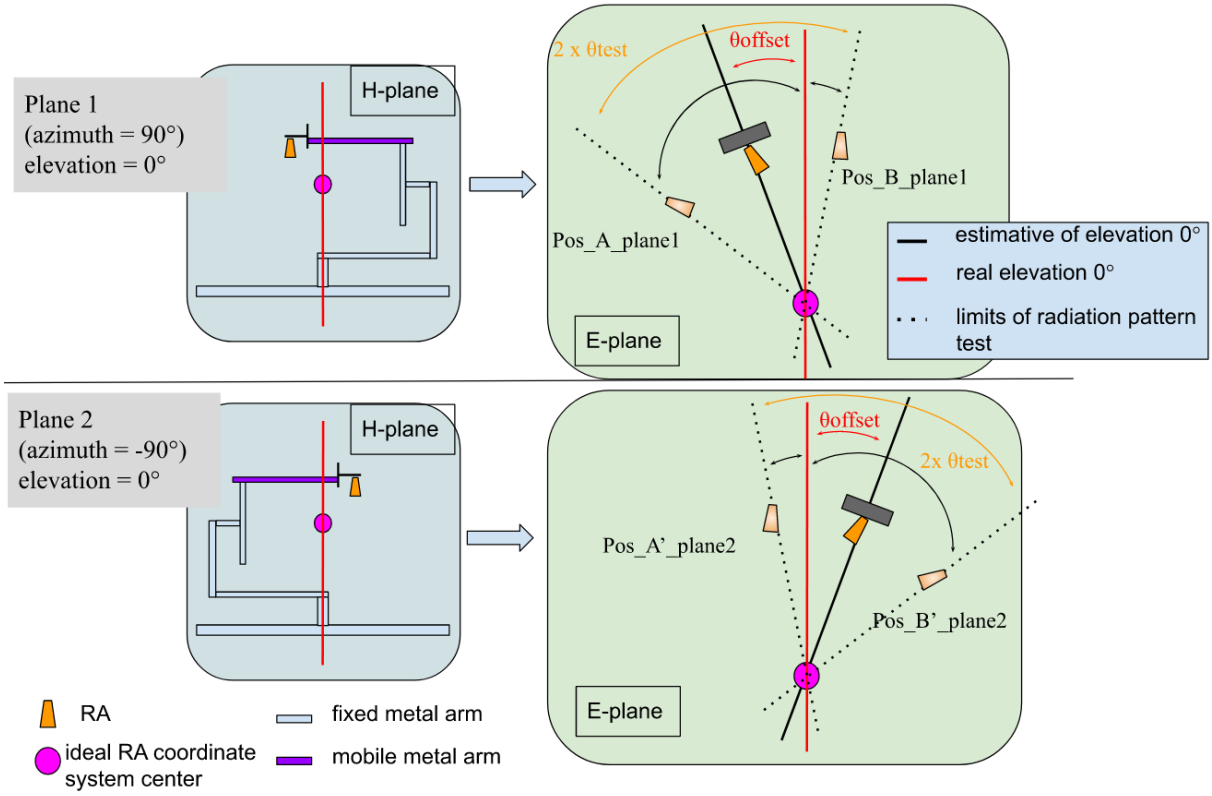

Source: author. These two radiation pattern measurements of the same plane are used to discover the 0° elevation position of the system.

A way to align this coordinate is to make two radiation pattern measurements of the same plane, using two different azimuth positions: -90° and +90°. The AUT should be a very directional antenna; this way, the system will have a very abrupt coupling power variation for a very narrow elevation displacement (see the derivative of Fig. 40). Let's study a theoretical case to understand what to expect from the results. Suppose that the radiation pattern is measured in a 10° range, ie. from -5° to 5°. Suppose that the offset between the estimated zero and the RACS zero is θ_{offset}=3°. Fig. 41 shows this scenario. If θ_{offset} is null, *Pos_A_plane1* and *Pos_A'_plane2* must match, as well as *Pos_B_plane1* and *Pos_B'_plane2*. Instead, as shown in the expressions below, they will be shifted by 6°, which is $2*\theta_{offset}$. The common data of both measurements are the measured points between *Pos_A'_plane2* and *Pos_B_plane1*; in this case, between -2° and 2°.

$$Pos\_A\_plane1 = -\theta_{offset} - \theta_{test} = -5°-3° = -8°.$$

$$Pos\_A'\_plane2 = -\theta_{test} + \theta_{offset} = -5°+3° = -2°.$$

$$Pos\_B\_plane1 = \theta_{test} - \theta_{offset} = 5°-3° = 2°.$$

$$Pos\_B'\_plane2 = \theta_{test} + \theta_{offset} = 5°+3° = 8°.$$

Now, let's make this test with real data. Using the same setup of the previous section, with a 60 GHz signal, both planes were swept, from -3.96° to 3.96° elevation, using a 0.198° step wide. Fig. 42(a) shows these measurements. Datatips are used to show the maximum received value for both traces: they are 8 steps, or 1.386°, apart. Dividing this value by 2 gives 0.693°, which is the distance between the previously estimated zero and the real zero, ie. the θ_{offset} . With this information, the distance between end-of-travel switch and the real 0° elevation could be implemented in the control software. Fig. 42(b) graph is a software correction of this offset.

Figure 42: RACS elevation zeroing test, using the V band horn at 60 GHz.

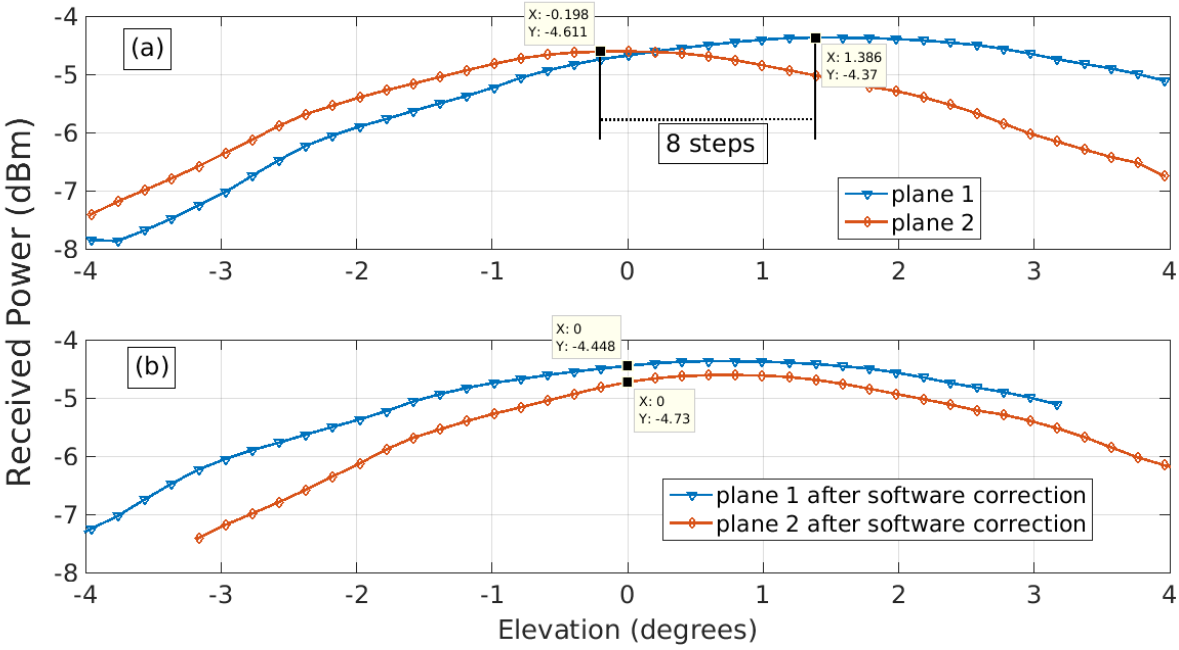

Source: author.

As the measurements of the two planes are done in a short time lapse, it's not believed that the instrumentation inaccuracy is responsible for the amplitude difference between the traces of Fig. 42(b). Contrary to the inaccuracies results presented in the previous sections, this result is caused by deterministic factors, including:

- Misalignment of the RA (section 3.3.1): the error is caused by the described sources of misalignment *RA_d1* and *RA_d2* of Fig. 29.

- Signal reflection: the environment change caused by the variation of the azimuth position (+90° and -90°) could cause differences in the distribution of the reflected signals.
- Rotary joints scattering parameters change: for every RA position, there is a different combination between the positions of the 3 rotary joints.

The last two factors are assumed here to have little influence on the measurements. For the scattering parameters problem, its variation is probably disregarded by the automatic control loop (ALC) of the frequency multiplier; for the reflection problem, absorbers could be placed surrounding all the setup, but some tests not cataloged here indicate very little difference between measures using or not using absorbers around the system.

Therefore, it is assumed that the RA misalignment is the major contributor to the error presented, ie. the difference in traces of Fig. 42(b). This misalignment will be studied in the rest of this section. Fig. 43 shows the same test of Fig. 42, after the elevation zeroing procedure, for a longer elevation interval. It could be seen that the error varies with the elevation angle, which suggests that it depends on the radiation pattern characteristics of the AUT. To give an order of magnitude estimate of this deviation, the biggest difference between the traces is approximately 0.8 dB and happens close to -13° of elevation at Fig. 43.

Figure 43: Two E-planes measurement of the V band horn antenna at 60 GHz.

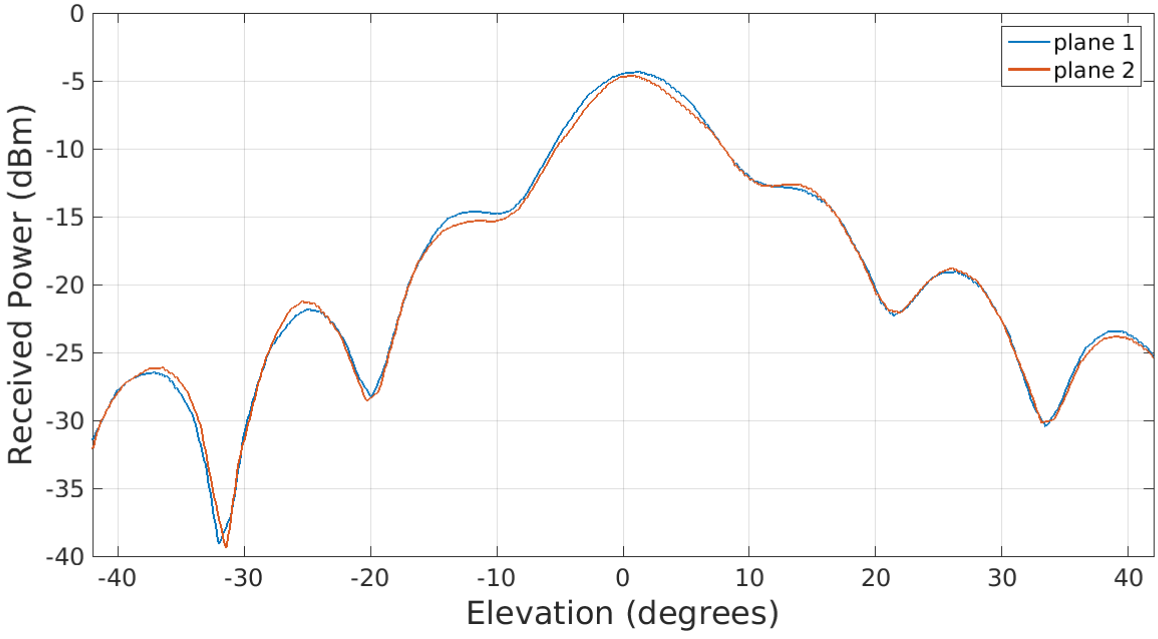

Source: author.

Figure 44: RACS misalignment influence on radiation pattern measurement.

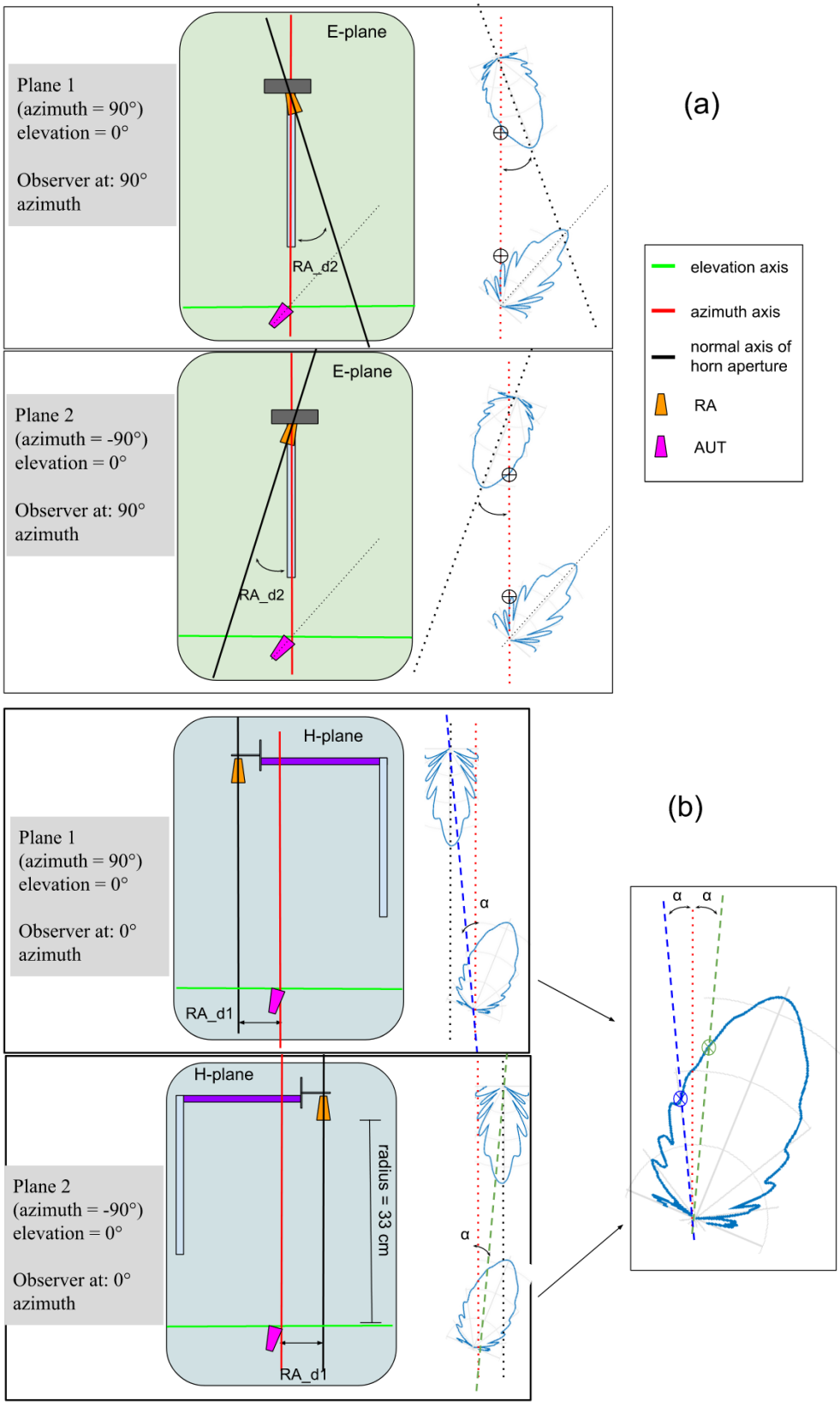

Source: author.

In Fig. 44, there is a graphical representation of the interaction of the radiation patterns of the RA and AUT for the test discussed above, ie. with the azimuth motor positioned in two different positions but with the RA contained in the same plane. In Fig. 44(a), it is considered the *RA_d2* misalignment source, which is a rotational misalignment of the RA; in Fig. 44(b), the *RA_d1* is considered, which is a translational misalignment of the RA. In both cases, it is only considered the influence of the misalignment at the 0° elevation position.

Due to the symmetry of the RA, it is possible to notice that the *RA_d2* does not influence the measurements: for both planes, the shorter line that connects the antennas intersect the same point of both radiation pattern graphs, meaning the same coupling between antennas. However, the *RA_d1* misalignment causes this shorter line to intersect different points of the AUT radiation pattern. This means that neighboring points of the desired AUT pattern point are scanned. In fact, this is also true for points other than 0°: there will always be this *α* difference between the desired point and the actually measured point. First, let's figure out the *RA_d1* distance, and then let's discuss the procedure to accommodate misalignment errors in radiation diagram measurements.

To estimate this *RA_d1*, it is first necessary to calculate *α* based on the difference of power measurement (in milliwatts) of the traces for 0° elevation presented in Fig. 42(b) and a estimative of the derivative of the H-plane radiation pattern at this same point. The H-plane is used because the *RA_d1* misalignment occurs in this plane (see Fig. 44(b)). The derivative of the H-plane at 0° elevation, obtained from the data of graph of Fig. 40, is 0.06483 mW/degree. The formula to calculate the angular deviation α is given below:

$$diff_{H\text{-}Plane}(0°\ elevation) \approx \frac{|\ value\_trace1 - value\_trace2\ |}{2 \cdot \alpha} \Rightarrow$$

$$\Rightarrow \alpha \approx \frac{10^{\frac{-4.44}{10}} - 10^{\frac{-4.73}{10}}}{2 \cdot 6{,}48 \cdot 10^{-2}} \Rightarrow \alpha \approx 0.2°$$

Considering that the RA trajectory sphere has 33 cm of radius and using trigonometry:

$$tan\,\alpha = \frac{RA\_d1}{radius} \Rightarrow RA\_d1 \approx 1\,mm$$

This result is consistent with the order of magnitude accuracy of manually positioning the movable metal arm (Fig. 29). Now, let’s see what this misalignment

error could cause in the measurements. As explained, this *α* variation will be present at all sampling points in the 3D radiation pattern measurements. In Fig. 45, the constant azimuth trajectory of the RA (solid black line) is plotted over a spherical coordinate system. It is shown that the *α* variation is contained only at the elevation trajectory when the pole is being measured, and is contained only at the azimuth trajectory when the equator is being measured. For every other sampling point, *α* variation is a combination of steps in azimuth and elevation.

Figure 45: RA_d1 misalignment error estimation in 3D radiation patterns.

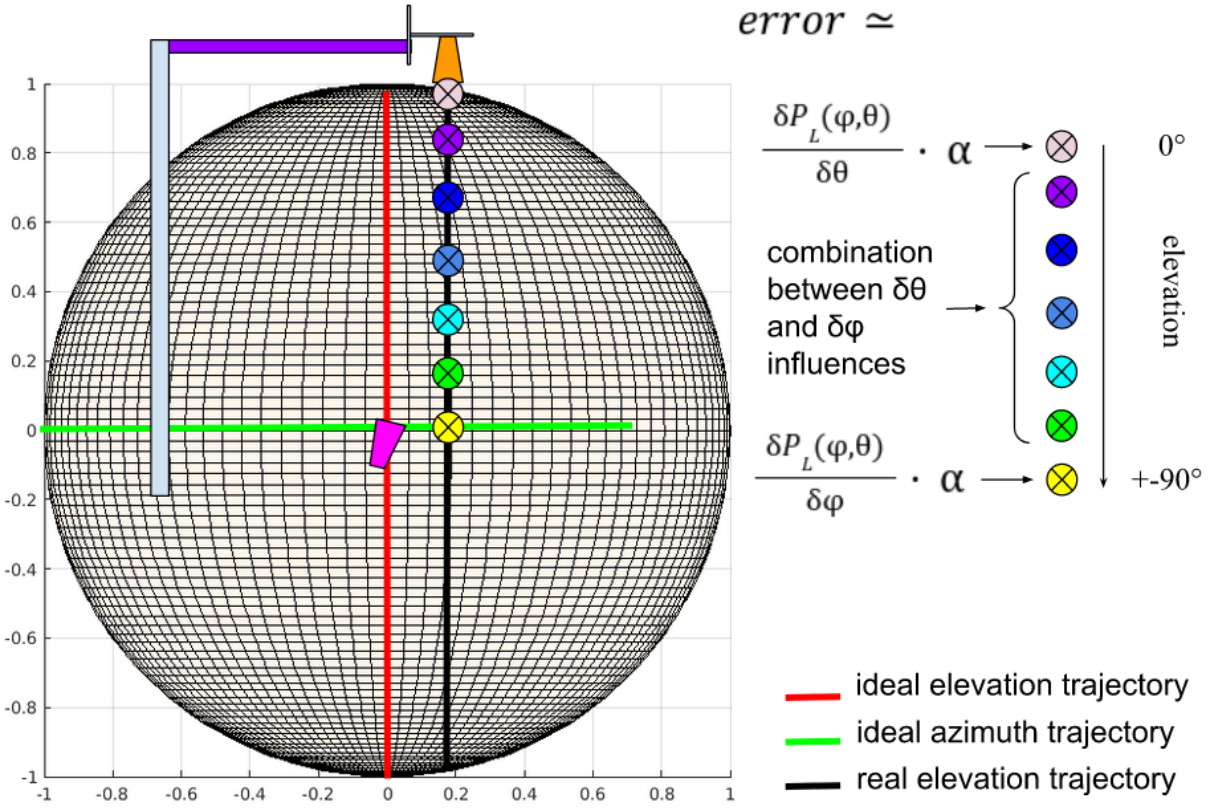

Source: author.

Thus, the influence of this misalignment will depend on a weighting of the elevation and azimuth derivatives of this radiation pattern. The idea here is not to reach an absolute error value for each point, but calculate a range that contains this error. The reason is that it will not be possible to give an absolute error value, as the derivative of the 3D radiation pattern as a function of elevation and azimuth angles are in fact approximations. This way, this work proposes that, for each position, the influence of both components of the magnitude of the gradient be summed to the measured value. The proposed formula is given in Eq. 22, where Δ is used instead of δ to make evident the numerical approximation, and the index “q” is used to

reference an arbitrary measured point.

$$RACS\ Error(\varphi_q,\ \theta_q) = \pm\left(\left|\frac{\Delta P_L(\varphi_q, \theta_q)}{\Delta\theta}\right| + \left|\frac{\Delta P_L(\varphi_q, \theta_q)}{\Delta\varphi}\right|\right)\cdot \alpha \qquad \text{(Eq. 22)}$$

To give an example, in Fig. 46 the level curves of a 3D radiation pattern of the antenna that will be shown in section 4.3.2 is plotted, as well as the gradient vectors (red arrow) . At (φ, θ)=(42°,5°), the gradient is equal to ($3.9 \cdot 10^{-5}$, $2.1 \cdot 10^{-5}$) mW/°, and the received power is equal to $2.6 \cdot 10^{-3}$ mW (-25.86 dBm). Using the found α = 0.2°, Eq. 22 gives an error of $\pm\ 1.2 \cdot 10^{-5}$ mW. Using this equation, the real value of this point is inside the range of [-25.84,-25.88] dBm. Obviously, this range depends on the directivity of the antenna, as well as the measured point.

Figure 46: plot of a measured 3D radiation pattern and arrows representing the intensity and direction of the gradient.

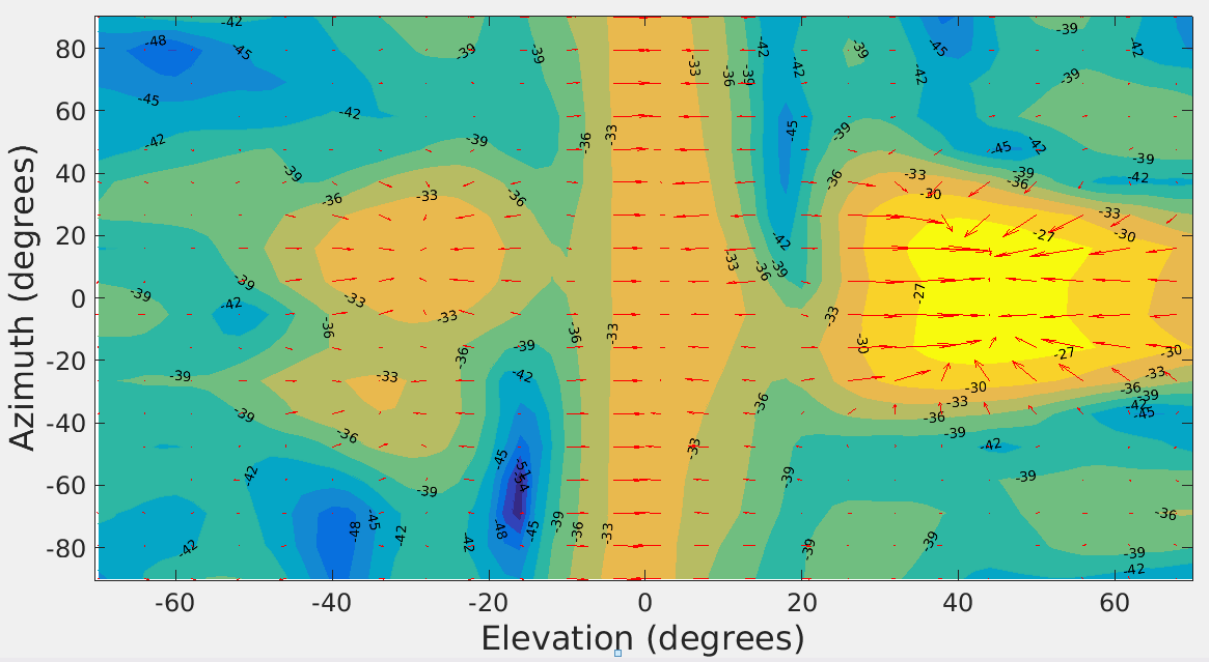

Source: author.

Therefore, the *RACS* misalignment is a combination of the *RA_d1* and *RA_d2* sources of error. No evidence was found that the *RA_d2* misalignment influences the measurements. However, *RA_d1* causes the system to measure a different position of the AUT radiation pattern than expected. To account for the error generated by *RA_d1*, it is necessary to find the angular deviation α, and by estimating the gradient of the AUT radiation pattern it is possible to estimate the error associated with each point of the measured radiation pattern.

4.2.4 Probe effects

As commented, probes are the least invasive way to test antennas in Millimeter Waves. However, their size, material and proximity to the antennas are still a problem, as they cause reflections that generate disturbances in measurements of radiation characteristics. These effects, however, are very difficult to calculate quantitatively [34]. The antenna characterization system presented in this work uses a long body probe together with absorbers to reduce its influence in the measurements.

Accordingly to [35], probe based antenna measurement systems suffer from another kind of noise, namely the radiation of the probe. When the AUT is configured as the receiver, the resulting measured signal is a product of the interaction between the AUT and the probe with the incoming signal. This results in a reduced measurement dynamic range, as the instrumentation could not measure below a threshold defined by the probe radiation properties. This threshold, according to the article, could be obtained by measuring the radiation pattern of the probe matched with a 50 Ohms lumped load, like that found on calibration substrates. In other words, the resulting signal is a simple sum of the signal coming from the probe with the signal coming from the antenna. If this is the case, the system must be characterized in terms of probe received power in function of the RA position. Posteriorly, antenna measured values that touch these should be labeled as inaccurate.

Fig. 47 shows tests concerning the probe radiation properties. Using a H-plane radiation pattern for 9 different frequencies of V band, five scenarios were analyzed: probe connected to an antenna (blue trace), probe without contacting and keeping the antenna below it (black), probe contacting a 50 Ohms load from a Calibration Kit (red), probe without contact and keeping the Calibration Kit below it (pink), and probe without anything below it (green).

It is possible to see a great similarity for the traces in the three scenarios in which the probe had no contact, ie. probe in an open configuration. The differences between traces are more pronounced for the extremes of the interval, and are caused by the material's boundary change. Another clear point is that there is a reduced received power when the probe is connected to the load. This reduction, however, becomes smaller as the frequency increases.

Figure 47: Tests concerning the probe radiation effects.

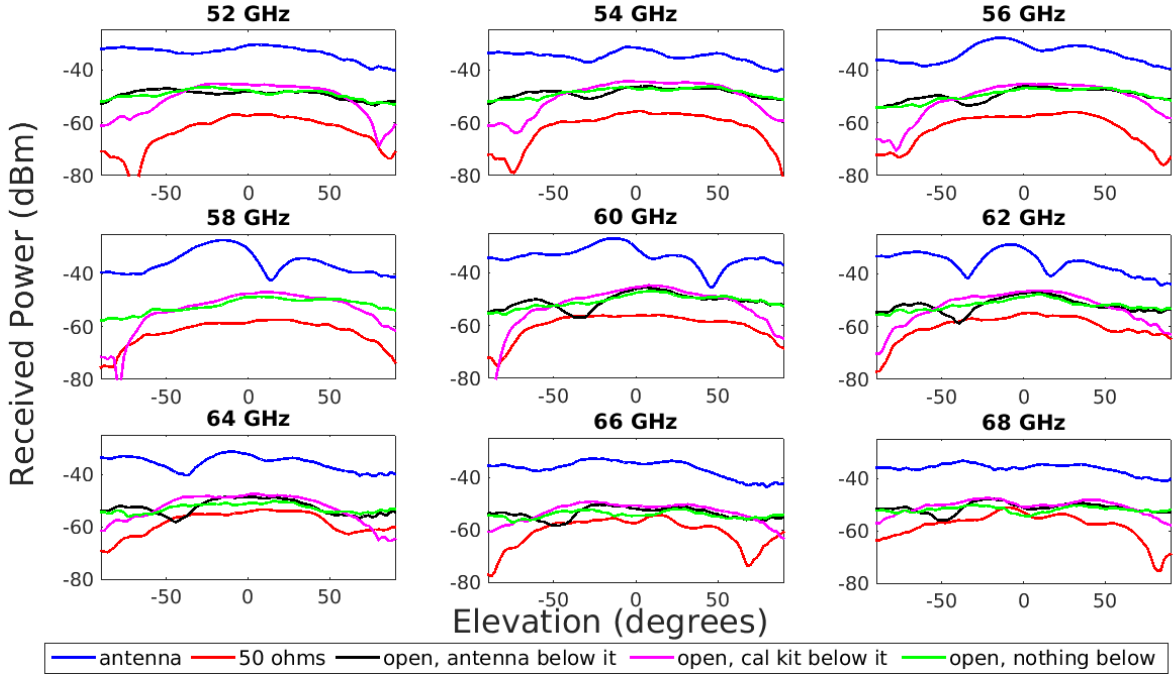

Source: author. Radiation pattern measurement of the H-plane for 9 different frequencies belonging to the V band. “Open”, in the legend, corresponds to the probe not connected to anything.

As the antenna measured at Fig. 47 doesn’t have lower valleys, it was not possible to test the assumption presented in [35], in which the blue trace will never be below the red trace. New studies and measurements must be made to prove this hypothesis. One possible test would be to measure the antenna in a cross-polarization configuration. According to the results presented with this test, it will be possible to verify if the effect of the probe in the measurement is to add power to the measured signal, or if a more sophisticated modeling should be done.

4.2.5 Summary of System Imprecisions

The accuracy of the antenna measurement is a combination of the accuracies of the instrumentation, movementation setup, RA misalignment, AUT misalignment and radiation probe effects. In the presented setup, it was concluded that:

- Because of the laser system and the AUT micropositioners, the AUT misalignment could be arbitrarily small, depending only on the system operator.
- The RA misalignment is caused by the RA_d1 error source, which is a translational positioning misalignment of the mobile metal arm of the

mechanical part of the system. Its influence in the measurements is calculated based on the angular variation (α) misalignment of the RA and the gradient of the radiation pattern measurements of the AUT. More studies need to be done to understand if the RA_d2 error source influences the measurements.

- The instrumentation error is a function of the frequency, VNA received power and test duration. It was shown that it is the main responsible for the error of the radiation pattern measurements. Nevertheless, in the measured points, its error values are below 0.2 dB, which are reasonable accuracy values.
- It was shown that the step movementation error is lower than 0.2°. Using a very directional antenna, it was shown that the measurement errors associated with this step in radiation pattern measurements are much smaller than the instrumentation errors. That way, when considering the instrumentation errors into the measurements, it is possible to disconsidered the movementation error.
- Although more studies must be performed in the probe effects subject, it is possible to say that the probe reduces the dynamic range in radiation pattern measurements.

It is possible to conclude that the accuracy of the radiation pattern in far-field antenna measurement systems is well modeled. This section provides methods to use the antenna measurement system to test itself. Furthermore, these methods were used in the presented antenna measurement system, which shows very small errors, which translates into a great implementation of the proposed objective.

For the calculation of the gain errors, the problem is much greater . In addition to the inaccuracies presented in this section, there are those that we were unable to estimate due to lack of calibration instrumentation. That said, it's not possible to know how far our estimated *difference in guided path loss* (*DGPL,* section 2.3.2) is from the real one. Furthermore, the standard gain antenna value error presented by the manufacturer is +-1 dB for the whole band, which is a large variation. While there is no way to characterize the entire chain of passive devices present in the comparison method calculation, any error estimation would be huge and therefore useless.

4.3 Antenna Measurements

4.3.1 Design

To show the capabilities of the system, we have gathered here measurements from three devices with beam steering capability. These high complex antennas and feed circuits were designed by other researchers, as stated in the “Acknowledge” section, and fabricated at the clean-room of the Laboratory of Microelectronics, USP, Brazil. They were designed on the Metallic-nanowire-filled Membrane (MnM) substrate that has already been extensively studied by researchers at the Laboratory of Microelectronics [36]. This MnM technology consists of a 50 μm-thick nanoporous Alumina substrate, with 6.7 of dielectric constant and 0.015 of loss tangent, both at 60 GHz. The main advantage of this substrate is the easy way to obtain Through Substrate Vias (TSVs), since the nanoporous could be filled by electrodeposition of copper, which made this platform an excellent Millimeter Wave material for the conception of passive devices and for their integration with active devices. The comparison between measurement and simulation in the below examples demonstrate the maturity of this technology, both in terms of modeling and fabrication.

The measurement inaccuracies are not present in the following results for some reasons: instrumentation error was not completely characterized in frequency, power level and measurement time, and the RA alignment error could not be calculated because the mechanical part and the frequency measurement band has changed several times since these measurements were performed. The reader, however, could have an error estimation for the V band measurements using the data collected at Section 4.2.

4.3.2 V Band 8-element patch array

The layout of these antennas are shown at Fig. 48(a). There are four 8-element arrays, two 4-element arrays and two 2-element arrays in this 1 inch MnM wafer. These arrays are formed of equally spaced patch antennas, distanced by $\lambda_g/2$, where λ_g is the guided wavelength at 60 GHz. The array presents a frequency-beamforming, ie. sweeping the frequency causes the principal radiation lobe swept at the E-plane. In this section we will only discuss the 8 element array.

As the nanoporous alumina is not completely flat after processing, the wafer was glued onto a glass base before being placed on the AUT measurement location. Fig. 48(b,c) shows the positioning of the AUT and the connection with the probe. Note that the azimuth motor position of the RA spherical positioning system: it is one of the E-planes positions, and it will be fixed there for all the measurements of this section. The negative elevation side is when the RA is more close to the probe than of the AUT.

Figure 48: Image of the 8-element V band patch array and its placement in the system.

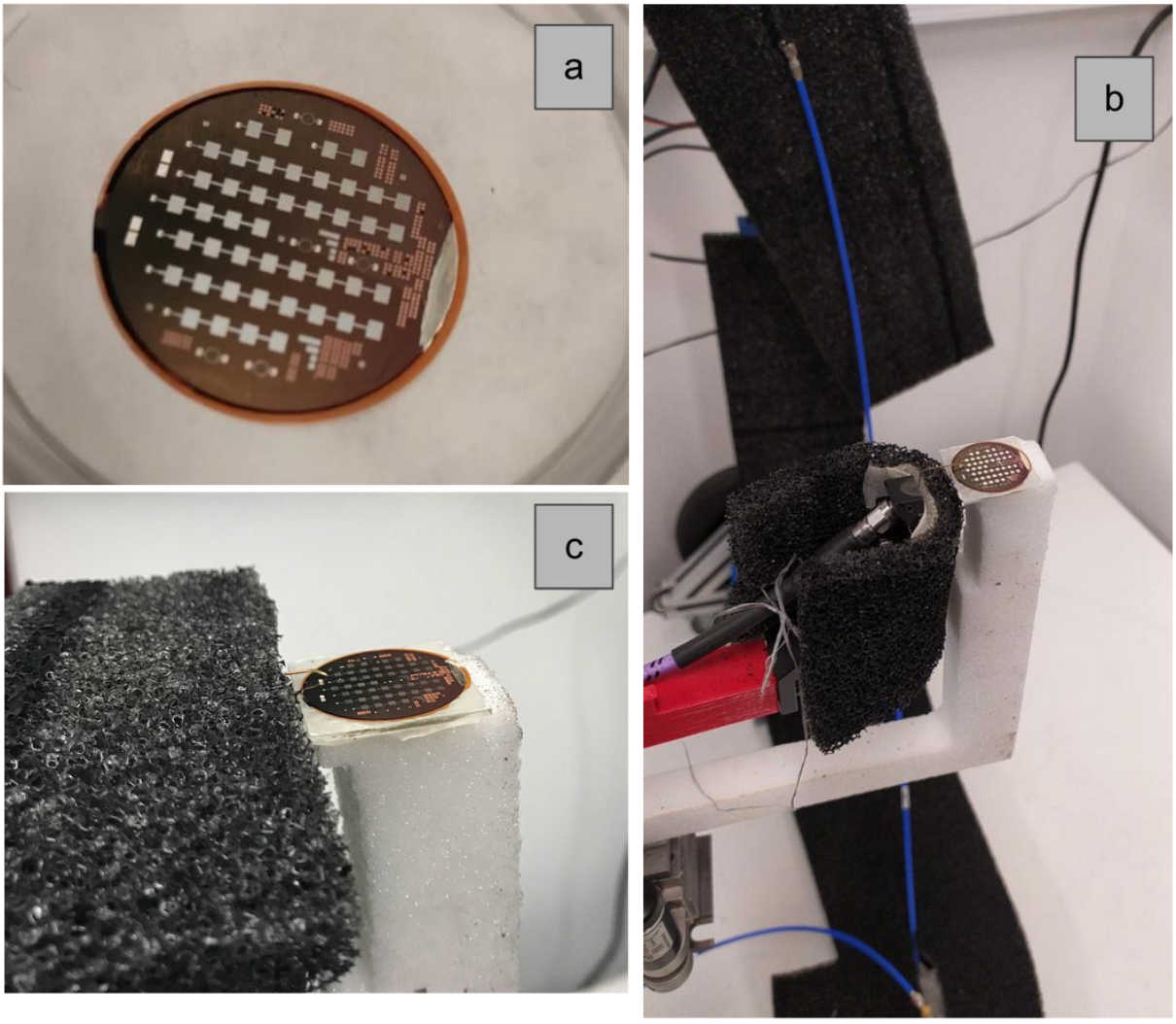

Source: author. (a) shows the 1 inch MnM wafer, with several Millimeter Wave devices, including the 8 element patch array; (b) and (c) are photographs of the MnM wafer resting above the AUT base, after contacting between the probe and the AUT pads.

Fig. 49 shows the measured frequency-beamforming behavior. For lower frequencies, the beam is positioned at the negative elevation positions, for example ~-60° for 50 GHz. For higher frequencies, the beam is located at positive elevations positions, as for ~+40° for 70 GHz. One thing to notice in these measurements is the

lack of ripple, ie. the measures are very smooth. This indicated few reflections of the signal in the system. The array has a better performance at 60 GHz, as shown by simulations in Fig. 50.

Figure 49: Gain pattern measurement of the E-plane of the V band 8-elements patch array.

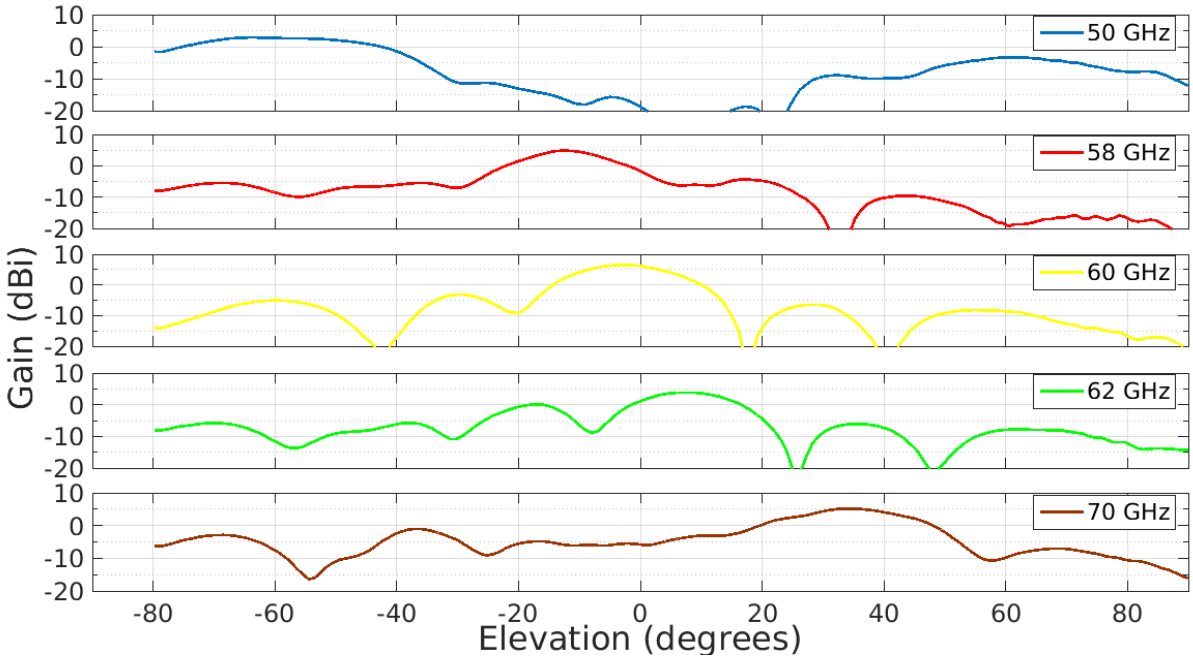

Source: author. The graphs are gain patterns, ie. a combination of radiation pattern and gain measurements, as stated in Eq. 19. Notice that sweeping from 50 to 70 GHz continually shifts the beam from ~-60° to ~+40°.

Fig. 51 shows a comparison between simulated and measured radiation patterns for 58, 60 and 62 GHz. There is a good agreement between them, evidencing a good modeling and fabrication of the device. Again, the smoothness of the traces is evidenced.

The difference between the simulated and the measured radiation patterns is a function of a lot of factors, including: modeling inaccuracies, layout and fabrication divergences, the fact that the array was not detached from the substrate before measurements (influence of neighboring metals) and the presence of glass instead of air at the bottom. In the case of gain measurement, only in the case of minimum and maximum frequencies these differences are greater than the inaccuracy of the standard antenna, which is 1 dB.

Figure 50: Measurement and simulation of gain versus frequency of the V band 8-elements patch array.

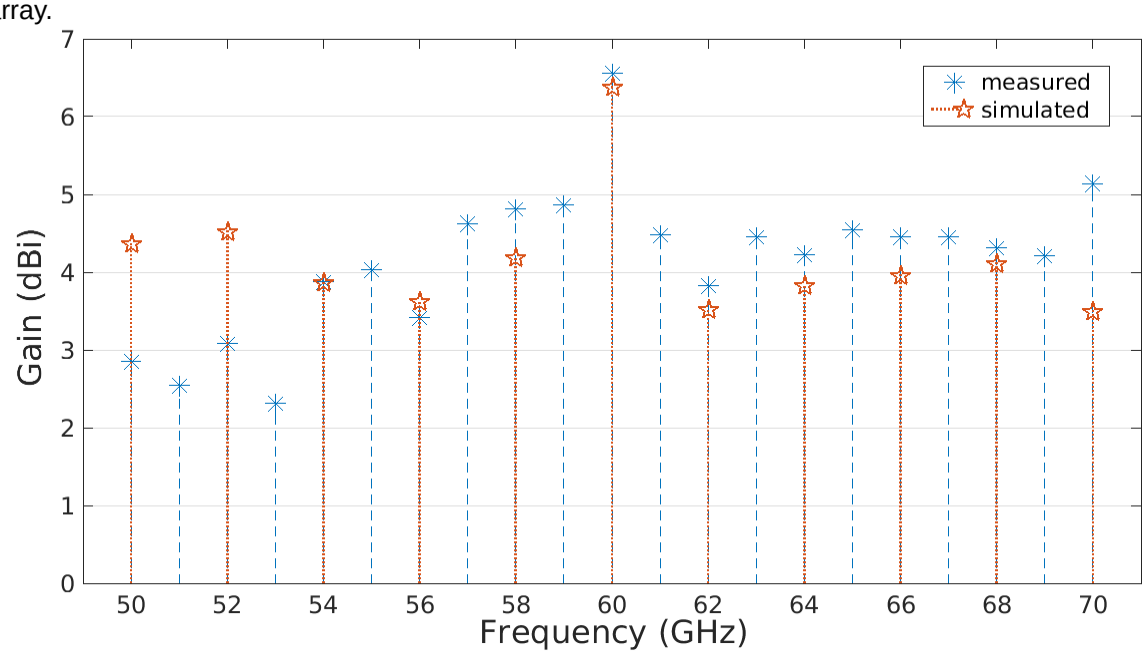

Source: author. The simulated points are 2 GHz apart, while the measured points are 1 GHz apart.

Figure 51: Simulated and measured radiation patterns of the V band 8-elements patch array, for three frequencies around the 60 GHz.

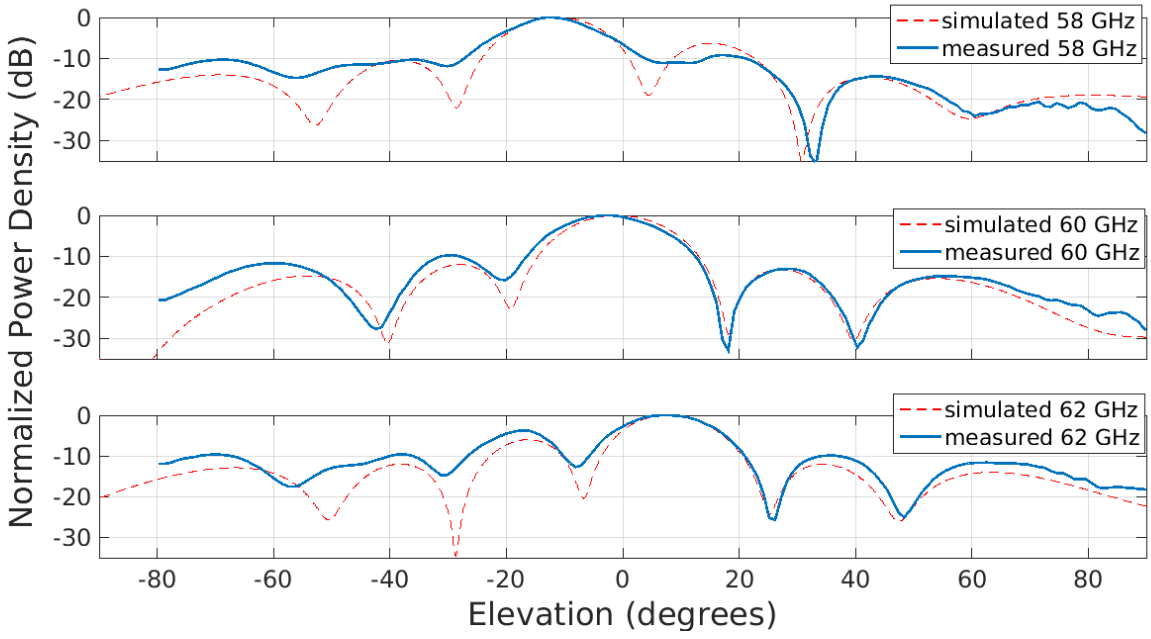

Source: author.

Finally, in Fig. 52 it is shown the reason why it is not possible to say that a Millimeter Wave antenna measurement system is good just by comparing the simulated and the measured traces. This figure makes a comparison between the four devices manufactured in the same process, sharing the same wafer, as shown in Fig. 48(a). The graphs are from E-plane measurements, all at 58 GHz. It is possible

to notice that the traces have the same behavior, but the angular position of nulls and crests changes a lot from device to device. As we are dealing with very small devices, a small variation at any stage of manufacture greatly alters the device's response to the stimulus.

Figure 52: Simulated and measured gain patterns for four same layout 8-element array patch antenna devices, all sharing the same MnM wafer.

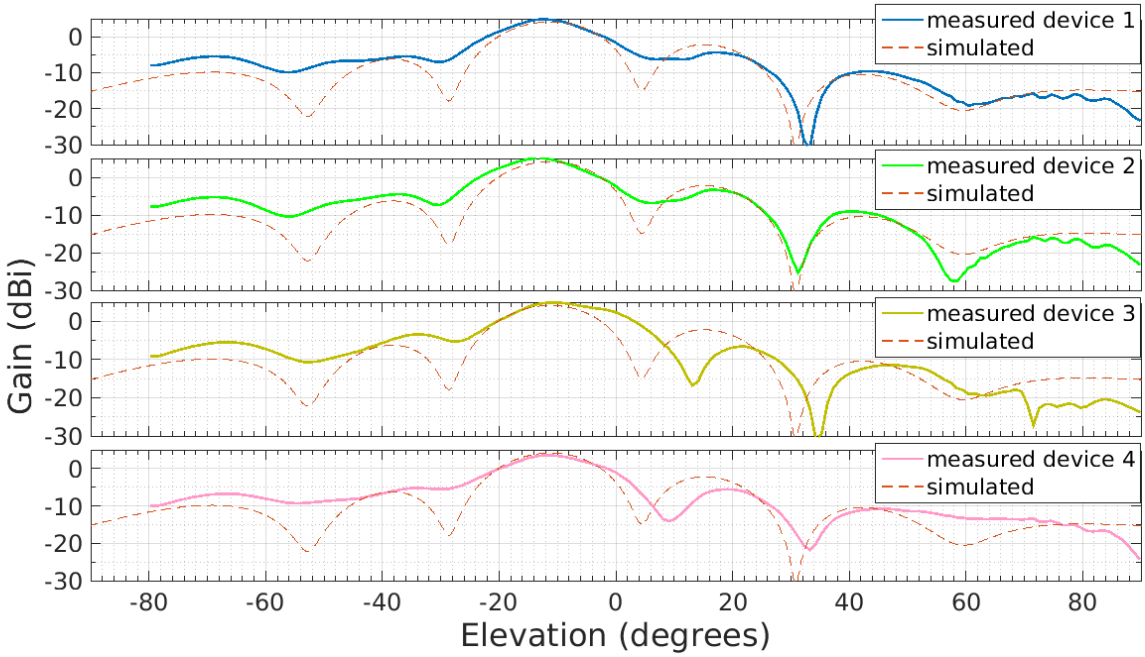

Source: author. The difference is caused by process variation across the wafer, as well as the position of the device and its surroundings.

4.3.3 V Band 4x4 Butler Matrix with 4-element patch array

Butler Matrix are architectures belonging to the analog beamforming category. In this section case, the Matrix has N = 4 input ports; depending on which is feeded, the maximum radiation beam takes one of N = 4 directions. A complete revision of this device developed at the same substrate is presented at Ref. [37]. At each output port, instead of a single patch as would be usual, the designers introduced an 4-element series patch antenna array. This array has the same behavior of the previously presented 8-element array, but has less gain as must be expected from less elements. This device in this section was published in Ref. [38], in which the design of all the basic blocks and the manufacturing processes are explained. The project is centered at 60 GHz. A photograph of this structure is shown in Fig. 53.

In Fig. 54, there is a comparison between measurement and simulation of the H-plane 2D radiation pattern at 60 GHz for all the four ports. Datatips show a very good agreement for values and positions of the maximum lobes.

Figure 53: Image of the V band Butler Matrix and its placement in the system.

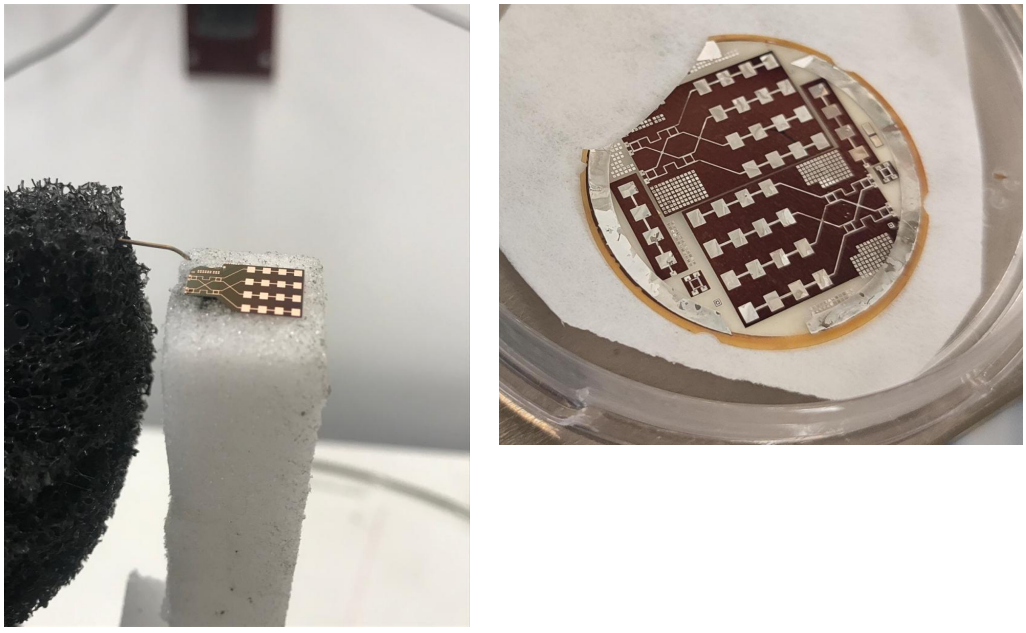

Source: author.

Figure 54: Measured and simulated traces for the V band Butler Matrix at 60 GHz.

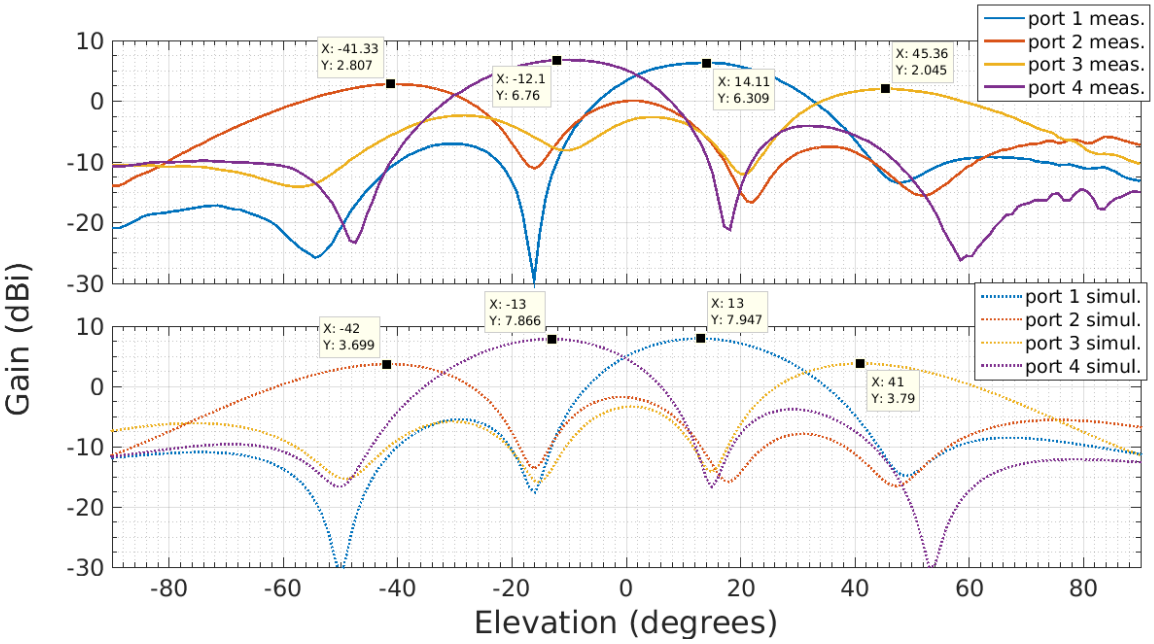

Source: author.

The E-plane radiation pattern wouldn't give us understandable results, as the maximum beam doesn't belong to it. This is a scenario where the 3D radiation pattern proves useful. Despite being hard to present, this measurement has all the information about the direction of the beam. Measured data were acquired from -70° to +70° elevation, with a step of 2°, at 18 planes from -90° to +90° azimuth. For each spherical point, the RA rotates 30 times. This means a total of 179*18*30=96660

samples. For each port, this measurement takes about 1 whole day.

Here, we will present these results in two different ways. Fig. 55 shows a 2D graph of the 3D radiation pattern data. It is a top view of the cartesian graph (XY view). The 12 portions correspond to individually feeding 3 frequencies to each of the 4 ports; the scale is decibel-milliwatts. This figure is intended to show the variation position of the maximum beam while changing the feed port and the frequency. For example, when feeding port 1 and changing the frequency (first column of graphs), the maximum will almost follow a ‘y’-movement (with ‘x’ constant) trajectory of the RA. Another example is keeping the frequency at 60 GHz and changing the feed port (second line of graphs); knowing that the equator line corresponds to the H-plane (red trace), it is possible to notice that the behavior of the Fig. 54 is repeated here.

Figure 55: XY projection of the 3D radiation pattern of the V band Butler Matrix.

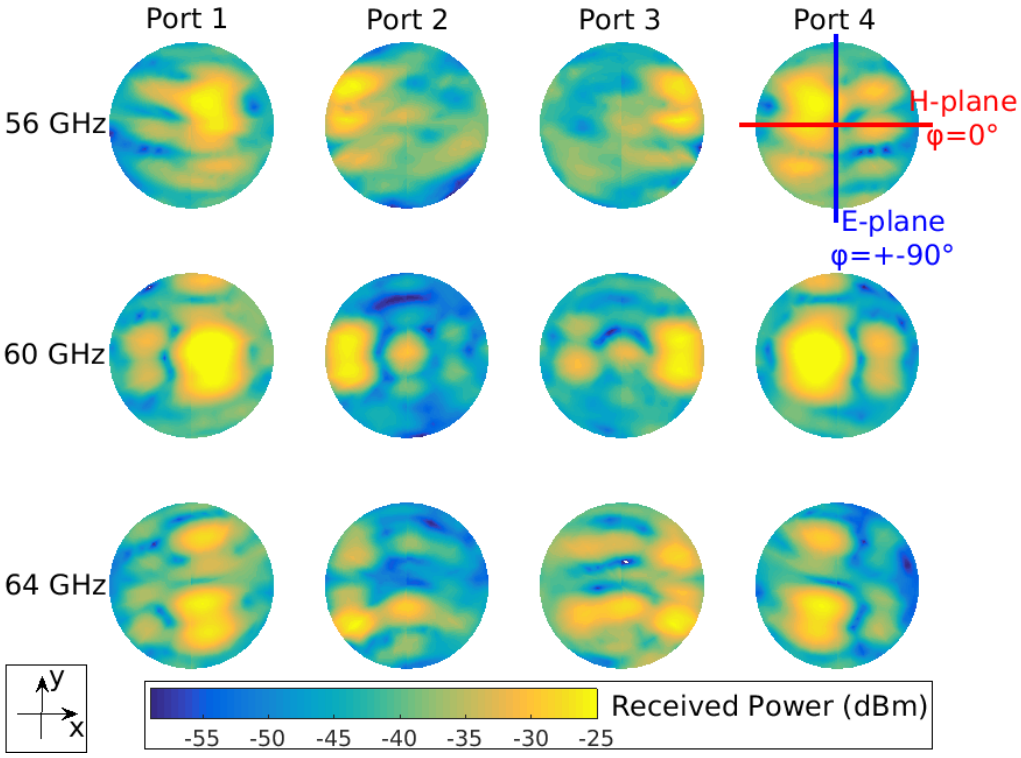

Source: author.

The second form of visualization is a 3D spherical plot, shown in Fig. 56. The azimuth and elevation are already intrinsic to the acquired data. The radius and the colors are two ways of representing the radiation pattern data, that is, the normalized power density. In the control software presented in section 3.4, the radius is a representation of the decibel data, and the color has a linear scale (milliwatts). The charts of Fig. 56 were extracted from this developed control software. Through the

graph it is possible to see the behavior of the main beam when changing ports and varying the frequency.

Figure 56: Control software plot of the 3D radiation pattern of the V band Butler Matrix.

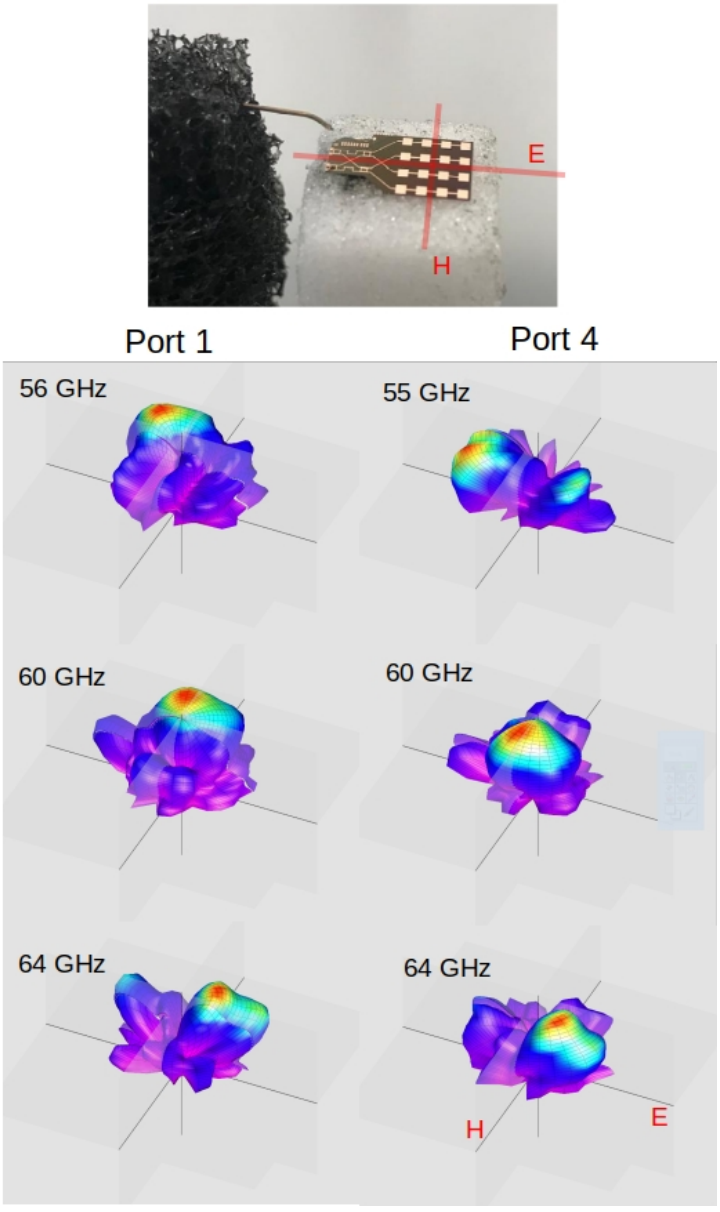

Source: author.

4.3.4 W Band 4x4 Butler Matrix

In this section, it's shown a 4x4 Butler Matrix (BM) structure operating at 100 GHz. Unlike the previous section device where a patch array was used on each output port, in this case there is a single patch connected to each one of them. This means that the beamforming is only in the H-plane, controlled by choosing the excitation input port. A photograph of a very first measurement of this device is at

Fig. 57(a), in which the entire wafer is placed in the AUT base. For a more accurate measurement of the matrix, it was detached from the MnM wafer through a laser cutter, as shown at Fig. 57(b); the measurements presented at this section are from this isolated matrix.

Figure 57: Image of the W band Butler Matrix and its placement in the system.

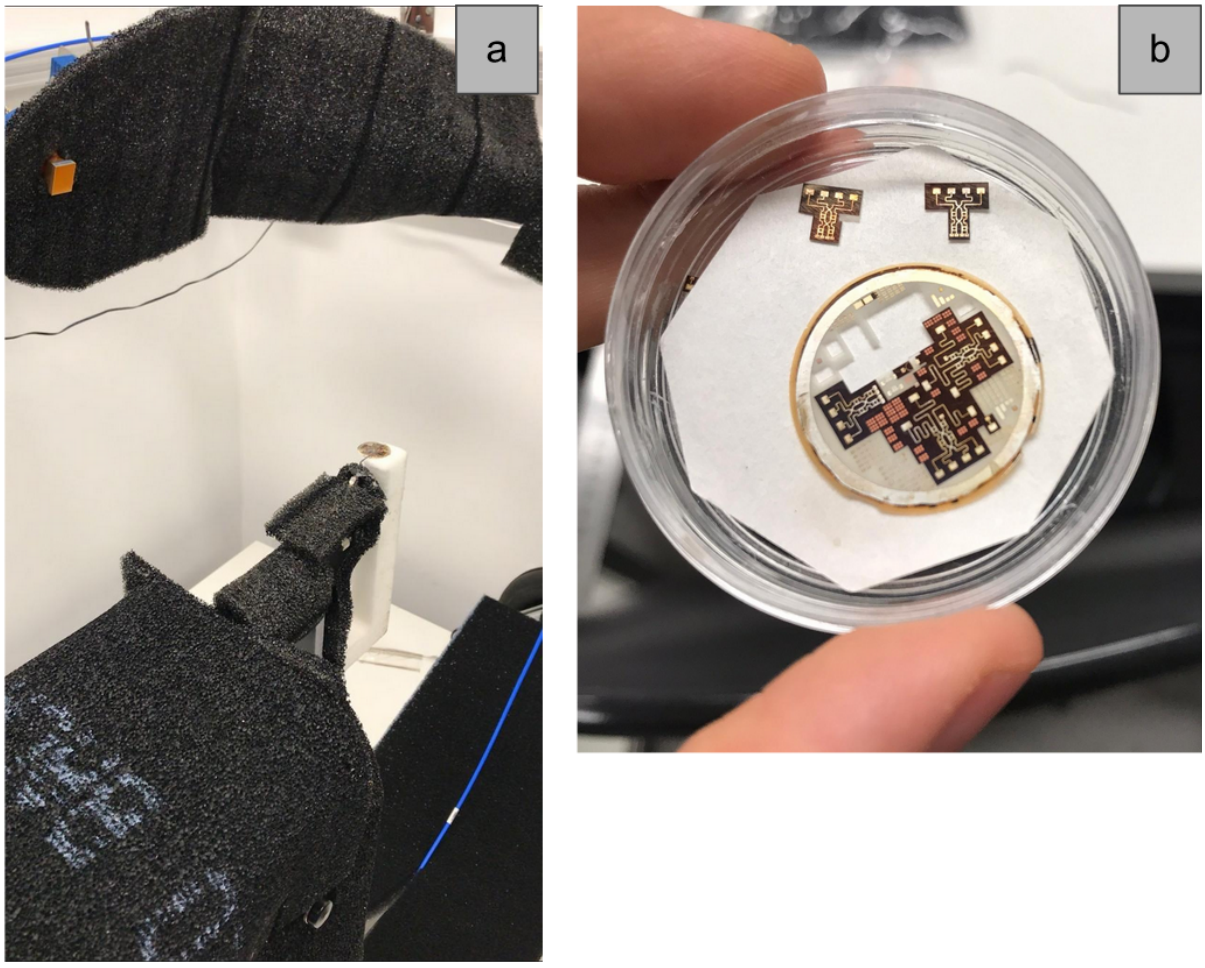

Source: author. (a) W band configuration measuring the BM inside the MnM wafer. The RA is at some negative elevation position. (b) BM detached from the MnM wafer. The ports are numbered from 1-4, from left to right.

The radiation pattern of the H-plane is shown at Fig. 58(a). As this device is symmetrical, the crossing point between the main lobes of ports 1 and 4 is the AUTCS 0° elevation and, in this measurement case, it is at 2° elevation. If we subtract this offset from the independent variable in all port measurements, it's possible to see that the beam is able to be switched to 12°, −45°, 45° and −12° when excited by port 1, 2, 3, 4, respectively. The maximum gains of each port were sought and measured, and are presented at Fig. 58(b). At 100 GHz, they are 5.49 dBi, 3.77 dBi, 3.32 dBi and 4.93 dBi, respectively from port 1 to 4. It is only presented here the measurements data, as the designer didn't simulate the whole operating device --

which would be a very large and time consuming simulation. These results are expected to be published soon.

Figure 58: Measurements results of W Band Butler Matrix.

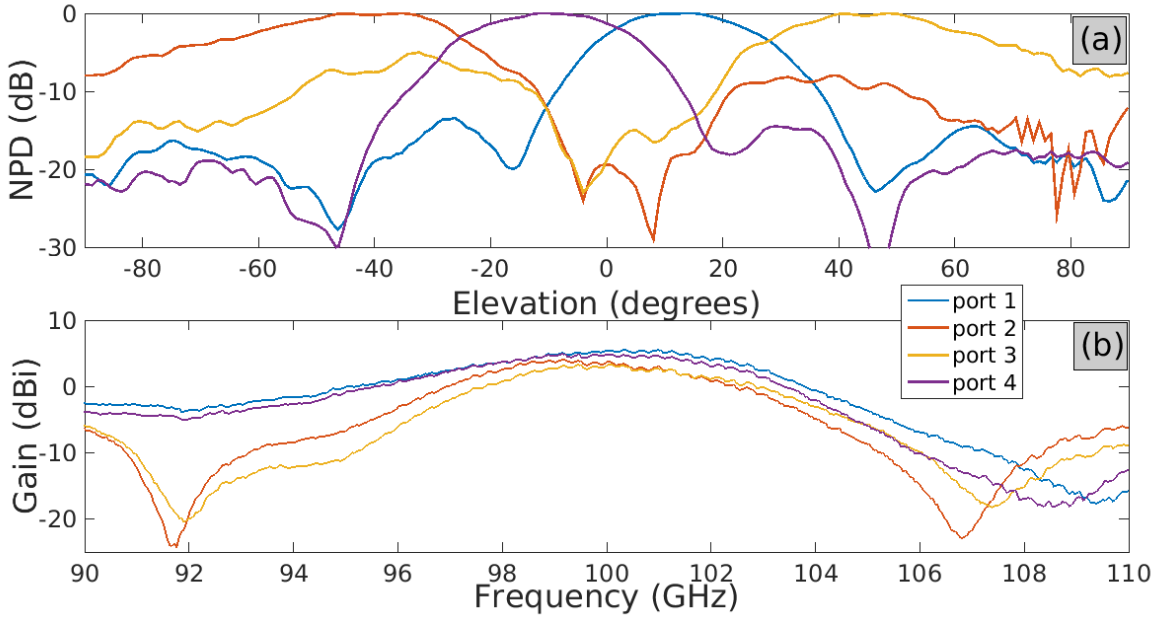

Source: author. (a) Measurement of the radiation pattern for each of the matrix input ports; NPD is an abbreviation for Normalized Power Density. (b) Gain measurement for each input port; notice that the outer ports have a higher gain than the inner ports.

The analysis of the radiation patterns from the V band and W band measurements indicates that the W band radiation pattern shows more prominent ripple or fluctuations. These variations can be attributed to reflections caused by the presence of metal parts in close proximity to the Antenna Under Test (AUT). It is worth noting that the same absorbers were utilized to mitigate probe reflections for both frequency bands. As a result, the laboratory has plans to purchase additional absorbers specifically designed for these higher frequency bands in order to further improve the accuracy of the antenna characterization system.

5 Conclusion

A solid alternative to society's growing demand for data exchange is to establish communication channels at Millimeter Wave frequencies. Antennas play a crucial role in wireless systems, as their performance directly impacts the overall system performance. Therefore, accurate testing of these devices is essential. However, antenna characterization at these frequencies poses technological and cost challenges. This dissertation work aims to address this pressing issue by presenting one possible solution for creating an in-house antenna characterization system. Along with the development of the system, establishing appropriate test routines to validate the correctness of the configuration is also emphasized.

The development of an effective antenna characterization system requires careful consideration of several key factors. Firstly, a thorough review of the state of the art of existing antenna characterization systems worldwide is essential (Chapter 1). Secondly, a deep understanding of antennas performance metrics and parameters is crucial (Chapter 2). Lastly, delimiting the necessary instrumentation and comprehending their behavior and limitations is critical to the success of the characterization system (part of Chapter 3). In Chapter 3, the developed antenna characterization system is presented, encompassing the culmination of the insights gained from the previous chapters.

In the first part of Chapter 4, methods were developed to utilize the far-field antenna characterization system for self-testing. Using these tests in the developed system, it was determined that the main source of inaccuracy in the radiation pattern measurements is the instrumentation error, which is dependent on factors such as frequency, received power in the Vector Network Analyzer (VNA) receiver, and test duration. For the points tested in this work, the instrumentation error values were consistently below 0.2 dB. Additionally, it was shown that the mechanical misalignment was limited to approximately 1 mm, and the motor stepper error was found to be lower than 0.2°.

In the second part of Chapter 4, the developed antenna characterization system was employed to perform measurements on real antennas. Comparisons were made between fabrications and simulations. The results obtained demonstrated the system's ability to capture subtle nuances of the fabricated antennas with a wide dynamic range. Notably, the measurements in the V band exhibited smoothness,

indicating the absence of signal reflections and the system's accuracy in capturing the antenna's performance in this frequency range. However, it was observed that the measurements in the W band appeared to be slightly noisier, suggesting that the performance of the absorbers may not be as efficient at these higher frequencies. Furthermore, this chapter also discusses various formats of data presentation, highlighting the attention to detail and thorough analysis conducted to effectively present the measured results. The utilization of appropriate data presentation formats adds to the rigor and comprehensibility of the findings, further underscoring the robustness and reliability of the developed antenna characterization system.

These exceptional results strongly suggest that the developed antenna characterization system is well-implemented and capable of reliable and precise performance. The thorough testing and validation conducted in Chapter 4 serves as a robust proof of the correctness and effectiveness of the system, reaffirming its potential for practical applications in the field of antenna characterization at Millimeter Wave frequencies.

Future work in enhancing the capabilities of the developed antenna characterization system could include the development of a directivity calculation algorithm based on the 3D radiation pattern, which would enable more accurate characterization of the antenna's radiation pattern. Mapping the instrumentation accuracy in terms of frequency, received power level, and test period could provide valuable insights into the system's performance and enable improved error estimation and correction techniques. Additionally, modeling the influence of probe radiation on the measured results could be explored. Finally, efforts could be employed to estimate the scattering parameters of the passive device chain, in order to allow gain error calculations. Addressing these areas of future work would contribute to the continued advancement and refinement of the developed antenna characterization system, leading to more precise and reliable characterization of antennas in Millimeter Wave frequency bands. These endeavors have the potential to open up new opportunities for further advancements and innovations in the field of antenna characterization, ultimately enhancing the performance and capabilities of the developed system.

REFERENCES

[1] HARARI, Y. N. **Homo Deus: A Brief History of Tomorrow**. Harper, 2017.

[2] STANDAGE, T.. **The Victorian Internet: The Remarkable Story of the Telegraph and the Nineteenth Century's On-line Pioneers**, 2ed. Bloomsbury USA, 2014.

[3] STONE, J. V. **Information Theory: A Tutorial Introduction**. Sebtel Press, 2015.

[4] MACKAY, David. **Information Theory, Inference, and Learning Algorithms**. Cambridge University Press, 2003.

[5] WIKIPEDIA, **IEEE 801.11**. Available in: https://en.wikipedia.org/wiki/IEEE_802.11. Accessed on: 04/03/2023.

[6] NATIONAL TELECOMMUNICATIONS AND INFORMATION ADMINISTRATION (NTIA). **Federal Government Spectrum Use Reports (225 MHz - 7.125 GHz)**. Available in: https://ntia.gov/page/federal-government-spectrum-use-reports-225-mhz-7125-ghz. Accessed on: 04/03/2023.

[7] NOKIA. **5G Carrier Aggregation Explained**. Available in: https://www.nokia.com/about-us/newsroom/articles/5g-carrier-aggregation-explained/ . Accessed on: 04/03/2023.

[8] NATIONAL TELECOMMUNICATIONS AND INFORMATION ADMINISTRATION (NTIA). **How the Spectrum is Used**. Available in: https://www.ntia.doc.gov/book-page/how-spectrum-used. Accessed on: 04/03/2023.

[9] AKDENIZ, M. R. et al. **Millimeter Wave Channel Modeling and Cellular Capacity Evaluation**, IEEE Journal on Selected Areas in Communications, vol. 32, no. 6, pp. 1164-1179, June 2014. DOI: 10.1109/JSAC.2014.2328154.

[10] RAPPAPORT, T. S. et al. **Wireless Communications and Applications Above 100 GHz: Opportunities and Challenges for 6G and Beyond**, IEEE Access, vol. 7, pp. 78729-78757, 2019, DOI: 10.1109/ACCESS.2019.2921522.

[11] LIOU, J.J.; SCHWIERZ, F. **RF MOSFET: Recent Advances, Current Status and Future Trends**, Solid-State Electronics, Vol. 47, no 11, pp. 1881-1895, 2003. DOI: 10.1016/S0038-1101(03)00225-9.

[12] NIKNEJAD, A. M.; HASHEMI, H. **mm-Wave Silicon Technology: 60 GHz and Beyond**. Springer, 2008.

[13] NSI-MI TECHNOLOGIES LLC. Available in: https://www.nsi-mi.com/. Accessed on: 04/03/2023.

[14] AMETEK INC. **Ametek Acquires NSI-MI Technologies.** Available in: https://investors.ametek.com/news-releases/news-release-details/ametek-acquires-nsi-mi-technologies. Accessed on: 04/03/2023.

[15] UNIVERSITY OF SHEFFIELD. **About the mmWave Facility.** Available in: https://www.sheffield.ac.uk/mm-wave/about. Accessed on: 04/03/2023.

[16] BOEHM, L. et al. **The Challenges of Measuring Integrated Antennas at Millimeter-Wave Frequencies** [Measurements Corner], IEEE Antennas and Propagation Magazine, vol. 59, no. 4, pp. 84-92, 2017, DOI: 10.1109/MAP.2017.2706652.

[17] RENIERS, A. C. F. et al. **Review of the accuracy and precision of mm-wave antenna simulations and measurements**. In: 10th European Conference on Antennas and Propagation (EuCAP), Madrid, Spain, 2016. DOI: 10.1109/EuCAP.2016.7481973.

[18] RENIERS, A. C. F.; SMOLDERS, A. B. **Guidelines for millimeter-wave antenna measurements**. In: IEEE Conference on Antenna Measurements & Applications (CAMA), Vasteras, Sweden, 2018. DOI:10.1109/CAMA.2018.8530518

[19] CENTRO DE ONDAS MILIMÉTRICAS. Available in: https://sites.usp.br/centrommw/. Accessed on: 04/03/2023.

[20] BALANIS, C. A. **Antenna Theory**: Analysis and Design, 4th ed. Wiley, 2016.

[21] PARINI, C. et al. **Theory and Practice of Modern Antenna Range Measurements**. Institution of Engineering and Technology (IET), 2014.

[22] INSTITUTE OF ELECTRICAL AND ELECTRONICS ENGINEERS (IEEE). **Standard 149-1979**: IEEE Standard Test Procedures for Antennas. Published by IEEE, 1979. DOI: 10.1109/IEEESTD.1979.120310.

[23] INSTITUTE OF ELECTRICAL AND ELECTRONICS ENGINEERS (IEEE). **Standard 145-2013**: IEEE Standard for Definitions of Terms for Antennas. Published by IEEE, 2014. DOI: 10.1109/IEEESTD.2014.6758443.

[24] POZAR, D. **Microwave Engineering**, 4th ed. Wiley, 2011.

[25] DUNSMORE, J. P. **Handbook of Microwave Component Measurements**, 2nd ed. Wiley, 2020.

[26] KEYSIGHT TECHNOLOGIES. **Keysight 2-Port and 4-Port PNA-X Network Analyzer**. Available in: https://www.keysight.com/us/en/assets/9018-04526/technical-specifications/9018-04526.pdf. Accessed on: 04/03/2023.

[27] IVI FOUNDATION. **Standard Commands for Programmable Instruments (SCPI)**, Vol 1-4. Available in: https://www.ivifoundation.org/docs/scpi-99.pdf. Accessed on: 04/03/2023.

[28] TOTOKU INC. **Coaxial Cable & Assembly for Microwave**. Available in: https://www.totoku.com/product/pdf/wave_ruota.pdf. Accessed on: 04/03/2023.

[29] QUANTUM MICROWAVE. **QMC-MX4-15F13 50 to 75 GHz WR-15 Active Multiplier**. Available in: https://quantummicrowave.com/product/qmc-mx4-15f13-50-to-75-ghz-wr-15-active-multiplier/. Accessed on: 04/03/2023.

[30] QUANTUM MICROWAVE. **QMC-MX6-10F10: 75 to 110 GHz WR-10 Active Multiplier**. Available in: https://quantummicrowave.com/product/qmc-mx6-10f10-75-to-110-ghz-wr-10-active-multiplier/. Accessed on: 04/03/2023.

[31] KEYSIGHT TECHNOLOGIES. **PNA help file** - “mmWave Measurements without a Test Set” section. Available in: https://www.keysight.com/us/en/lib/resources/help-files/n52xxb-pna-series-help-file.html. Accessed on: 04/03/2023.

[32] OML INC. **WR-10 Frequency Extension Module**. Available in: https://www.omlinc.com/images/pdf/VxxVNA2/OML-V10VNA2_Datasheet.pdf. Accessed on: 04/03/2023.

[33] HUBER, F. **A Logical Introduction to Probability and Induction**. Oxford University Press, 2018.

[34] BOEHM, L. et al. **Probe influence on integrated antenna measurements at frequencies above 100 GHz**. In: 46th European Microwave Conference (EuMC), London, UK, 2016. DOI: 10.1109/EuMC.2016.7824402.

[35] MOHAMMADPOUR-AGHDAM, K. et al. **RF probe influence study in millimeter-wave antenna pattern measurements**, International Journal of RF and Microwave Computer-Aided Engineering, vol. 21, no. 4, pp. 413-420, 2011. DOI: 10.1002/mmce.20530.

[36] LÉ, J. E. G., et al. **Integrated Antennas on MnM Interposer for the 60 GHz Band**. Journal of Microwaves, Optoelectronics and Electromagnetic Applications, vol. 21, no. 1, pp. 184-193, 2022. DOI: 10.1590/2179-10742022v21i1253671

[37] VERONA, B. M. **Matriz de Butler em interposer MnM para aplicações em ondas milimétricas**, Masters dissertation, Universidade de São Paulo, 2021. Available at: https://www.teses.usp.br/teses/disponiveis/3/3140/tde-31012022-123610/. Accessed on: 04/12/2023.

[38] SIMIONATO, E. et al. **Design and Analysis of a Butler Matrix at 60 GHz Compatible with Metallic-Nanowire-Filled Membrane Fabrication Platform**. In: XL Simpósio Brasileiro de Telecomunicações e Processamento de Sinais, Santa Rita do Sapucaí, Brazil, 2022. DOI: 10.14209/sbrt.2022.1570824905.

APPENDICES

APPENDIX A - ILLUSTRATED PROCEDURE FOR CHANGING THE REFERENCE ANTENNA WHEN CHANGING THE MEASUREMENT BAND

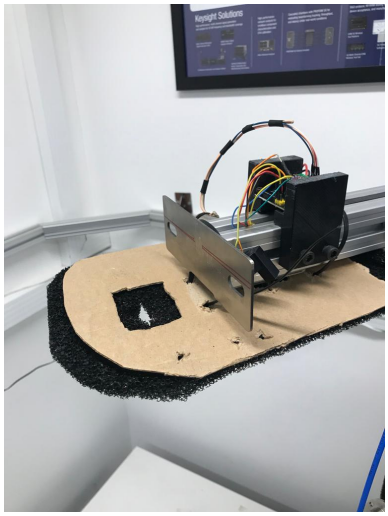

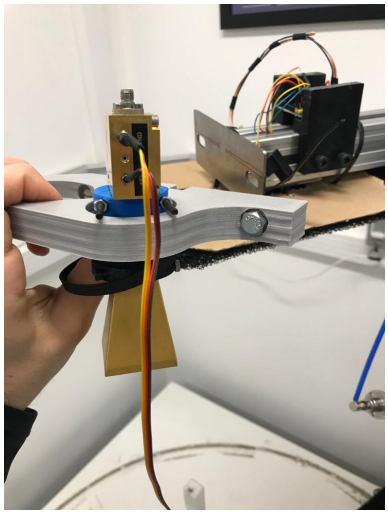

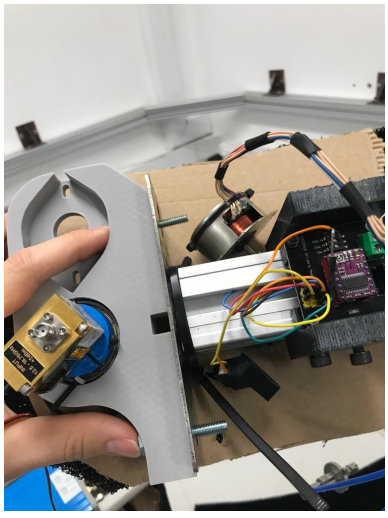

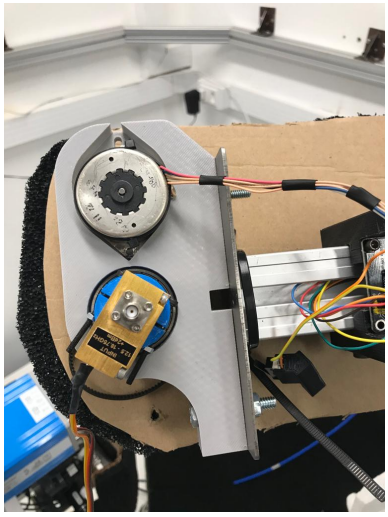

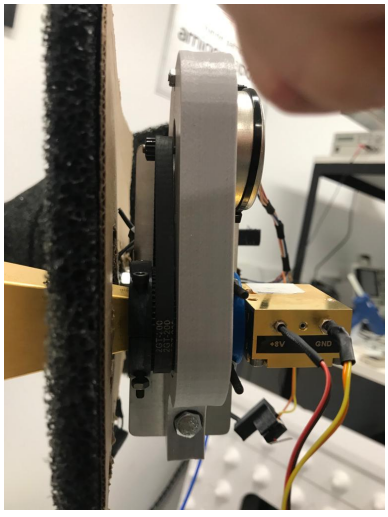

APPENDIX B - A QUICK LOOK AT THE SOFTWARE USER INTERFACE

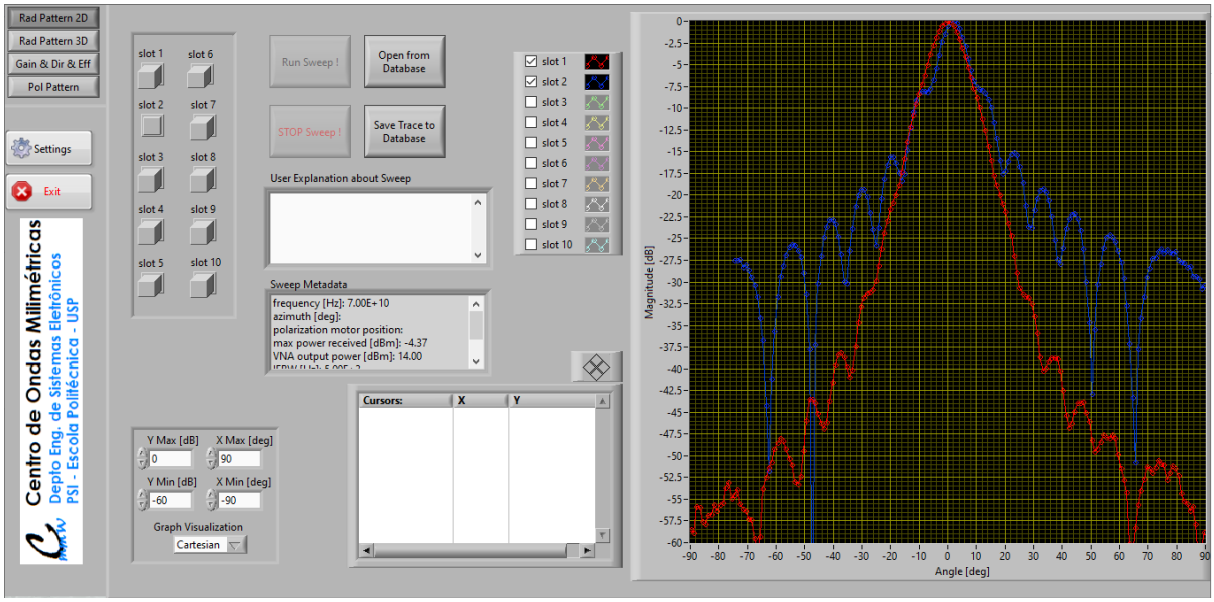

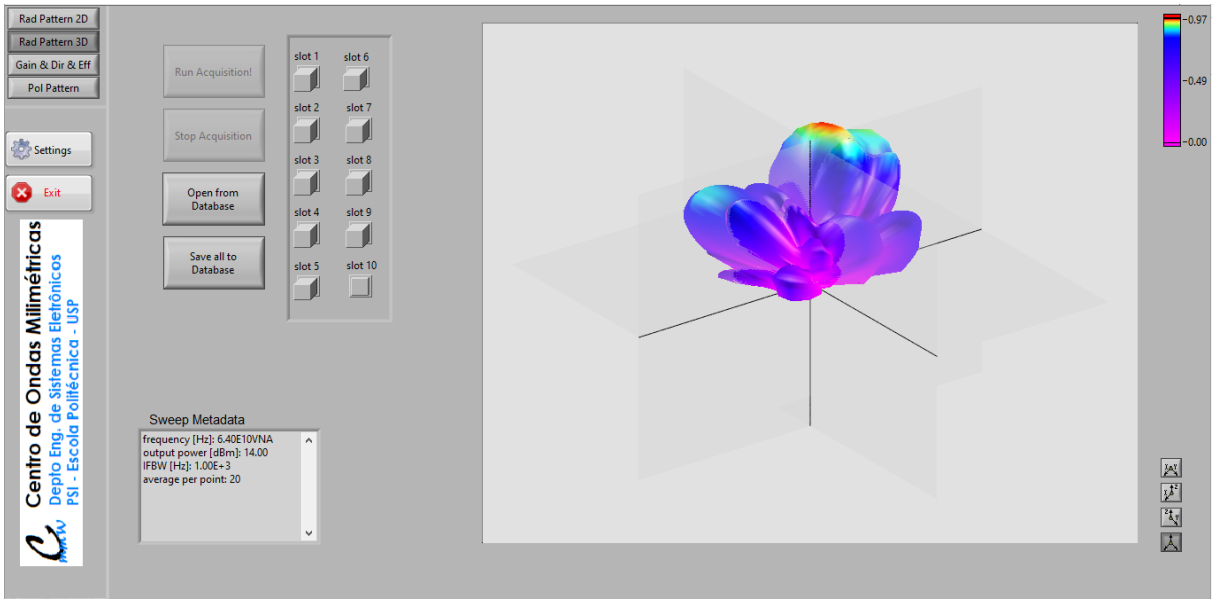

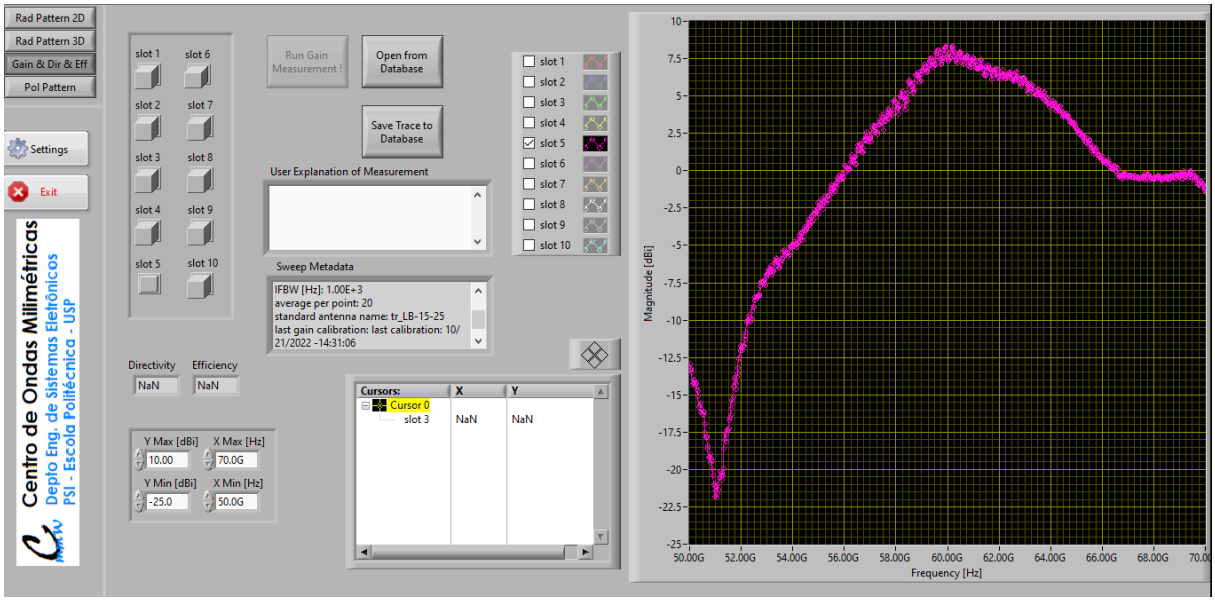
Rad Pattern 2D
Rad Pattern 3D
Gain & Dir & Eff
Pol Pattern
Settings
Exit
Centro de Ondas Milimétricas
Depto Eng. de Sistemas Eletrônicos
PSI - Escola Politécnica - USP
slot 1
slot 2
slot 3
slot 4
slot 5
slot 6
slot 7
slot 8
slot 9
slot 10
Run Gain Measurement !
Open from Database
Save Trace to Database
User Explanation of Measurement
Sweep Metadata
IFBW [Hz]: 1.00E+3
average per point: 20
standard antenna name: tr_LB-15-25
last gain calibration: last calibration: 10/21/2022 -14:31:06
Directivity
NaN
Efficiency
NaN
Y Max [dBi]
10.00
X Max [Hz]
70.0G
Y Min [dBi]
-25.0
X Min [Hz]
50.0G
Cursors:
X
Y
Cursor 0
slot 3
NaN
NaN
Magnitude [dBi]
Frequency [Hz]

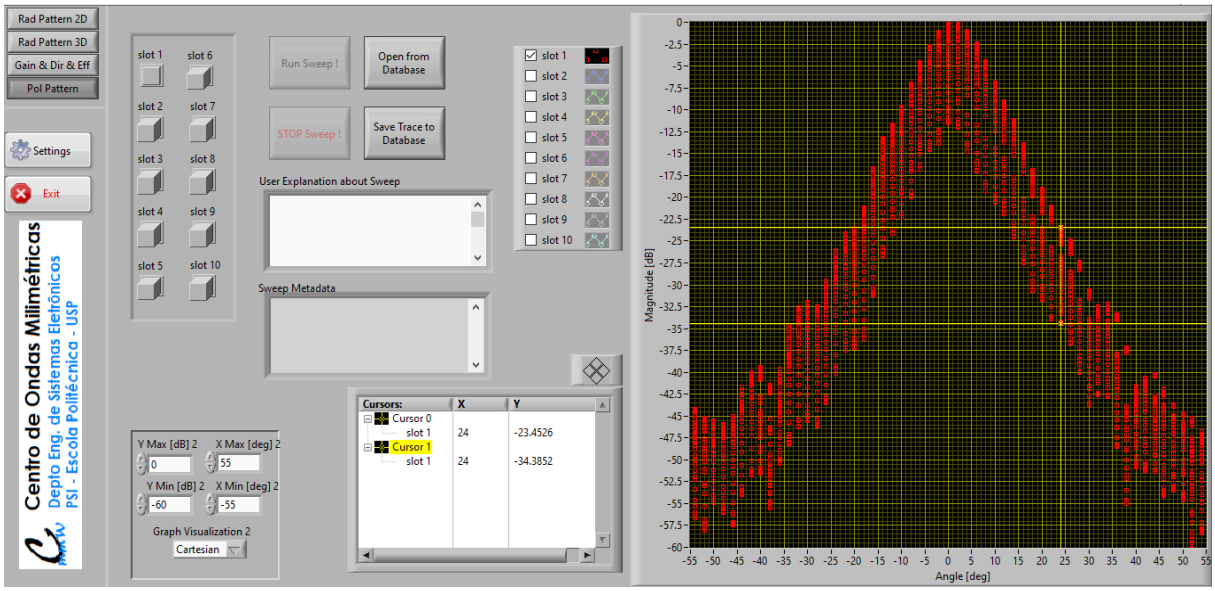
Rad Pattern 2D
Rad Pattern 3D
Gain & Dir & Eff
Pol Pattern
Settings
Exit
Centro de Ondas Milimétricas
Depto Eng. de Sistemas Eletrônicos
PSI - Escola Politécnica - USP
slot 1
slot 2
slot 3
slot 4
slot 5
slot 6
slot 7
slot 8
slot 9
slot 10
Run Sweep !
STOP Sweep !
Open from Database
Save Trace to Database
User Explanation about Sweep
Sweep Metadata
Y Max [dB] 2
0
X Max [deg] 2
55
Y Min [dB] 2
-60
X Min [deg] 2
-55
Graph Visualization 2
Cartesian
Cursors:
X
Y
Cursor 0
slot 1
24
-23.4526
Cursor 1
slot 1
24
-34.3852
Magnitude [dB]
Angle [deg]

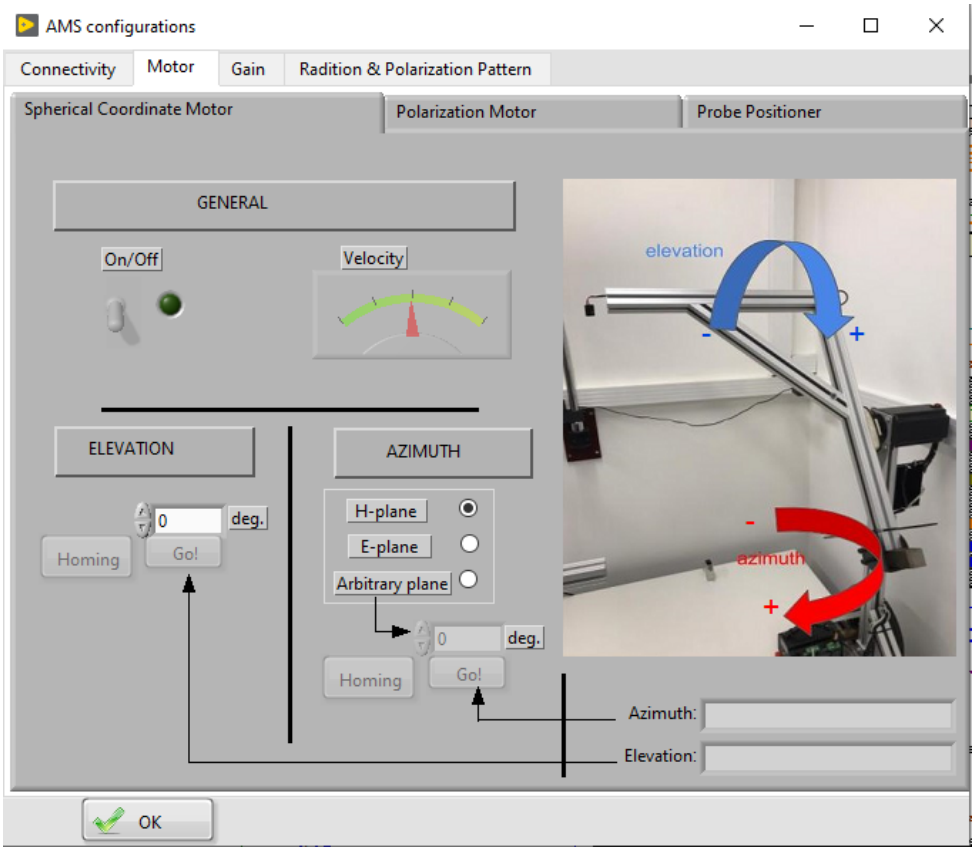
AMS configurations
Connectivity
Motor
Gain
Radition & Polarization Pattern
Spherical Coordinate Motor
Polarization Motor
Probe Positioner
GENERAL
On/Off
Velocity
elevation
azimuth
ELEVATION
AZIMUTH
deg.
Homing
Go!
H-plane
E-plane
Arbitrary plane
Azimuth:
Elevation:
OK

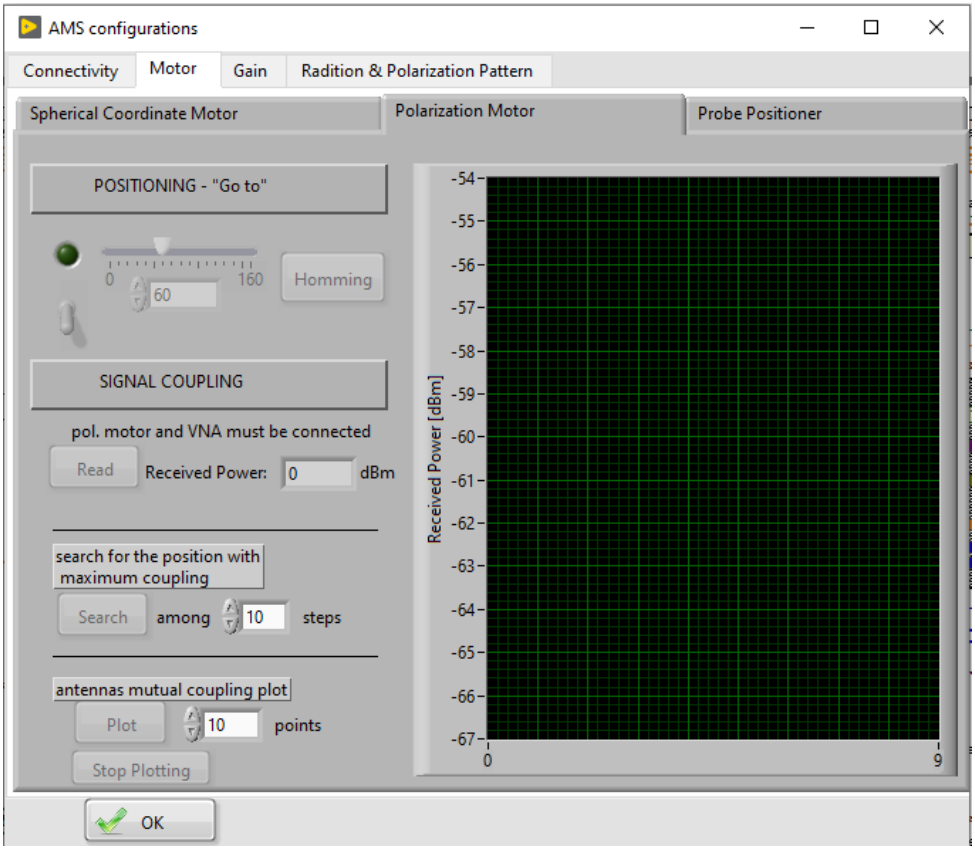
AMS configurations
Connectivity
Motor
Gain
Radition & Polarization Pattern
Spherical Coordinate Motor
Polarization Motor
Probe Positioner
POSITIONING - "Go to"
Homming
SIGNAL COUPLING
pol. motor and VNA must be connected
Read
Received Power:
dBm
search for the position with maximum coupling
Search
among
steps
antennas mutual coupling plot
Plot
points
Stop Plotting
Received Power [dBm]
OK

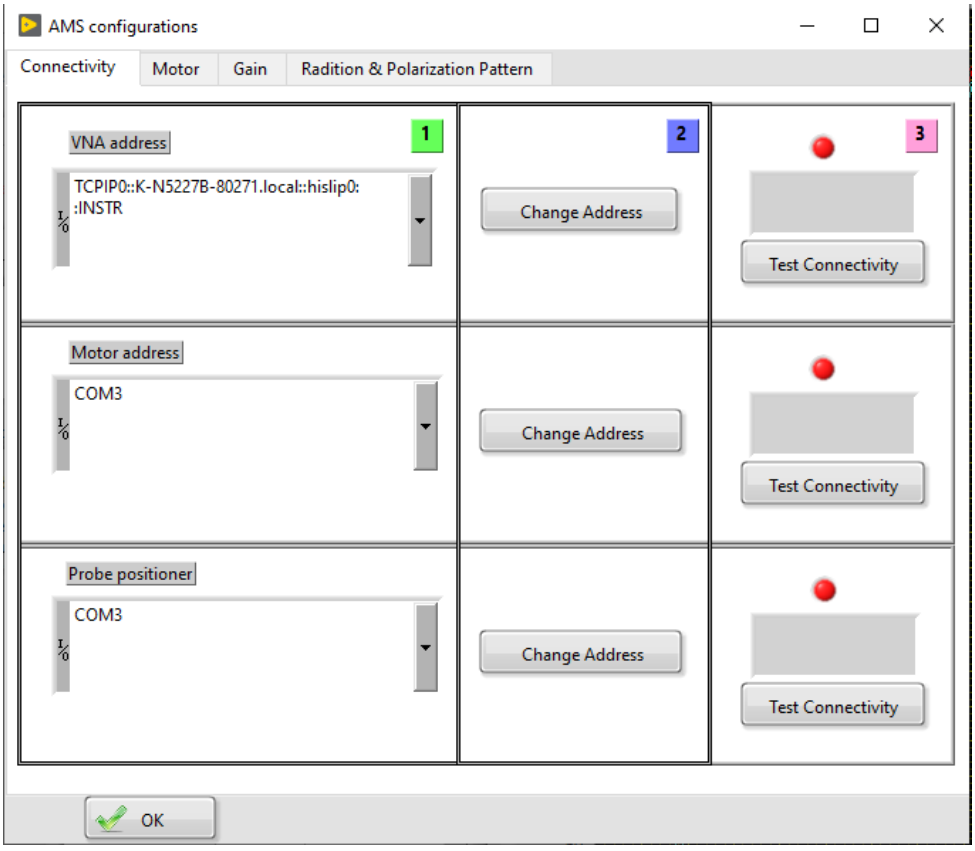
AMS configurations
Connectivity
Motor
Gain
Radition & Polarization Pattern
VNA address
1
TCPIP0::K-N5227B-80271.local::hislip0::INSTR
2
Change Address
3
Test Connectivity
Motor address
COM3
Change Address
Test Connectivity
Probe positioner
COM3
Change Address
Test Connectivity
OK

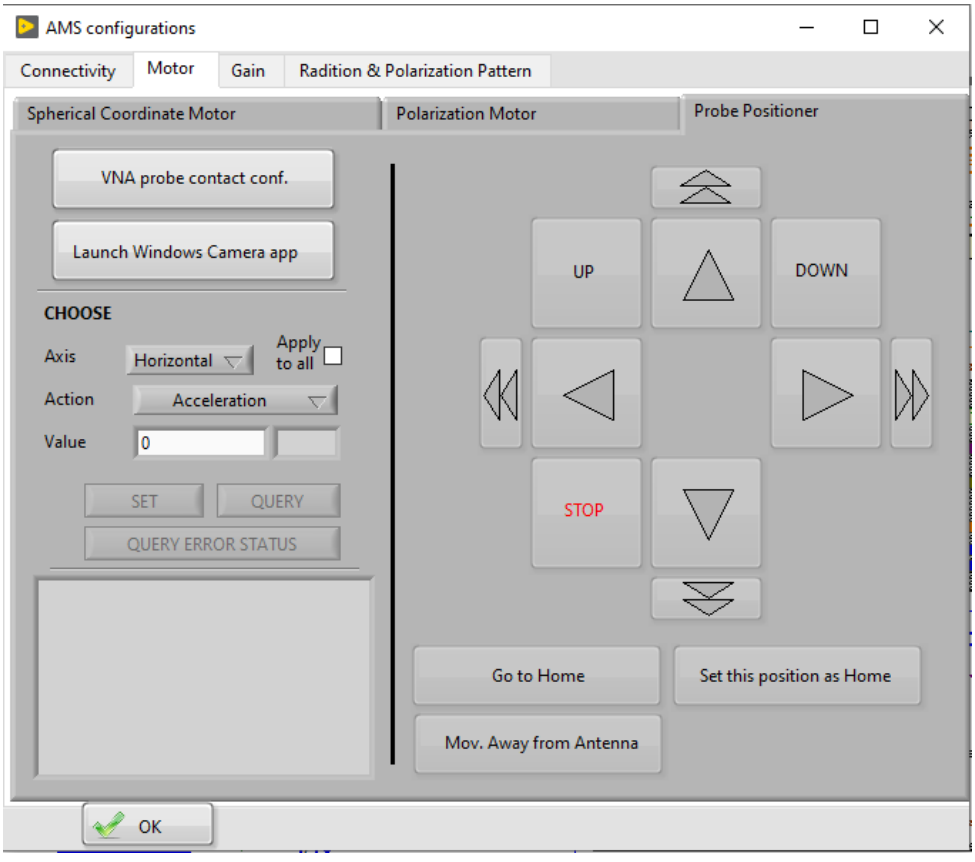
AMS configurations
Connectivity
Motor
Gain
Radition & Polarization Pattern
Spherical Coordinate Motor
Polarization Motor
Probe Positioner
VNA probe contact conf.
Launch Windows Camera app
CHOOSE
Axis
Horizontal
Apply to all
Action
Acceleration
Value
0
SET
QUERY
QUERY ERROR STATUS
UP
DOWN
STOP
Go to Home
Set this position as Home
Mov. Away from Antenna
OK

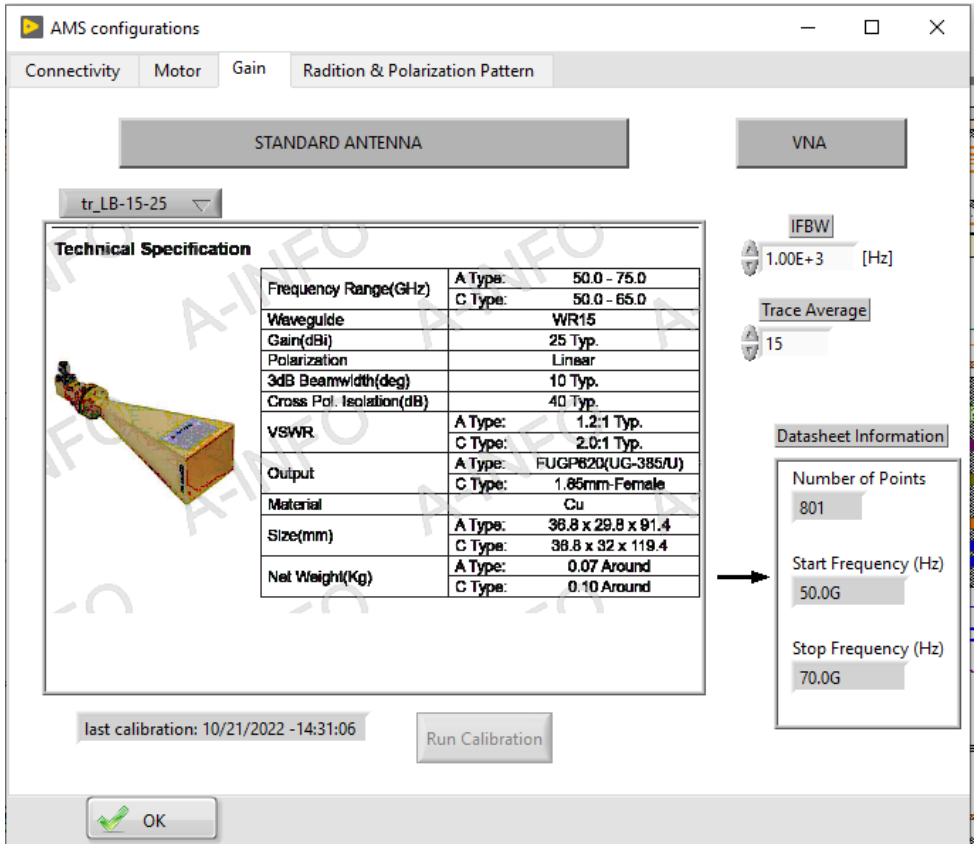
AMS configurations
Connectivity
Motor
Gain
Radition & Polarization Pattern
STANDARD ANTENNA
VNA
tr_LB-15-25
Technical Specification
Frequency Range(GHz)
A Type: 50.0 - 75.0
C Type: 50.0 - 65.0
Waveguide
WR15
Gain(dBi)
25 Typ.
Polarization
Linear
3dB Beamwidth(deg)
10 Typ.
Cross Pol. Isolation(dB)
40 Typ.
VSWR
A Type: 1.2:1 Typ.
C Type: 2.0:1 Typ.
Output
A Type: FUGP620(UG-385/U)
C Type: 1.85mm-Female
Material
Cu
Size(mm)
A Type: 38.8 x 29.8 x 91.4
C Type: 38.8 x 32 x 119.4
Net Weight(Kg)
A Type: 0.07 Around
C Type: 0.10 Around
IFBW
1.00E+3
[Hz]
Trace Average
15
Datasheet Information
Number of Points
801
Start Frequency (Hz)
50.0G
Stop Frequency (Hz)
70.0G
last calibration: 10/21/2022 -14:31:06
Run Calibration
OK

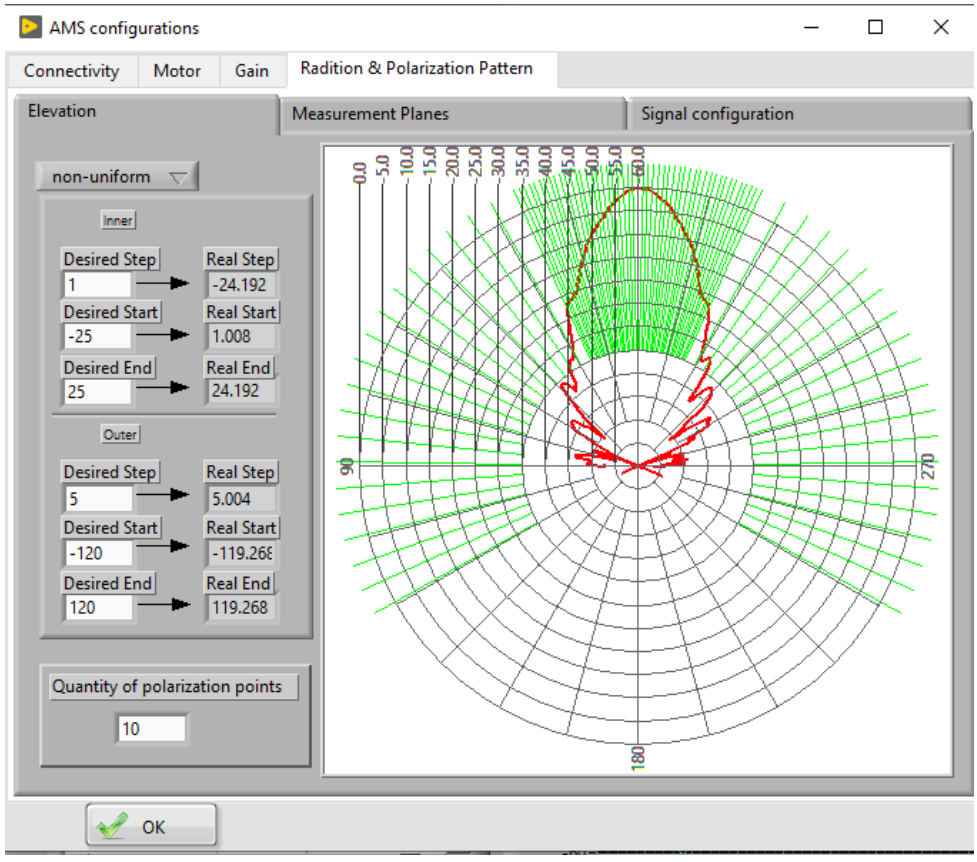
AMS configurations
Connectivity
Motor
Gain
Radition & Polarization Pattern
Elevation
Measurement Planes
Signal configuration
non-uniform
Inner
Desired Step
1
Real Step
-24.192
Desired Start
-25
Real Start
1.008
Desired End
25
Real End
24.192
Outer
Desired Step
5
Real Step
5.004
Desired Start
-120
Real Start
-119.268
Desired End
120
Real End
119.268
Quantity of polarization points
10
0.0
5.0
10.0
15.0
20.0
25.0
30.0
35.0
40.0
45.0
90
270
180
OK

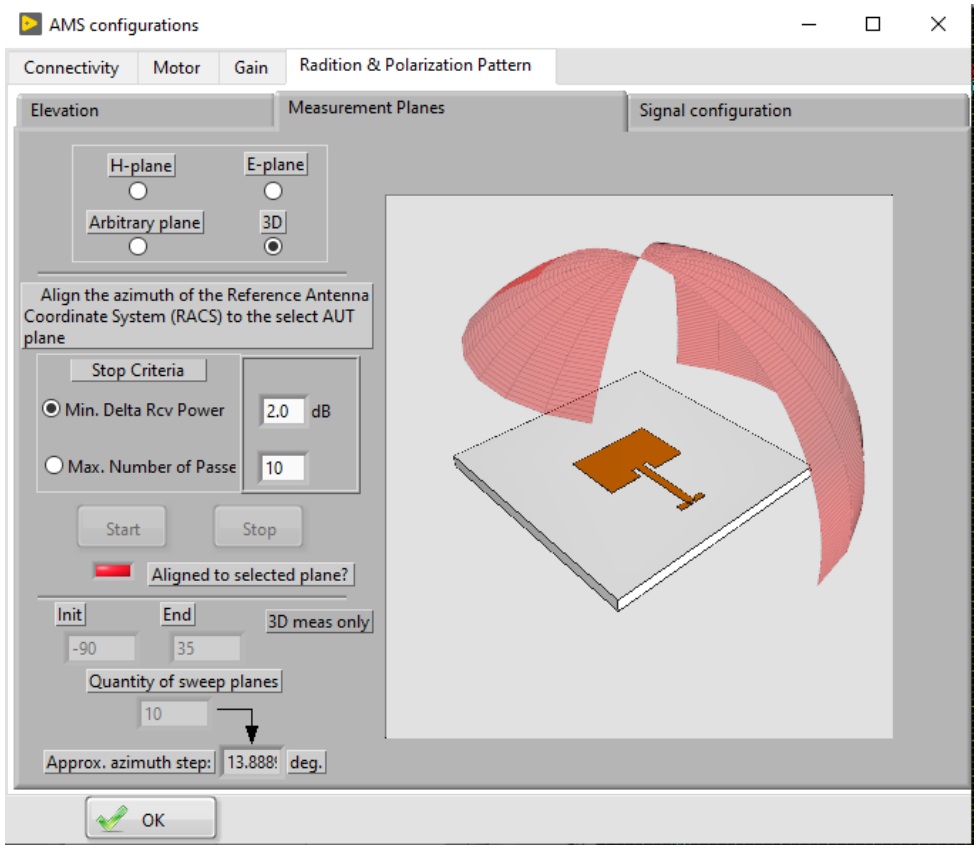
AMS configurations
Connectivity
Motor
Gain
Radition & Polarization Pattern
Elevation
Measurement Planes
Signal configuration
H-plane
E-plane
Arbitrary plane
3D
Align the azimuth of the Reference Antenna Coordinate System (RACS) to the select AUT plane
Stop Criteria
Min. Delta Rcv Power
2.0
dB
Max. Number of Passe
10
Start
Stop
Aligned to selected plane?
Init
End
3D meas only
-90
35
Quantity of sweep planes
10
Approx. azimuth step:
13.888
deg.
OK

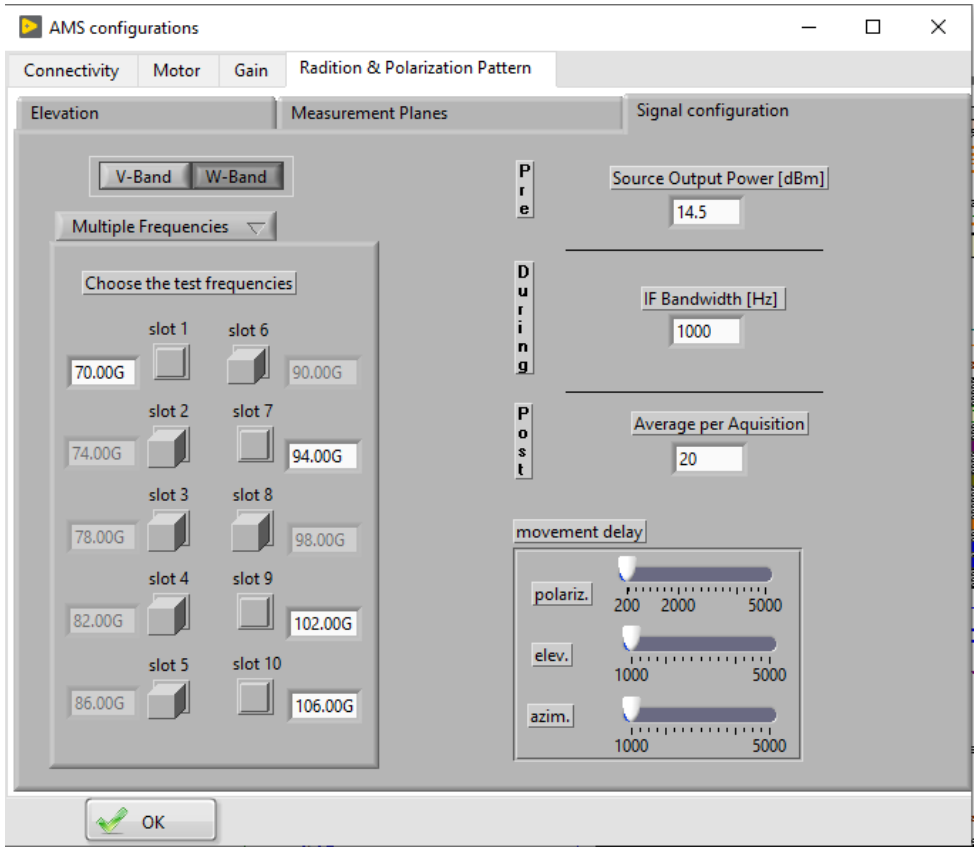
AMS configurations
Connectivity
Motor
Gain
Radition & Polarization Pattern
Elevation
Measurement Planes
Signal configuration
V-Band
W-Band
Multiple Frequencies
Choose the test frequencies
slot 1
slot 6
70.00G
90.00G
slot 2
slot 7
74.00G
94.00G
slot 3
slot 8
78.00G
98.00G
slot 4
slot 9
82.00G
102.00G
slot 5
slot 10
86.00G
106.00G
Pre
Source Output Power [dBm]
14.5
During
IF Bandwidth [Hz]
1000
Post
Average per Aquisition
20
movement delay
polariz.
200
2000
5000
elev.
1000
5000
azim.
1000
5000
OK